Design and Fabrication of a Mask Projection Microstereolithography System for the Characterization and Processing of Novel Photopolymer Resins

Philip Michael Lambert

Thesis submitted to the faculty of the Virginia Polytechnic Institute and State University in partial fulfillment of the requirements for the degree of

Master of Science
In
Mechanical Engineering

Christopher B. Williams
Timothy E. Long
Lissett R. Bickford

June 26th, 2014
Blacksburg, VA

Keywords: Mask Projection Microstereolithography, Stereolithography, Vat Polymerization, Tissue Scaffolds, Novel Photopolymer

Design and Fabrication of a Mask Projection Microstereolithography System for the Characterization and Processing of Novel Photopolymer Resins

Philip Michael Lambert

ABSTRACT

The goal of this work was to design and build a mask projection microstereolithography (MPμSL) 3D printing system to characterize, process, and quantify the performance of novel photopolymers. MPμSL is an Additive Manufacturing process that uses DLP technology to digitally pattern UV light and selectively cure entire layers of photopolymer resin and fabricate a three dimensional part. For the MPμSL system designed in this body of work, a process was defined to introduce novel photopolymers and characterize their performance. The characterization process first determines the curing characteristics of the photopolymer, namely the Critical Exposure (E_c) and Depth of Penetration (D_p). Performance of the photopolymer is identified via the fabrication of a benchmark test part, designed to determine the minimum feature size, XY plane accuracy, Z-axis minimum feature size, and Z-axis accuracy of each photopolymer with the system.

The first characterized photopolymer was poly (propylene glycol) diacrylate, which was used to benchmark the designed MPμSL system. This included the achievable XY resolution (212 micrometers), minimum layer thickness (20 micrometers), vertical build rate (360 layers/hr), and maximum build volume (6x8x36mm^3). This system benchmarking process revealed two areas of underperformance when compared to systems of similar design, which lead to the development of the first two research questions: (i) "How does minimum feature size vary with exposure energy?" and (ii) "How does Z-axis accuracy vary with increasing Tinuvin 400 concentration in the prepolymer?" The experiment for research question (i) revealed that achievable feature size decreases by 67% with a 420% increase in exposure energy. Introducing 0.25wt% of the photo-inhibitor Tinuvin 400 demonstrated depth of penetration reduction from 398.5 micrometers to 119.7 micrometers. This corresponds to a decrease in Z-axis error from 119% (no Tinuvin 400) to 9% Z-axis error (0.25% Tinuvin 400).

Two novel photopolymers were introduced to the system and characterized. Research question (iii) asks "What are the curing characteristics of Pluronic L-31 how does it perform in the MPμSL system?" while Research Question 4 similarly queries "What are the curing characteristics of Phosphonium Ionic Liquid and how does it perform in the MPμSL system?" The Pluronic L-31 with 2wt% photo-initiator had an E_c of 17.2 mJ/cm$_2$ and a D_p of 288.8 micrometers, with a minimum feature size of 57.3 ± 5.7 micrometers, with XY plane error of 6% and a Z-axis error of 83%. Phosphonium Ionic Liquid was mixed in various concentrations into two base polymers, Butyl Diacrylate (0% PIL and 10% PIL) and Poly Ethylene Dimethacrylate (5% PIL, 15% PIL, 25% PIL). Introducing PIL into either base polymer caused the E_c to increase in all samples, while there is no significant trend between increasing concentrations of IL in either PEGDMA or BDA and depth of penetration. Any trends previously identified between penetration depth and Z accuracy do not seem to extend from one resin to another. This means that overall, among all resins, depth of penetration is not an accurate way to predict the Z axis accuracy of a part. Furthermore, increasing concentrations of PIL caused increasing % error in both XY plane and Z-axis accuracy.

Acknowledgements

To those who inspire me to be the best I can be, I want to recognize:

- My mother, for her guidance and perspective.
- My father and brother, for their enthusiasm and pride.
- Alexandra Oliver, for expecting greater things of me than I ever expected of myself.

I would like to recognize ICTAS (Institute of Critical Technology and Applied Science) for providing the financial support for this body of research.

I would like to thank Dr. Lisette Bickford and Dr. Timothy Long for graciously serving as members of my committee. The Long group played no small role in the success of this project, particularly the prompt work and enduring patience of Nancy Zhang and Alison Schultz. Furthermore, I recognize Nicolas Chartrain, whose assistance with the more dolorous tasks and experiments certainly eased my burdens.

My coworkers and peers in the DREAMS Lab, your insight, support, and friendship throughout the research process were instrumental to my graduate level success. For that, I am exceptionally grateful. Specifically, I'd like to acknowledge Earl Campaigne, who was my coworker and friend. As we explored Projection Stereolithography together, our shared experiences were invaluable to my success as well as my sanity.

Finally, I'd like to recognize and extend my greatest gratitude to my advisor, Dr. Christopher Williams. Under his selfless guidance and advice, as well as his criticism, I grew as a researcher and an engineer. I believe the value of my graduate degree is far greater as a result of my relationship with Dr. Williams and my experiences within the DREAMS Lab.

All photos by author, 2014.

Table of Contents

Table of Figures

Table of Tables

1. Introduction to Mask Projection Microstereolithography and Thesis Objectives

1.1. Mask Projection Microstereolithography

This section was written in collaboration with Earl Andrew Campaigne III of the DREAMS Lab.

Within the realm of Additive Manufacturing (AM), stereolithography (SL) is a well-established technology used to create parts, with features as small as 75µm, by crosslinking layers of photopolymer resin with a scanning ultraviolet (UV) laser beam. Mask projection microstereolithography (MPµSL) modifies the SL process by replacing the scanning UV laser with a UV light source and dynamic pattern generator (or dynamic mask) to digitally pattern light and expose an entire cross-sectional layer at once. Unlike traditional SL processes, MPµSL is not limited by the laser beam radius or its scan speed, and thus enables the creation of feature sizes smaller than 10µm while also reducing build times by an order of magnitude [1]–[14].

In 1995 Arnaud Bertsch presented the first MPµSL system, which he then called integral stereolithography [1], [2], [15] The general mask projection micro-stereolithography process flow is illustrated in Figure 1-2. Light is first created by a source - commonly a light emitting diode (LED), lamp, or laser. This light is then conditioned by a series of optics that may include collimating lenses, wavelength filters, and homogenizing rods. A mirror is often used to reflect light onto a dynamic pattern generator (dynamic mask), such that it is parallel to the projection surface. The dynamic pattern generator digitally patterns and projects the incident light as an image. Finally, the patterned light is resized by an optical lens, or series of lenses, to focus the final image on the surface of liquid photopolymer resin. The projected pattern initiates the crosslinking of monomer chains within the photopolymer resin, causing it to change phases from a liquid to a solid in a process called polymerization. A diagram of the cross-linking process presented in Figure 1-1.

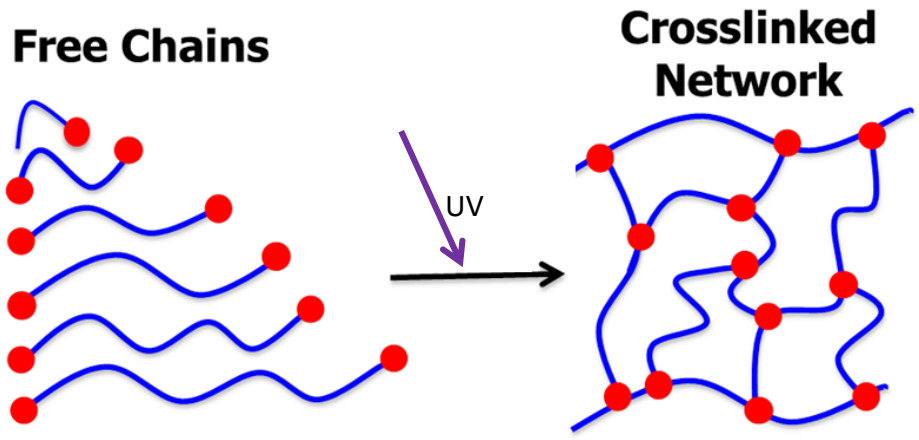

Figure 1-1: Diagram of the polymerization process.

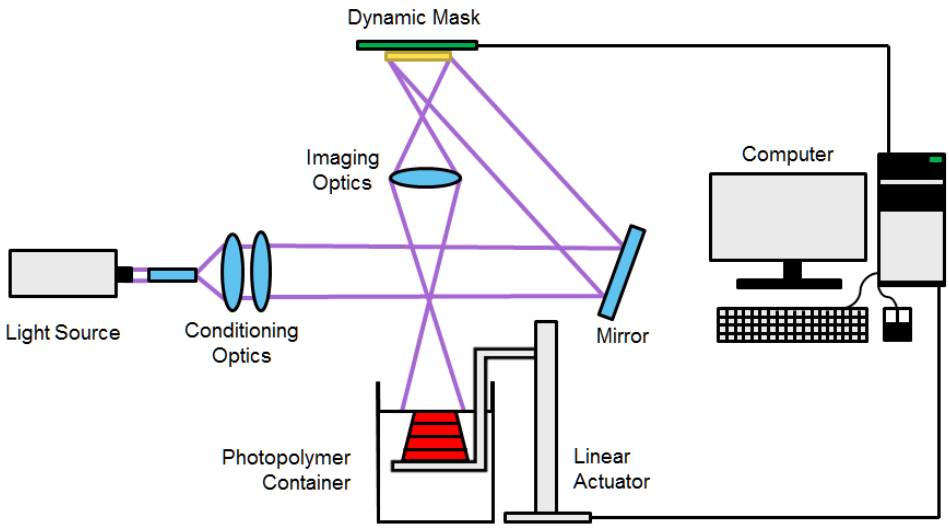

Figure 1-2: Diagram of a typical MPµSL system. Purple lines highlight the travel of light.

The first layer of photopolymer resin is cured on a build platform. The build platform is then repositioned such that additional resin recoats the previously cured photopolymer to provide material for creating a subsequent layer. An image of the next cross-sectional layer is projected to cure it on top of the previous layer. After the final cross-section is projected, the completed 3D part is removed and post-processed.

Mask projection microstereolithography systems can process novel photopolymers with unique properties at very high resolutions. The ability to produce high-resolution features makes

MPμSL an ideal candidate for the production of engineered tissue scaffolds, provided that the material is biocompatible.

1.2.Tissue Engineering

The field of tissue engineering is a multidisciplinary arena that aims to develop biological tools and processes that can be used to regenerate defective tissue. In tissue engineering, cells are isolated from a patient, the population expanded in a cell culture, and then seeded to a carrier. The most common and well-established approach to tissue engineering is the development of pre-made porous scaffold for cell seeding.

1.2.1. What are Tissue Scaffolds

The scaffold is used as a temporary support structure which seeded cells use as a backbone to direct tissue formation, and serves as a template for cell adhesion [16]–[18]. They guide the growth of cells and accommodate tissue regeneration in three dimensions. A highly porous artificial extracellular matrix, the scaffold is a structure with numerous interconnected channels of less than 500 μm in width [19]. Figure 1-3 shows an example of a scaffold embedded in-situ.

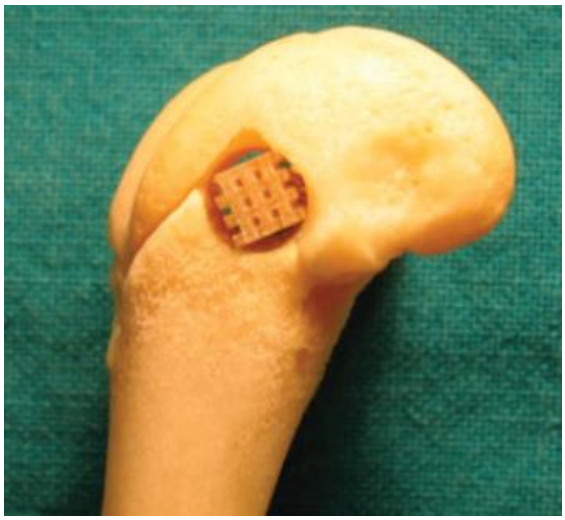

Figure 1-3: Image of an engineering tissue scaffold embedded in a cavity of a distal femoral bone of a New Zealand white rabbit (C. Heller, M. Schwentenwein, G. Russmueller, F. Varga, J. Stampfl, and R. Liska, "Vinyl Esters : Low Cytotoxicity Monomers for the Fabrication of Biocompatible 3D Scaffolds by Lithography Based Additive Manufacturing," pp. 6941–6954, 2009, Used under fair use, 2014).

The two main considerations for development of tissue scaffolds are material selection and scaffold architecture. The desirable characteristics of materials in this application are biocompatibility and biodegradability. Biocompatibility is described as possessing the correct surface chemistry to promote cell attachment and function, while biodegradability means the breakdown of the scaffold into nontoxic products, leaving behind living tissue [18].

Performance of a tissue scaffold has been shown to be dependent on the structure, specifically the porosity and pore size, of the matrix. Highly porous support structures are favorable for mass transport, delivering cell mass for tissue regeneration. Furthermore, high porosity is desirable for diffusion of nutrients and waste products to and from the tissue growth, as well as for vascularization, which are requirements for successful cell growth. While a large surface area favors cell attachment, the surface area/volume ratio of a porous material is dependent on density and diameter of pores. Furthermore, the diameter of the cells dictates the minimum pore size. When defining porosity and pore size, considerations must be made such that scaffolds retain good mechanical properties while also being permeable and porous for the transport of cells and nutrients [16], [18], [19]. An example scaffold with ~400 micron pores and high porosity is shown in Figure 1-4.

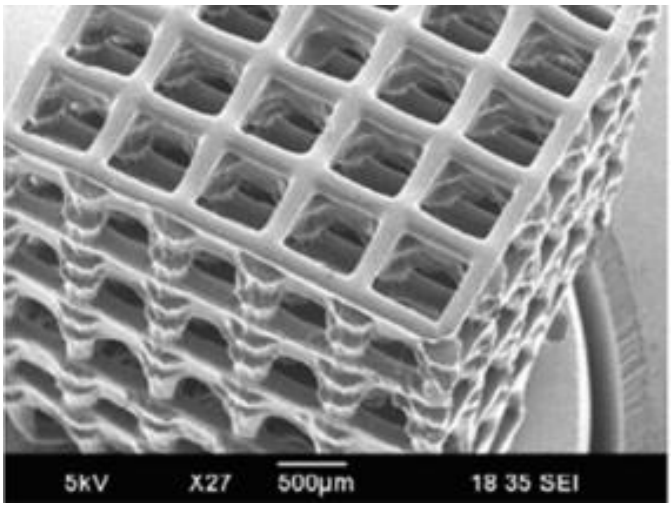

Figure 1-4: An SEM image of a scaffold demonstrating porosity at a micrometer scale.

The macrostructure of a scaffold is also important, meaning the structure must be processed to fit in the space where tissue regeneration is required.

Traditional tissue scaffold manufacturing methods are limited in several respects, particularly in controlling pore size and porosity, which are inherently stochastic. The following section will provide a brief outline of some of these traditional manufacturing methods and their limitations.

1.2.2. Tissue Scaffold Manufacturing Methods

Scaffold manufacturing techniques can be classified into three categories: (i) processes using porogens in biomaterials, (ii) techniques using woven or non-woven fibers, and (iii) processes using 3D printing [16].

1.2.2.1. Traditional Manufacturing

The first (i) and second (ii) categories are examples of traditional manufacturing. In the first category, solid material is incorporated with porogens, which could be a gas, liquid, or solid, that is removed after fabrication to leave behind a porous structure. These techniques include solvent casting/particulate leaching and gas foaming.

Solvent Casting and Particulate Leaching (SCPL) consists of dispersing mineral or organic particles into polymer solutions, which is then either cast or freeze-dried in order to evaporate the solvent. The particles are leached out to produce a porous polymer matrix. This method can be used to produce matrices with porosity as high as 93% with pore diameters around 500 μm, but can only produce substrates as thick as 3mm. However, this can be overcome by fusing layers of the 3mm substrates to make a 3D matrix [18]. Figure 1-5 shows an image of a porous scaffold manufactured with SPCL.

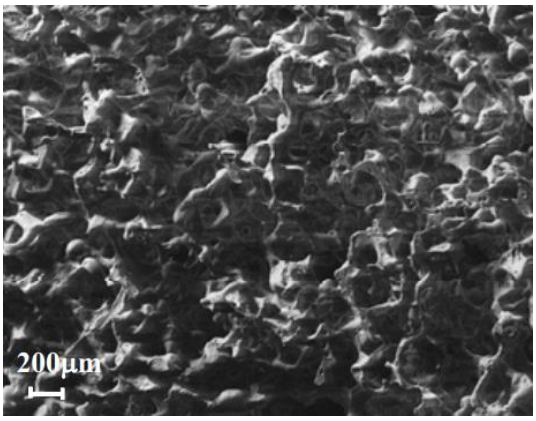

Figure 1-5: Micro-scale image of a scaffold manufactured via Solvent Casting and Particulate Leaching (F. Intranuovo and R. Gristina, "Plasma Modification of PCL Porous Scaffolds Fabricated by Solvent-Casting/Particulate-Leaching for Tissue Engineering," *Plasma Process.*, pp. 1–4, 2014, Used under fair use, 2014).

A high pressure gas technique used for scaffold fabrication is called gas-foaming. Polymer discs are exposed to high pressure CO2 gas to saturate the discs with CO2. Reducing the pressure to ambient creates thermodynamic instability and leads to the expansion of the saturated gas and the growth of macropores. The disadvantage of this technique is the formation of nonporous skin on the external surface [18], [22].

The second category uses woven or non-woven fibers that are layered or piled together and bonded in a thermal or chemical adhesion process. These techniques are not ideal for fine controlling of porosity or pore size. Fibers can also be generated in a process called electrospinning (Figure 1-6), in which high voltage generates a spinning fiber jet from a polymer solution [16], [18].

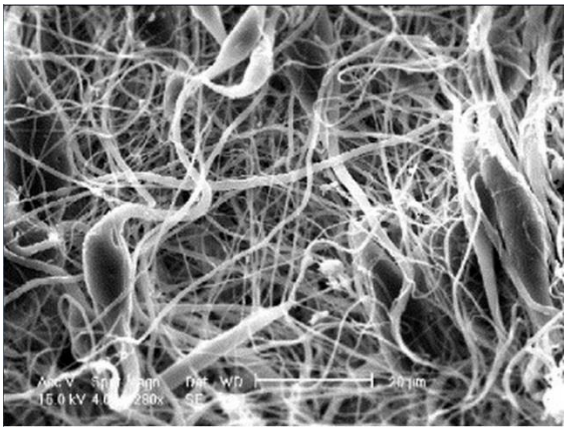

Figure 1-6: Micro-scale image of a scaffold manufactured through electrospinning (J. Lannutti, D. Reneker, T. Ma, D. Tomasko, D. Farson, "Electrospinning for tissue engineering scaffolds," *Mater. Sci. Eng. C*, vol. 27, no. 3, pp. 504–509, Apr. 2007, Used under fair use, 2014).

As mentioned earlier, the main disadvantage of the traditional manufacturing techniques is the inherent stochastic distribution and size of pores. The techniques above cannot control the location, size, or distribution of pores, which means scaffold design cannot be optimized.

1.2.2.2. Additive Manufacturing of Tissue Scaffolds

The third category, the category of interest of this research, is scaffold fabrication using additive manufacturing (AM) techniques. The majority of AM processes have been considered for scaffold fabrication, including selective laser sintering, fused deposition modeling, binder jetting, and stereolithography [16], [19]. These techniques all utilize an additive, layer-by-layer manufacturing process, where the geometry of each layer can be designed and controlled. Stacking these layers in a consecutive fashion enables the design of complex 3D parts. These techniques use direct curing or deposition of material in a predetermined manner, allowing the scaffold to have predefined porosity and pore size. The advantage of AM on tissue engineering is the ability to control microstructure, enabling interconnecting micro-channels, as well as controlled macrostructure. This gives AM a significant advantage over traditional manufacturing methods for fabricating tissue scaffold designs with controlled structure. The overarching process is referred to as Computer Aided Tissue Engineering (CATE), which is described as an approach for biomimetic modelling and design of tissue scaffolds [24]. Mask projection

microstereolithography offers the resolution and design freedoms required to transition CATE designs into real, fabricated 3D scaffolds.

1.3.Formulation of Research Questions and Tasks

Give the goal of using MPμSL to fabricate tissue scaffolds, as well as other micro-scale parts with novel photopolymers, the broad objective of this work is presented as:

> "Design and build a projection microstereolithography 3D printing system to characterize, process, and quantify the performance of novel photopolymers."

In this section, the primary research questions that this research aims to answer are presented, along with a brief summary of tasks to answer each question.

1.3.1. Polymer Characterization

In order to develop 3D structures with projection stereolithography, each polymer that will be processed by the MPμSL system must be characterized. This means a process must be developed for this system to determine the curing characteristics of the photopolymer resin, as well as identify several photopolymer dependent performance parameters. These performance parameters include the XY plane minimum feature size, the XY plane accuracy, the Z-axis minimum feature size, and the Z-axis (XZ and YZ planes) accuracy. Characterization Question 1 (CQ1) addresses these requirements.

> **CQ1:** How can the curing characteristics of a photopolymer and its performance with the MPμSL system be determined?

The curing characteristics of a polymer are determined by developing a working curve for each polymer resin. A benchmark part was designed and a process was created to identify the polymer performance parameters listed above. The process is outlined in a step-by-step format, and identifies all the parameters necessary to quantify photopolymer performance and answer CQ1.

1.3.2. System Characterization

The system developed as part of this body of research was designed using the morphological matrix tool introduced in Chapter 2. The goal of Characterization Question 2 (CQ2) is to characterize the performance of this system relative to the systems designed with similar morphology. The secondary goal of this characterization question is to demonstrate the validity of the morphological matrix as a design tool for projection microstereolithography systems.

CQ2: How does the performance of the system designed as part of this work compare to other systems of similar morphology?

To determine the performance of this system, experiments were designed to measure four performance metrics: minimum feature size, minimum layer thickness, maximum part size, and vertical build rate. This system's performance was compared to the performance of machines of similar morphology. The result of this comparison should identify areas where system performance can be improved.

Also important in system characterization, while somewhat independent of the previously introduced performance metrics, is how closely the printed part represents the CAD model. Characterization Question 3 (CQ3) aims to characterize the performance of the system that is independent of the performance metrics highlighted in CQ2.

CQ3: How well does a printed part dimensionally compare to its designed model?

The dimensional comparison suggested in CQ3 refers to the size of the part, the relative size of the features, the locations of features, and the form of the part. This question will be answered by measuring feature accuracy in the XY, XZ and YZ planes of a benchmark characterization part. Characterization methods include digital microscopy, Scanning Electron Microscopy (SEM), and micro-computed tomography (micro-CT).

1.3.3. Process Improvement

The results of the system characterization experiments conducted to answer CQ2 and CQ3 revealed several areas where the MPμSL system does not meet performance expectations. This

includes the achievable minimum XY feature size and the Z-axis feature accuracy. Initial experiments to improve the system resolution suggested that a relationship exists between the XY resolution and exposure energy. Research Question 1 explores the process/property relationship between exposure and XY feature size.

1.3.3.1. Effects of Exposure on Resolution

Initial system characterization experiments determined the actual minimum lateral (XY) feature size of the system was significantly larger than the theoretical expectation (as is shown in the section addressing CQ2 in Chapter 5). This means that there are limits in the system that were not predicted. Experiments conducted by Jariwala et. al. suggest that the presence of oxygen on the surface of the resin may be causing the consumption of free radicals faster than in the polymerization process [25]. Should this be the case, the inhibition effects of oxygen would be limiting the size of XY plane features. Features below a certain size may require a higher amount of exposure energy than that specified by the working curve to cure. To explore the validity of this hypothesis, Research Question 1 (RQ1) was developed:

RQ1: How does minimum feature size vary with exposure energy?

This question seeks to determine the process/property relationship between exposure and XY feature size. The relationship between exposure and feature size was explored by designing and conducting an experiment that varied exposure on individually printed benchmark parts. The smallest printed feature on each part was located, measured, and plotted against exposure to identify any trends between exposure energy and minimum feature size.

1.3.3.2. Effects of Tinuvin on Z-axis Accuracy

The results of CQ2 presented a significant accuracy issue along the Z-axis called print-through. Print-through is a common problem in vat photopolymerization processes, and occurs due the uncontrolled penetration of UV light into photopolymer resin when fabricating down-facing surfaces [26]. Several approaches have been presented in literature to account for print-through, including a software based “Compensation Zone” approach by Limaye/Rosen [27]. However, instead of approaching the problem through process control, others have used an

approach where UV photo-absorber is introduced into the resin to alter the curing characteristics and reduce the penetration depth of UV light. A commercial UV photo-absorber called Tinuvin 400 is the photo-absorber explored in Research Question 2 (RQ2).

RQ2: How does Z-axis accuracy vary with increasing Tinuvin 400 concentration in the prepolymer?

This question aims to determine the structure/property relationship between Tinuvin 400 concentration in prepolymer resins and Z-axis accuracy in printed parts. The relationship between Tinuvin 400 concentration in an acrylate-based photopolymer and Z-axis accuracy was explored by designing and conducting an experiment that varied the concentration of Tinuvin 400 in the photo-curable poly (propylene glycol) diacrylate resin. Working curves were developed and a benchmark part was printed for each concentration, and the Z-axis feature accuracy was measured analyzed for trends.

1.3.4. Novel Photopolymer Characterization

As mentioned in the broad objective of this work, several photopolymers with novel structures were introduced into the MPμSL system for processing. These polymers include a novel co-block polymer called Pluronic L-31 and a phosphonium ionic liquid (PIL). The co-block Pluronic L-31 is a polymer of interest due to its reported biocompatibility, and can be used in tissue engineering scaffold fabrication and other biological applications. The phosphonium ionic liquid, a molten salt, is known to be ionically conductive. Ionic conductivity is useful in micro-actuation/sensing or microelectromechanical (MEMS) applications [28]. Before 3D structures can be manufactured with these novel resins, their processability must first be determined. Research Question 3 (RQ3) and Research Question 4 (RQ4) aim to understand the curing characteristics and performance of these resins according to the methods described by Characterization Question 1.

RQ3: What are the curing characteristics of Pluronic L-31 how does it perform in the MPμSL system?

RQ4: What are the curing characteristics of phosphonium ionic liquid and how does it perform in the MPμSL system?

The answers to RQ3 and RQ4 will serve to validate CQ1, as well as act as the baseline for introducing and characterizing new polymers into this MPμSL system. Furthermore, application specific parts were printed to demonstrate the potential uses of fabricating MPμSL parts with these novel resins. For the Pluronic L-31 photopolymer, a basic tissue scaffold was printed.

1.4.Thesis Objective and Roadmap

To recall, the overall goal of this work is stated as:

"Design and build a projection microstereolithography 3D printing system to characterize, process, and quantify the performance of novel photopolymers."

In Chapter 2, a comprehensive literature review of published Mask Projection Microstereolithography systems is presented. The data collected as part of this review was synthesized into design tools that are used to categorically analyze MPμSL system embodiments. These embodiment categories are analyzed based on several system performance metrics, which are then used identify several design considerations for future MPμSL system development. These design tools and considerations were used in the design and development of the MPμSL system constructed as part of this body of research.

Chapter 3, "Design of a Mask Projection Microstereolithography System," details the process for the design and development of the MPμSL system. As mentioned, this section utilizes the design tools and design considerations presented in Chapter 2. The entire design process, from conception of finalization, is discussed in detail.

Chapter 4 is titled "Methods for Characterizing Novel Polymers (CQ1)." This chapter explains the process developed for introducing and characterizing new photo-curable resins into this MPμSL system. The process described provides the answer to CQ1**: "**How can the curing characteristics of this photopolymer and its performance with the MPμSL system be determined?"

In Chapter 5, “Benchmarking the MPµSL System”, Characterization Question 2 and Characterization Question 3 are addressed. The MPµSL system performance metrics are determined and compared to the performance metrics of similar embodiments. The accuracy of the system is also determined, in reference in CQ3. The experiments conducted to answer CQ2 and CQ3 revealed the areas for system improvement described in RQ1 and RQ2.

Chapter 6 is titled “Improving System Performance.” This chapter explores the first two research questions regarding XY plane resolution improvements and cure-depth control. This chapter explains the experiments conducted to determine the process/property relationship between exposure energy and XY feature size (Research Question 1), as well as the structure/property relationship between Tinuvin 400 concentration and Z-accuracy (Research Question 2).

“Novel Photopolymer Characterization” in Chapter 7 presents experimental methods (utilizing the process described for CQ1) and results regarding the characterization of two polymers novel to projection stereolithography: Pluronic L-31 and phosphonium ionic liquid.

The report is finalized by identifying areas of future work and process improvements in the “Conclusions and Future Work.”

2. Design Considerations for Mask Projection Microstereolithography

This section was written in collaboration with Earl Andrew Campaigne III of the DREAMS Lab.

Many mask projection microstereolithography systems have already been developed, some of which have been commercialized. While each of these systems provides the same fundamental functionality, different system embodiments were developed to meet the requirements of a variety of applications. This chapter analyzes these existing MPμSL systems and abstracts the inherent system tradeoffs in order to develop guide for designing future systems and applications.

2.1. Background and Motivation

The MPμSL process is described in terms of functional components and design considerations in Section 2.2. Following the AM classification approach suggested by Williams, Rosen and Mistree [29], a morphological matrix design tool is used to visually categorize MPμSL design solutions. Performance tradeoffs are identified between the various system components that reoccur throughout published MPμSL systems in Section 2.3. The performance metrics used to quantify these tradeoffs are the systems' (i) achievable layer thickness, (ii) minimum feature size, (iii) build volume, and (iv) vertical build time. Within the organizational context of the presented morphological matrix, this chapter categorizes many MPμSL systems in Section 2.4, while drawing conclusions from their design decisions. The results and conclusions of this review are presented in Section 2.5.

2.2. MPμSL Functional Analysis

This section describes the MPμSL process as a set of sub-functions and performance parameters, which are shown through a functional decomposition and a morphological matrix.

2.2.1. MPμSL System Sub-functions

The MPμSL process can be discretized into a set of functional subsystems, each with their own set of unique design considerations. The final performance of a MPμSL system is dependent on the sum of these functional parts. They are as follows:

- *Light source* produces the luminous energy that is projected onto the resin surface to selectively cure photopolymer.
- *Conditioning optics* change properties of the projected light for MPμSL applications.
- *Dynamic mask* digitally patterns and projects incident light to selectively cure photopolymer.
- *Projection orientation* is the position of the dynamic mask relative to the polymer container.
- *Imaging optics* expand or reduce the projected image to achieve the desired image resolution.
- *Recoat method* supplies liquid photopolymer over previous layers for the creation of new layers.
- *Build platform* supports the object being made.
- *Vertical actuator* repositions the build platform for the creation of new layers.
- *System controls* programmatically alter system properties during the fabrication process.
- *Photopolymer container* holds the reservoir of photopolymer and contains the build platform.
- *Photopolymer* is the raw material used in MPμSL to fabricate three dimensional objects.

These sub-functions, and their respective design considerations, are presented as a functional decomposition in Figure 2-1. This list includes the core system functionalities of MPμSL systems; however, it is not necessarily comprehensive. Some applications may require application-specific considerations, such as humidity control or gas metering within an enclosed build volume to reduce the influence of environmental inconsistencies [7].

This discretization of the MPμSL process into a set of necessary functional subsystems enables the categorization and comparison of MPμSL systems. A morphological matrix – a design tool that presents system sub-functions and their respective potential design solutions – is provided for the MPμSL process in Figure 2-2. Using this tool, a designer is able to create different MPμSL embodiments by implementing unique combinations of sub-functions. In

addition, this tool can be used as a framework for categorizing and comparing existing MPμSL systems on a functional basis.

It is important to note that the presented matrix features only those sub-functions that have the most direct effect on overall system performance. The remaining sub-functions (build platform, vertical actuator, system controls, and photopolymer) are not detailed in this work as they either have only indirect effects on system performance, are common engineering components, and/or are not within the scope of this chapter (e.g., controls and materials issues).

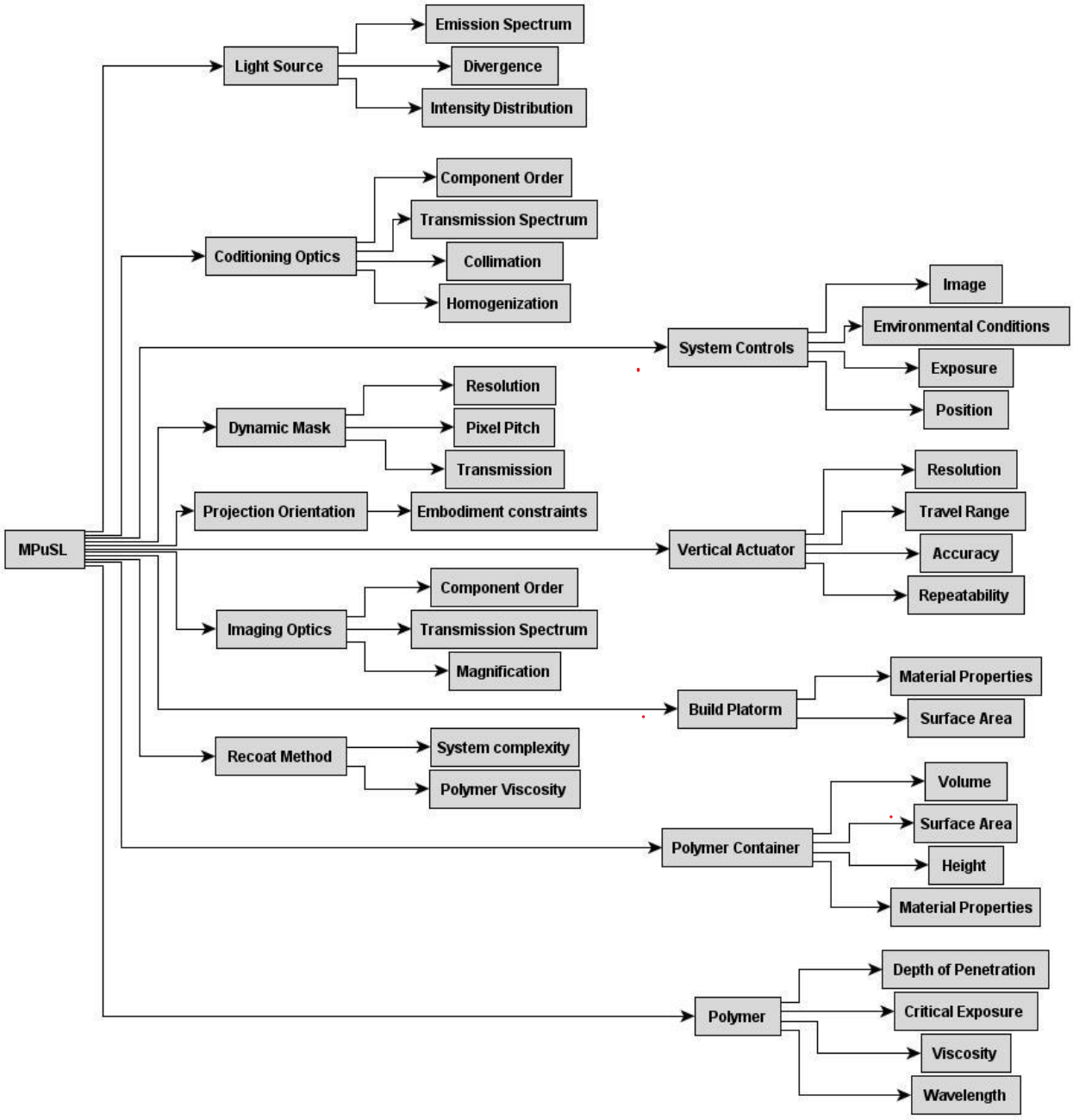

Figure 2-1: Functional decomposition of the MPµSL process relating sub-functions to design considerations.

Sub-functions	*Solutions*			
Light Source	Lamp	Light Emitting Diode (LED)	Laser	
Conditioning Optics	Homogenization	Collimation	Filtering	Beam Expansion
Pattern Light	Liquid Crystal Display (LCD)	Digital Micromirror Device (DMD, DLP Projector)	Liquid Crystal on Silicone (LCoS)	
Projection Orientation	From Above	From Below		
Imaging Optics	Image Expansion	Image Reduction		
Recoat Method	By gravity	By spreading	By pumping	By dipping

Figure 2-2: Morphological matrix discretizing the MPµSL process into a set of functional subsystems and their solutions.

2.2.2. MPµSL Performance Parameters

As they share the same broad design goals, all MPµSL systems can be evaluated via a common set of design metrics, and thus provide a basis for comparison. The MPµSL performance parameters and relationships are as follows:

- *Layer thickness (µm)* is a metric for quantifying vertical (z-axis) resolution. The achievable layer thickness is largely determined by the employed recoating method, actuator resolution, polymer characteristics, and projection orientation.
- *Minimum feature size (µm)* defines the cross-sectional resolution and smallest obtainable features in the X-Y plane. The dynamic pattern generator, projection orientation, and imaging optics define the projected cross-sectional resolution, while the recoating method restricts the physical minimum feature size.
- *Build volume (mm^3)* is a metric for quantifying the dimensions of the largest printed part. The dynamic mask and imaging optics limit the size of the projected image in the X-Y plane and thus the maximum build volume.
- *Vertical build rate (mm/s)* is a metric that quantifies process throughput. Unfortunately, MPµSL build rates are often published using unclear terms. For example, many authors

state throughput in units of seconds per layer, but do not specify whether this is the exposure time per layer or total build time per layer. This is compounded by the fact that each system uses different photopolymers, which require different exposures. This often prevents the direct comparison of vertical build rates for previously published work.

A Process Planning matrix (from Quality Function Deployment methodology) is used to illustrate the interrelationships between sub-functions and performance metrics (Table 2-1). The strength of each relationship is indicated by assigned values where 1 represents a weak relationship, 3 a medium relationship, and 9 a strong relationship. For example: There is a strong relationship (9) between the minimum feature size (µm) and imaging optics of a MPµSL machine, because the imaging optics expand or reduce the projected features. In addition, build rate is primarily determined by projection orientation and recoating method.

Table 2-1: QFD Process Planning matrix illustrating the interrelationships between MPµSL functional subsystems and performance parameters.

	Minimum Feature Size (µm)	**Layer Thickness (µm)**	**Build Volume (mm^3)**	**Vertical Build Time (mm/s)**
Light Source	1			3
Conditioning Optics	1			1
Pattern Light	9		9	
Projection Orientation	9	1		9
Imaging Optics	9		9	
Recoat Method	9	3		9

2.3.MPμSL System Components

In this section, the authors analyze possible solutions to the MPμSL sub-functions presented in Figure 2-2 and Table 2-1. The design considerations (Figure 2-1) for each solution are also detailed.

2.3.1. Light Source

There are three performance criteria that are particularly important for selecting a light source for MPμSL applications:

- The *emission spectrum* of the light source must include the wavelength required by the selected photopolymer to achieve photopolymerization.
- The *intensity of light* at that wavelength must be great enough to reach the photopolymer's critical exposure in a reasonable amount of time (e.g., < 60 seconds). This is a key factor in determining system build speed.
- The *divergence* and *intensity profile* of light determine the conditioning and imaging optics required to generate a focused image of homogenous intensity.

Lamp-based light sources reflect light emitted in all directions from a bulb into a light guide. These lamps output high intensity, broad-spectrum light often ranging between 350nm and 500nm. For this reason, lamp light sources are compatible with a wide variety of photopolymer resins of different wavelength sensitivities. Lamp-based light sources are the most commonly used light source for exposing photopolymers in MPμSL systems [4]–[9], [14], [30]–[37].

Light Emitting Diode (LED) sources are also used in MPμSL systems [3]. In general, LED sources have longer operating lives, lower cost, smaller package size, and lower heat generation than mercury lamps and lasers. LED sources generally output lower light intensities than lamps at one or more wavelengths, which may be chosen to match the photopolymer's polymerization wavelength. LED sources are therefore more energy efficient than mercury lamps and lasers, using energy more efficiently to photopolymerize the same volume of photopolymer [3].

Lasers have also been used in MPμSL systems [1], [2], [10]–[13]. Laser light sources may emit light at a single wavelength or across multiple wavelengths. Lasers are available in

ultraviolet, visible, and infrared wavelengths, but often cost thousands of dollars more than the other two light source options.

2.3.2. Conditioning Optics

The system of optical components between the light source and dynamic mask generator is referred to as the conditioning optics (Figure 2-1). These optical components change the properties of the original light source before reaching the dynamic mask. Unfortunately, published MPμSL systems underreport the specifics of these optical components, so it is difficult to discuss them in great detail. However, commonly mentioned components include:

- *Homogenizing rods* that internally reflect light repeatedly to create even intensity profiles. Light without a homogenous intensity profile fabricates inconsistent layer thicknesses along the projected image. These inconsistencies will compound and create dimensionally inaccurate parts [5], [37].
- *Collimating lenses* may be used to collimate a highly diverging source such as a lamp. Well collimated light diverges very little, preventing unwanted beam divergence and the resulting decrease in light density [4], [6]–[9], [30], [31], [36], [38].
- *Filters* may be used to remove unwanted wavelengths, isolating the desired wavelength [4], [6]–[9], [30], [31], [36], [38].
- *Beam expanding optics* may be used to expand already collimated light from an LED, laser, or collimating lenses [1], [2], [10]–[14].

Different light sources produce different levels of collimation and homogeneity. Lasers produce the most collimated light with the most homogenous light intensity. Lamp light sources often possess a Gaussian intensity distribution and non-collimated, widely diverging light. It is the authors' experience that LED light sources are often less collimated than lasers and possess periodic drops in intensity distributions originating from their diodes.

Using the optical components listed above, the collimation and homogeneity of lamp and LED light sources can be improved; however, it is difficult to achieve the same level of performance as a laser.

2.3.3. Pattern Light

A dynamic pattern generator digitally patterns and projects the conditioned light. Dynamic masks all operate by discretizing light over a 2D array of pixels, each individually controlling the light's path. Important design considerations of the dynamic mask include its resolution, pixel pitch, and transmission. Dynamic masks are used primarily in the digital display industry and come in standard resolutions (e.g., 800x600, 1024x768, and 1920x1080). The pixel pitch represents the size of each pixel and the space between pixels. Because optical magnification must be uniform, the resolution and pixel pitch determines the ratio between the projected image area and the minimum feature size. This limitation can only be overcome by moving the mask in relation to the build platform, such that images are stitched together in the photopolymer [4]. Digital Micromirror Device (DMD), Liquid Crystal Display (LCD), and Liquid Crystal on Silicon (LCoS) technologies have been used as dynamic masks throughout MPμSL.

2.3.3.1. Liquid Crystal Display (LCD)

Early MPμSL systems were implemented using LCD devices as the dynamic mask [1], [2], [10]–[14]. LCD chips digitally pattern light by switching pixels between opaque and transparent states, achieved by controlling the orientation of the liquid crystal molecules comprising the pixel. However, the original LCD devices were not designed for use with UV light, and only transmit about 12.5% of UV light [5].

2.3.3.2. Digital Micromirror Device (DMD)

Given LCD's limited UV transmission, the DMD was used almost exclusively in MPμSL systems after 1999 [4]–[10], [30]–[34], [36]–[39]. DMD's discretize light over a 2D array of aluminum micromirrors that are individually actuated between on and off orientations ($\pm$12 degrees) by electrostatic forces applied at their hinges. The DMD offers many advantages when compared to other available dynamic masks:

- The DMD has small pixel sizes and narrow gaps between pixels. Because of this, DMDs are designed with greater pixel density and can reflect incident light with a more

uniform intensity (less light is lost in the gaps). Therefore DMDs have a higher filling ratio (reflective area/total area) compared to LCDs: 91% versus 57% [5].

- The modulation speed between states for individual pixels is also much less for DMDs as compared with LCDs: 20µs versus 20ms. This allows for greater control of exposure time and an increased ability to modulate individual pixels as to achieve gradient, grayscale projection and digitally modulate the intensity of reflected light [5].
- The mirrors of the DMD are surfaced with aluminum that reflects approximately 88% of the incident light, while LCDs typically transmit only 12.5% of incident light. DMDs are therefore more efficient at patterning light and require less powerful light sources, reducing system cost and complexity [5].

2.3.3.3. Liquid Crystal on Silicone (LCoS)

Liquid Crystal on Silicone (LCoS) devices are a reflective version of LCD technologies. LCoS chips possess a 2D array of liquid crystals between one transparent thin-film transistor (TFT) and one silicon semiconductor. The transparency of each pixel is controlled by the applied voltage just as in LCD chips. Unlike LCD, the opaque pixels pass light to the underlying reflective coating to project a pattern. Blocked light is reflected in a different direction. Unlike a DMD, the reflective surface is static while the liquid crystals determine the reflection of light [3].

LCoS devices possess many of the same advantages over LCD devices as DMD devices. LCoS devices generally have higher fill rates and smoother reflective surfaces than the DMD. Unfortunately LCoS chips have poor contrast ratios and do not produce deep blacks. In MPµSLA, projected images will have a base level of intensity even in areas that are meant to be absent of light. This may unintentionally cure photopolymer and may even encourage the development of artifacts or otherwise restrict dimensional accuracy within the cross section. Furthermore, LCoS chips are difficult and expensive to manufacture making their availability and cost to performance ratio less than that of DMDs [40].

2.3.4. Imaging Optics

The optical components that modify the projected image are regarded as the imaging optics. This series of lenses is typically designed with the intention of capturing the light projection transmitting from the pattern generator and focusing it on the build surface. By choosing lenses with specific focal lengths and numerical apertures, a desirable reduction ratio can be achieved.

The reduction ratio is what determines the achievable resolution and working area, but there is a tradeoff between the two characteristics. A higher reduction ratio (lower magnification) means that higher resolutions are achievable, but this reduces the overall projection area and results in smaller part sizes. System magnification can be calculated using lens equations. For example, Choi explains for a system with a magnification of 0.434, one pixel on the DMD (pitch of 13.68 μm) would reduce to approximately 5.9 μm on the resin surface [30]. This constitutes the physical limit of the X-Y resolution of a system, provided that the recoat method or print orientation does not inhibit achievable feature sizes.

2.3.5. Recoat

There are several methods for reapplying resin to the build surface. The methods include recoating by gravity, by spreading, by pumping and by dipping (Figure 2-2).

Recoat by dipping is the most commonly used method for recoating in microstereolithography. In this method, the build platform is dipped below the resin surface to exactly one layer thickness depth. That layer is cured, and the stage descends into the vat of photopolymer, which allows for fresh uncured resin to flow over the previously created layer. The stage then returns to a location where the previously cured layer is exactly one layer thickness below the resin surface [4]–[8], [30]–[33].

Recoat by gravity is used exclusively in bottom-up projection systems (explained further in section 3.6). Unlike the dipping process when projecting from above, the build platform is

raised by the z-axis actuator to create a gap between the platform and the resin container for the next layer. If the photopolymer has a low viscosity, it will flow into the created gap. If the photopolymer has a high viscosity, the platform needs to be raised to an exaggerated height such that the photopolymer can fill the gap. The z-axis actuator than moves the platform down until the desired layer thickness gap is achieved, while extra photopolymer is forced to the sides [39]. Hypothetically, pumping the resin into the created gap could assist the recoat process when the viscosity is too high.

Recoat by pumping is used rarely and does not refer specifically to a recoat practice. Systems that utilize pumping in the recoat process typically are paired with a dipping process. One instance of pumping identified in literature is a syringe pump that purges uncured resin from the build surface with a high density "filler" material to prepare for the next layer [34]. In a multi-material system developed by Choi, a "deep dip" process is imitated through precise and extensive pumping [38].

Wiping or spreading uncured resin for recoating is a method common in stereolithography practices [41], but is seldom used in microstereolithography. However, some MPμSL systems utilize a squeegee or wiping system to recoat or level the resin surface [35].

2.3.6. Projection Orientation

When deciding upon a base design for a microstereolithography system, besides the dynamic mask, one of the most critical considerations is the orientation in which the system will be projecting light on the build surface. Typically, there are two orientation options as shown in Figure 2-3: a top-down approach where the path of light is projected from above onto the resin surface (also referred to as "from above" projection orientation) and a bottom-up approach where light is projected through the bottom surface of vat through a transparent window (also referred to as "from below" projection orientation).

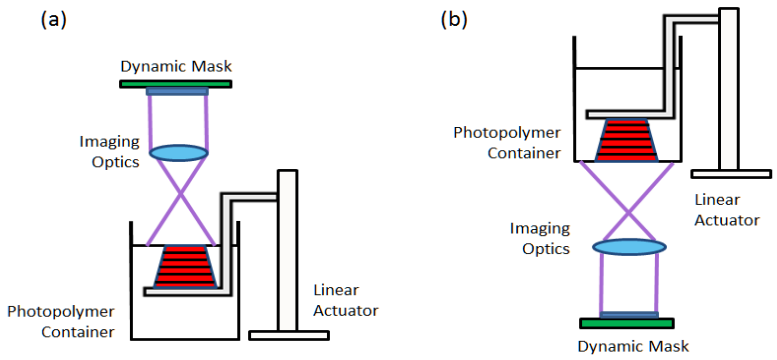

Figure 2-3: Illustration of different projection orientations: (a) image projection from above and (b) image projection from below.

2.3.6.1. Projecting from above

Typically the slower and more common of the two possible system orientations, projecting from above generally utilizes the dipping method to recoat the part. This approach demands that a designer account for resin characteristics, such as surface tension, viscosity, and wetting, to tune the process and achieve the desired layer thickness. In addition, these characteristics affect polymer settling time, which along with actuator speed, directly influences the process throughput.

In an effort to reduce recoat times, vibration assisted leveling has been experimented with to encourage quicker leveling time of the photopolymer and to obtain thin layers [27], [33]. Also, as mentioned in Section 3.5, Takahashi provides one instance in which a squeegee mechanism is used for adjustment of the resin surface in MPµSL [35]. However, as high resolution is generally in the scope of the top-down design, this type of recoat is avoided as sweeping motions may be enough to agitate the resin or catch the part, destroying the print entirely.

2.3.6.2. Projecting from beneath

Projecting images through the bottom of the photopolymer container offers several advantages over projecting images from above the container.

- Less photopolymer is required in the reservoir. Because the build part is not submerged in photopolymer as when projecting from above, the reservoir container is independent of part height and can be shallower. Less photopolymer can save time and/or reduce cost.
- System complexity decreases while the overall vertical print speed increases. When projecting from below, gravity is used to more quickly move and settle the photopolymer. Therefore it is unnecessary to implement recoating mechanisms like squeegees or long waiting periods for photopolymer to settle.
- Thinner layers are theoretically possible. Achievable layer thickness in this orientation is determined by the gap between the previously printed layer and the floor of the container, which is directly limited and controlled by the resolution of the vertical actuator of the build platform.
- Photopolymer can polymerize faster because it is removed from ambient oxygen that would otherwise inhibit crosslinking.

As photopolymer cures between the floor of the resin container and the previous layer, it adheres strongly to both. Forces upwards of 50N must be applied to overcome this adhesion and move the build platform, destroying smaller features in the process [39]. Therefore, there is an inherent tradeoff between printing speed and printing resolution for MPμSLA machines.

Researchers have developed a peeling process that is used when projecting underneath to alleviate feature destruction caused by separation. In this process either the build tray or resin vat is separated from the other by applying a gradual peeling force (like tape from a table). This process reduces the separation force greatly, preserving features smaller than using the same system without peeling. Unfortunately, the peeling process may prolong total build time and negate the inherent speed advantage. Chen's research group, however, has developed a fast mask projection stereolithography process that bypasses this design tradeoff by applying a flexible silicone membrane to the floor of the resin container [39]. This SYLGARD silicone gel maintains a thin oxidation layer directly on its surface, inhibiting photopolymerization so that a substantially smaller adhesion force is developed. The membrane is also flexible so that the

polymer container can slide easily under the build part, to another fresh section of photopolymer (in the same container) for the next layer to cure. This process emulates a peeling step but with much smaller displacements and applied forces, making the impact on overall print speed negligible.

2.4.Categorization and Analysis of MPμSL Systems

The morphological matrix introduced in Figure 2-2 provides a basis on which existing MPμSL systems can be analyzed. The existing systems are presented in this section via a categorization based on the critical architectural components of each system. Each morphological matrix is accompanied by a corresponding table that specifies the systems' respective performance parameters. Together, this data provides a basis for determining the effect of system design decisions on critical performance parameters.

2.4.1. First Generation – LCD MPμSL Systems

Bertsch, Chatwin, and Monneret published the first MPμSL systems. These systems all use beam expansion for their conditioning optics, LCD masks to pattern light, project images from above the photopolymer, reduce the projected image in size, and recoat photopolymer by dipping. This design architecture is illustrated in Figure 2-4 using the morphological matrix previously present in Section 2.2, performance parameters are included in Table 2-2.

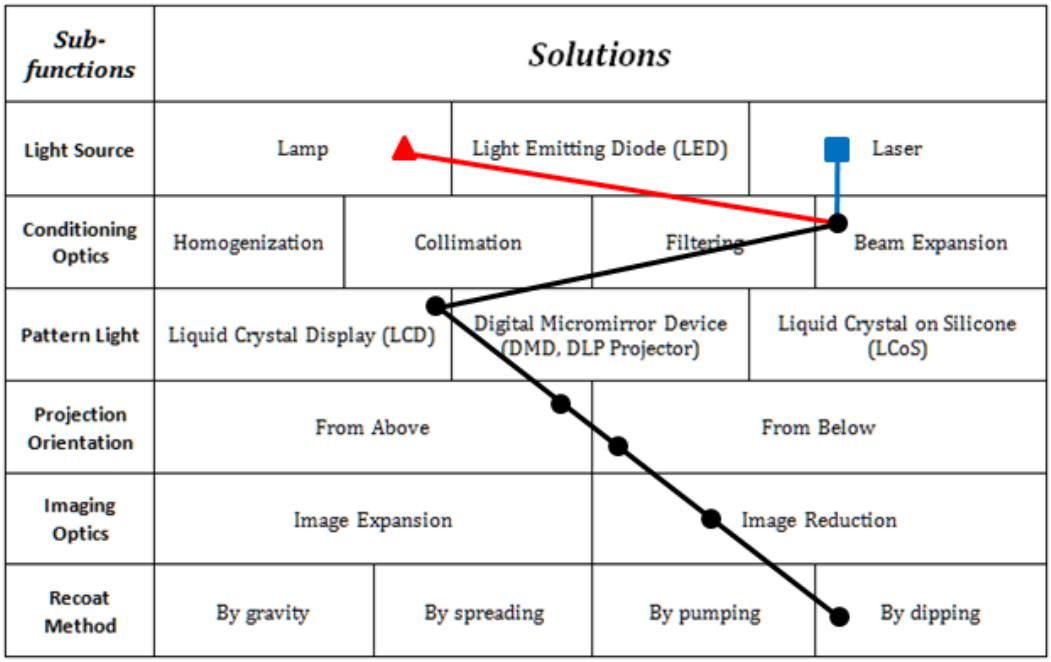

Figure 2-4: Morphological matrix categorizing MPµSL machines that use a LCD pattern generator to project images from above the build platform.

Table 2-2: Performance parameters for the MPµSL systems categorized in Figure 2-4.

	Ref	Research Group	Year	Special Features	Min. Feature Size	Min. Layer Thickness	Maximum Part Size	Vertical Build Rate
■	[19], [20]	Bertsch	1997	LCD,Laser, 515 nm	5 µm	5 µm	1.3 x 1.3 x 10 mm^3	110 layers in 90 minutes
■	[27]–[30]	Chatwin	1998	LCD,Laser, 351.1 nm	5 µm	Not reported	50 x 50 x 50 mm^3	60 second exposure per layer
▲	[31]	Monneret	1999	LCD,Lamp, 530nm	5 µm	10 µm	3.2 x 2.4 x 1.3 mm^3	60 layers per hour

All of these machines are capable of producing 5 µm minimum feature sizes with layer thicknesses ranging from 5 to 10µm. The machines published by Bertsch and Monneret are particularly noteworthy because they use visible light to cure photopolymer. Future MPµSL research moved away from visible photopolymers in favor of curing with UV light. Exposure

times for these machines varied, but were roughly 60 seconds per layer on average. The following section introduces second generation MPµSL systems.

2.4.2. Second Generation – DMD MPµSL Systems

The systems categorized in this section use a DMD to dynamically shape the projected image. These systems were grouped together in order to identify the paradigm shift in design decisions with the advent of the DMD. As outlined in Section 3.3.2, the transition from LCD to DMD was a result of better performance characteristics such as smaller pixel sizes, narrower gaps between pixels, higher modulation speeds, and high reflectivity. The morphological matrix presented in Figure 2-5 represents systems that utilize a lamp, DMD dynamic mask, from-above projection, image reducing optics, recoat by dipping, but employ unique conditioning optics.

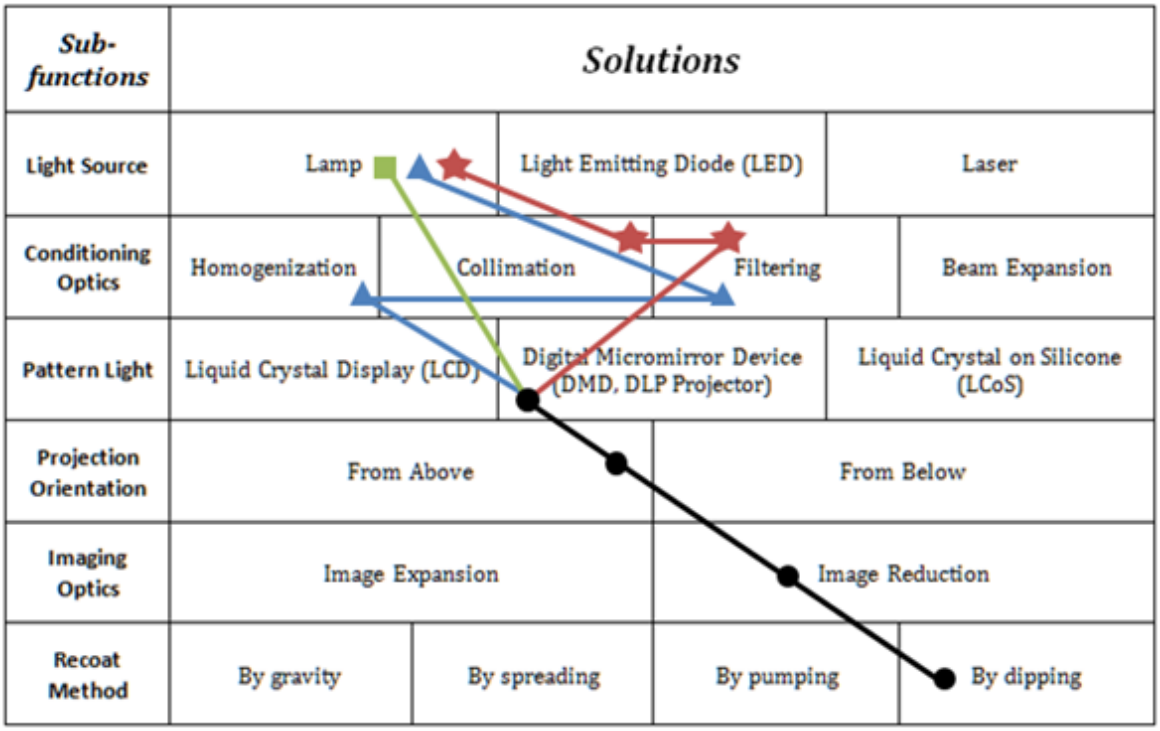

Figure 2-5: Morphological matrix categorizing MPµSL machines that use a DMD pattern generator to project images from above the build platform.

Table 2-3: Performance parameters for the MPµSL systems categorized in Figure 2-5.

	Ref	Research Group	Year	Special Feature	Min. Feature Size	Min. Layer Thickness	Maximum Part Size	Vertical Build Rate
★	[6]	Rosen	2007	DMD, 365 nm	6 µm	400 µm	2 x 2 x 1 mm^3	90s per layer
★	[7]	Rosen	2007	DMD, 365, 435, 647 nm	5 µm	5 µm	not reported	60s per layer
★	[30]	Wicker	2009	DMD, 365 nm	30 µm	4 µm	1.95 x 1.95 x 2.4 mm^3	<1s per layer
★	[4]	Lee	2008	DMD, 365nm, XY translation	2 µm	5 µm	10 x 10 x 2.68 mm^3	100s per layer
★	[8], [9]	Bertsch	1999	DMD, visible	5 µm	5 µm	6 x 8 x 15 mm^3	700 layers in 2.5 hours
★	[31], [36]	Bertsch	2000	DMD, UV	10 µm	10 µm	10.24 x 7.68 x 20 mm^3	200 layers in 1 hour
▲	[5]	Zhang	2005	DMD, 364 nm, fly-eye lens	0.6 µm	5 µm	not reported	not reported
■	[32]	Roy	2006	DMD, 355 nm	20 µm	150 µm	not reported	90s per layer
■	[33]	Hadipoespito	2003	DMD, 365 nm	20 µm	100 µm	not reported	not reported

As seen in Table 2-3, the reported achievable feature size of the DMD projection from above systems utilizing the dipping recoat method ranges from 0.6 to 30 µm. While smaller feature sizes were achieved with DMD based systems, the average achievable feature size is not significantly smaller than LCD systems. Unfortunately, the vertical build rate metric for many of these systems are not comparable as many publications use different speed metrics (as discussed in Section 2.3). Regardless, all systems in Figure 2-4 and Figure 2-5 use the dipping recoat method, and their build times seem comparable. However, as LCD masks transmit only 12.5% of UV light (as mentioned in Section 3.3.1), build time can increase by a factor of 7 when compared to systems using a DMD with the same light source.

Figure 2-6 and Table 2-4 presents systems using a DMD dynamic mask to project images from above, while employing alternative solutions to achieve recoating.

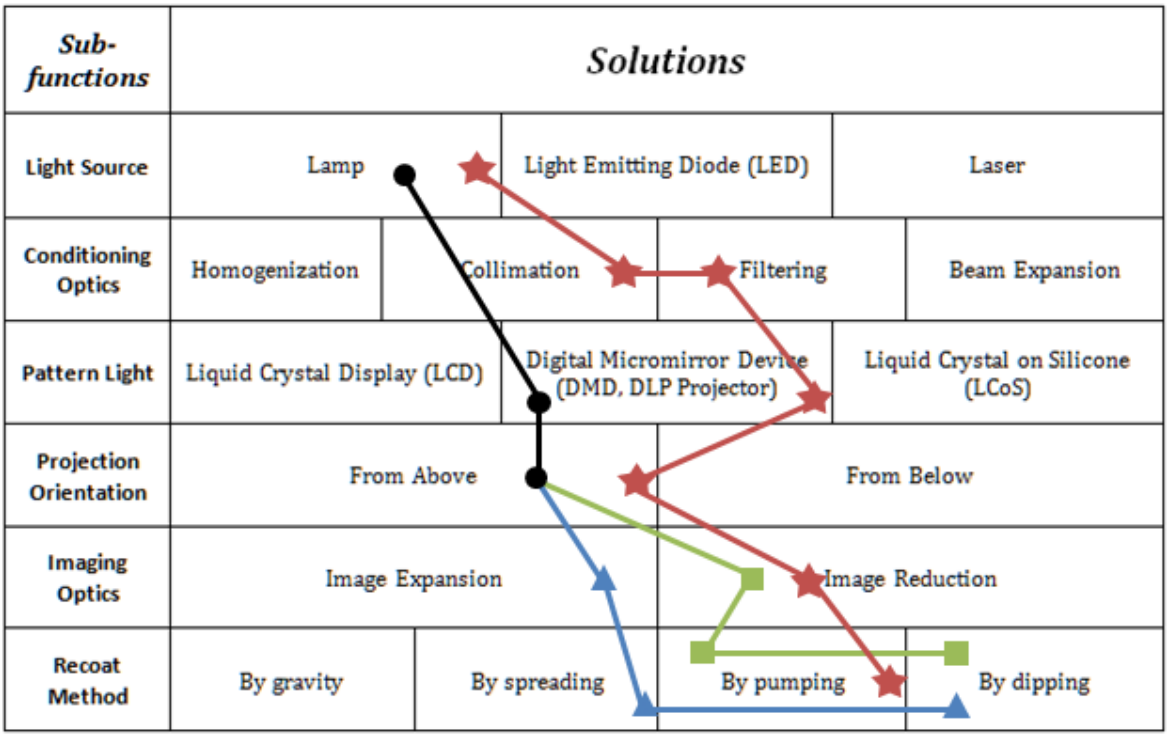

Figure 2-6: Morphological matrix categorizing MPµSL machines that use alternative recoat methods.

Table 2-4: Performance parameters for the MPµSL systems categorized in Figure 2-6.

	Ref	Research Group	Year	Special Feature	Min. Feature Size	Min. Layer Thickness	Part Size	Vertical Build Rate
★	[38]	Wicker	2009	DMD, 365 nm, multi material	~50 µm	21 µm	~ 2 x 2 x 4 mm^3	8-12s per layer
▲	[35]	Takahashi	2000	DMD, 365 nm	50 µm	200 µm	~ 2 x 2 x 2 mm^3	not reported
■	[34]	Roy	2008	DMD, 355 nm	50 µm	50 µm	not reported	60s per layer

Comparing the systems' performances listed in Table 2-2 and Table 2-3 versus Table 2-4 (which primarily differ by recoat method) suggests that systems that do not use recoat by dipping generally have larger minimum feature sizes (approximately 50 µm) and layer thicknesses ranging from 21 µm to 200 µm. This indicates that dipping may be the preferable method for recoating if the goal of system is to achieve a minimum feature sizes (as discussed in Section 3.5).

2.4.3. Third Generation – From Below Projection

As the embodiment of second generation systems became a standard, some researchers have begun experimenting with alternative projection orientation in the effort to reduce build time. The system architecture presented in Figure 2-7 and Table 2-5 is unique as it projects from below and recoats by gravity.

Sub-functions	*Solutions*			
Light Source	Lamp	Light Emitting Diode (LED)	Laser	
Conditioning Optics	Homogenization	Collimation	Filtering	Beam Expansion
Pattern Light	Liquid Crystal Display (LCD)	Digital Micromirror Device (DMD, DLP Projector)	Liquid Crystal on Silicone (LCoS)	
Projection Orientation	From Above	From Below		
Imaging Optics	Image Expansion	Image Reduction		
Recoat Method	By gravity	By spreading	By pumping	By dipping

Figure 2-7: Morphological matrix categorizing MPµSL machines that use a DMD pattern generator to project images from below the build platform.

Table 2-5: Performance parameters for the MPµSL systems categorized in Figure 2-7.

	Ref	Research Group	Year	Special Features	Min. Feature Size	Min. Layer Thickness	Maximum Part Size	Vertical Build Rate
●	[39]	Chen	2012	DMD, Lamp, visible	400 µm	100 µm	48 x 36 mm^2	180 mm per hour
▲	[37]	Kang	2012	DMD, Lamp, UV	Not reported	Not reported	14.6 x 10.9 mm^2	Not reported

The feature sizes reported in Table 2-5 are much larger than those of the systems listed in the Tables 2-4, but the part size is also much larger. The print speed is the quickest of all systems analyzed [39]. This suggests that projecting from below is indeed quicker, but cannot achieve the resolution of top down projection systems. Work in this system embodiment still developing, and there is room for further improvement based on the performance parameters advantages.

2.4.4. Alternative Embodiments

The last system is unique in that it is the only published system that utilizes an LED light source, and is the only published system that uses an LCoS device to digitally pattern light. Figure 2-8 and Table 2-6 outline this system and characterizes its performance.

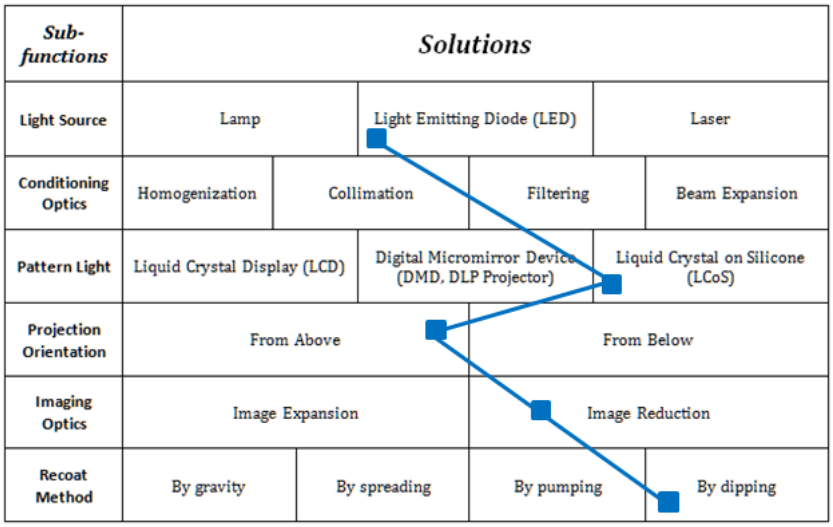

Figure 2-8: Morphological matrix categorizing MPµSL machines that use a LCoS pattern generator to project images from above the build platform.

Table 2-6: Performance parameters for the MPµSL systems categorized Figure 2-8.

	Ref	Research Group	Year	Special Features	Min. Feature Size	Min. Layer Thickness	Maximum Part Size	Vertical Build Rate
■	[3]	Zheng	2012	LCoS, LED, 395nm	1.3 µm	10 µm	2.56 x 1.44 mm^2	Not reported

This unique system achieves very small feature sizes, comparable layer thickness and part size of other projection from above, recoat by dipping systems. It follows the trend that high resolution is achievable by combining recoating via dipping with the top-down orientation.

2.5. Closure

This chapter presents a MPµSL morphological matrix that is designed to functionally categorize and compare the fundamental design decisions solved in the realization of MPµSL systems. Using this matrix, several published MPµSL systems are analyzed in terms of critical MPµSL performance parameters: minimum feature size (µm), layer thickness (µm), build volume (mm^3), and vertical build time (mm/s). These performance parameters are expressed in units that serve as a standard benchmark to promote direct quantitative comparisons between MPµSL systems. From this analysis, relationships between system performance and the corresponding subsystems solutions have been identified to indicate general trends and tradeoffs.

- The most common system embodiments project images from above the photopolymer container and dip the build platform to achieve recoating. These systems are capable of achieving the smallest feature sizes, which are close to 1 µm.
- Dynamic mask selection does not significantly affect the minimum achievable feature size. While pixel pitch is a relevant design consideration, final feature size is ultimately determined by the imaging optics.

- Dynamic mask selection significantly affects the vertical build rate of a MPμSL system. LCD masks transmit only 12.5% of UV light, which can increase build time by a factor of 7 when compared to using a DMD with the same light source.
- The relationship between part size and feature size is equivalent to the relationship between aspect ratio and pixel pitch for any dynamic mask. Future dynamic masks with an equivalent pixel pitch but with greater resolution will enable creation of smaller feature sizes on equally sized parts, or the same feature sizes on larger parts.
- If a fast vertical build rate is priority, then system embodiment should project images from below the photopolymer vat. By using a gravity-assisted recoat approach, vertical build rates can be improved by an order of magnitude.
- The type of light source is noncritical provided that emission properties (wavelength and intensity) are suitable, and appropriate light conditioning is performed.

Amongst published MPμSL systems, design trends have changed historically. Exploration of novel form factors and embodiments has been limited. An area for future research is in exploring more unique embodiments and subsystem solutions. In doing so, the relationships between MPμSL performance parameters and subsystem solutions can be more broadly and quantitatively compared. Ultimately, such relationships could be used to develop processes more optimized for desired performance as governed by the application.

3. Design of a Mask Projection Microstereolithography System

Per the suggestion of the "Design Considerations for Mask Projection Microstereolithography Systems" section presented in Chapter 2, design of this MPμSL system began by identifying the customer needs and target specifications. From there, the embodiment of the system was determined, and components were selected to best meet the target specifications based on the guidelines put forth in Section 2.5.

3.1. Conceptual Design and Solution Selection

The first section of this chapter begins by determining the solutions to the major sub-systems of the MPμSL system. The target specifications are laid out, and the conceptual design is introduced.

3.1.1. Key Requirements

Several key requirements, along with target specifications for each requirement, are listed below for the design of the MPμSL system.

- *System can manufacture 3D structures utilizing vat polymerization*

As the goal of this work is to design an MPμSL system, the resulting machine must be able to use selective light exposure to cross-link photopolymer in a vat polymerization process.

- *System is has a very high resolution*

Mask Projection Microstereolithography is known for its unique ability to project 2D images with high resolution and manufacture very small features, reaching as small or smaller than 5 micrometers [4], [6]–[9]. Thus, the target minimum feature size is 5 micrometers.

- *The build process should be fast*

One of the pitfalls of many 3D printing systems is very slow build times. The benefit of MPμSL is that rather than using the SLA laser scanning method to cure photopolymer, entire 2D contours are projected and the entire layer is cured simultaneously. To harness this ability, the target build rate is 60 layers per hour.

- *The build process should be automated*

Additive manufacturing systems are touted for their ability to fabricate parts at the press of a button. The highest possible degree automation of the build process is desired.

- *System operation is simple*

The system operation and corresponding user interface should be simple. Few intermediate processing steps and user intervention is desired.

3.1.2. Morph chart embodiment

Figure 3-1 is the morphological matrix used to identify the embodiment of the MPµSL system designed for high resolution fabrication. The rationale for the solution chosen for each sub-function is listed below.

Sub-functions	***Solutions***			
Light Source	Lamp	Light Emitting Diode (LED)	Laser	
Conditioning Optics	Homogenization	Collimation	Filtering	Beam Expansion
Pattern Light	Liquid Crystal Display (LCD)	Digital Micromirror Device (DMD, DLP Projector)	Liquid Crystal on Silicone (LCoS)	
Projection Orientation	From Above	From Below		
Imaging Optics	Image Expansion	Image Reduction		
Recoat Method	By gravity	By spreading	By pumping	By dipping

Figure 3-1: The morphological matrix identifying the embodiment of the MPµSL system.

3.1.2.1. Light Source

An LED was chosen as the light source from a price and wavelength standpoint. As light source type is noncritical providing emission properties are appropriate, the cheapest and easiest option was chosen.

3.1.2.2. Pattern Light

To pattern the light, the Digital Micromirror device was chosen. This is the state of the art for image patterning due to its high transmission and high pixel density and is used in most modern systems.

3.1.2.3. Optics

There are no significant conclusions to consider when designing the optics for the system. Conditioning and Imaging optics choices were made to accommodate for the emission properties of the light source and DMD geometrics, respectively.

Conditioning

Collimation optics collimates the light, ensuring constant beam diameter and intensity throughout the light path. The beam emitting from LED light sources are very small in diameter, so a beam expander is essential. Coincidentally, a beam expander also aids in collimation. A filter is used to remove bands of light not being used in the polymerization reaction, and a diffusion lens homogenizes the light beam.

Imaging

The goal of this system is to achieve feature sizes down to 5 microns. As the pitch of DMD micromirrors are on the order of 10 microns, image reduction is necessary.

3.1.2.4. Projection Orientation and Recoat Method

As feature resolution is the primary driver of this system, projection from above with recoating by dipping is the best selection as all alternatives may disrupt the micron sized features being printed.

3.2.System Design and Component Specifications

This section details the system design and component selection for the major sub-functions of a mask projection microstereolithography system.

3.2.1. Pattern Light: DMD Selection and Mounting

The most critical component on a MPµSL system is arguably the dynamic mask generator. The following sections present the design methodology for component selection and mounting.

3.2.1.1. DMD and Development Kit

The goal of this design is to maximize the resolution of the projection and minimize the feature size of the printed part, an end-use developer kit was chosen in lieu of a DLP projector. This allows for greater design freedom for the light path. The chip chosen was the DLP 0.95 1080p Digital Micromirror Device. The DMD is a 1920 x 1080 array of aluminum micrometer-scale mirrors that measures 0.95-inch along the diagonal. The micromirror tilt at an angle of ±12° relative to the flat state, with landed positions called “On-state” and “Off-state”, demonstrated in Figure 3-2. Each mirror has a pitch 10.8µm and rotates between states along the diagonal of the mirror, shown in Figure 3-3

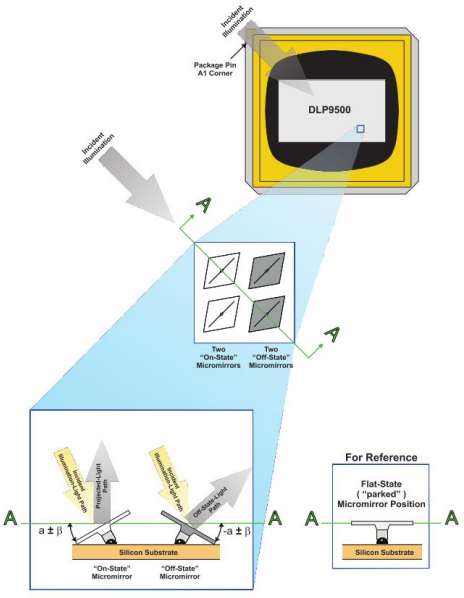

Figure 3-2: DMD landed positions and light paths (Texas Instruments, “DLP ® 0.95 1080p 2 x LVDS Type A DMD,” no. September. p. 29, 2012, Used under fair use, 2014).

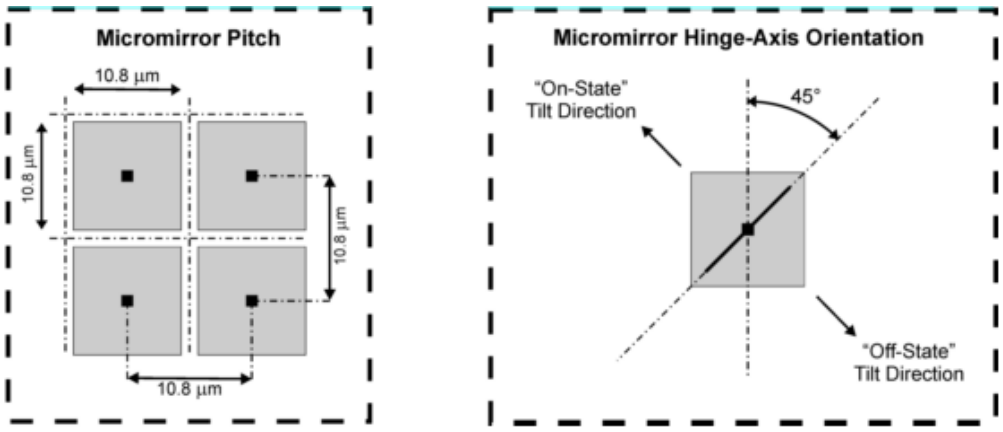

Figure 3-3: DMD micromirror pitch and hinge-axis orientation (Texas Instruments, "DLP ® 0.95 1080p 2 x LVDS Type A DMD," no. September. p. 29, 2012, Used under fair use, 2014).

This particular DMD is designed for use with broadband visible light (400nm to 700nm wavelength) with a window transmission of 97% and mirror reflectivity of 88%. As this DMD is not designed for UV light ranges, significantly more transmission loss is expected (but not documented by TI) [42].

The DMD was purchased as part of a developer kit by Keynote Photonics. This kit, called the FlexLight X1 DLP Development System, consists of a DMD mounted to a microcontroller with embedded source code and HDMI inputs for seamless data transfer [43]. Figure 3-4 shows an image of the Flightlight X1 board with physical dimension.

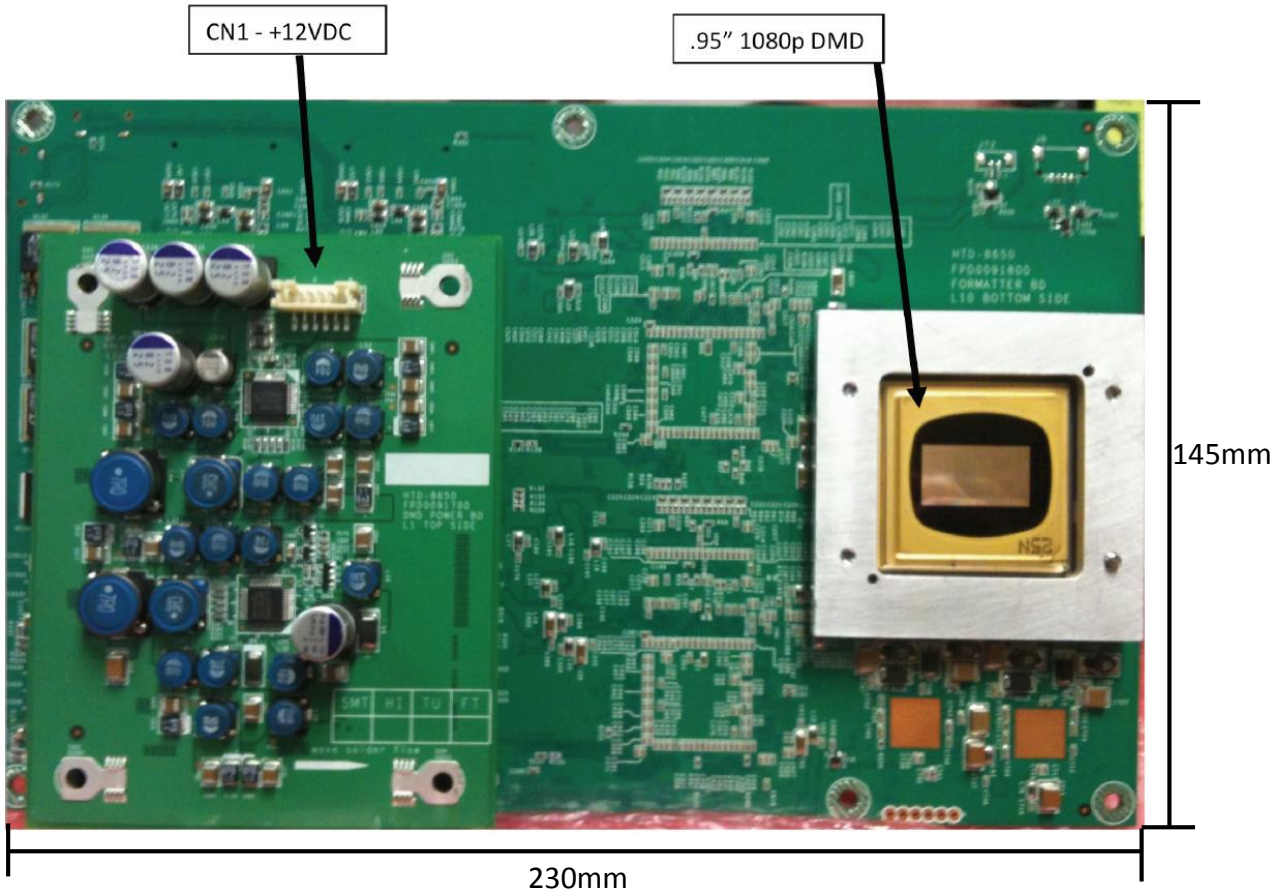

Figure 3-4: Flexlight X1 DLP Development System with physical dimensions (Keynote Photonics, "FlexLight ™ X1 DLP ® Development System Open Platform DLP ® Technology." pp. 1–2, 2012, Used under fair use, 2014).

3.2.1.2. DMD Mount design

In order to securely support the FlexLight X1 such that it can be properly oriented in the system, a custom mount was designed. This mount features two axes of rotation oriented around the center of the DMD chip, such that adjustments can be made to align the DMD projection with imaging optics and the resin surface. The orientation of the DMD mount was fixed with set screws that mated tapped holes. The mount was machined with Aluminum 6061. A render of the aluminum mount, with a model of the FlexLight X1 mounted, is show below in Figure 3-5.

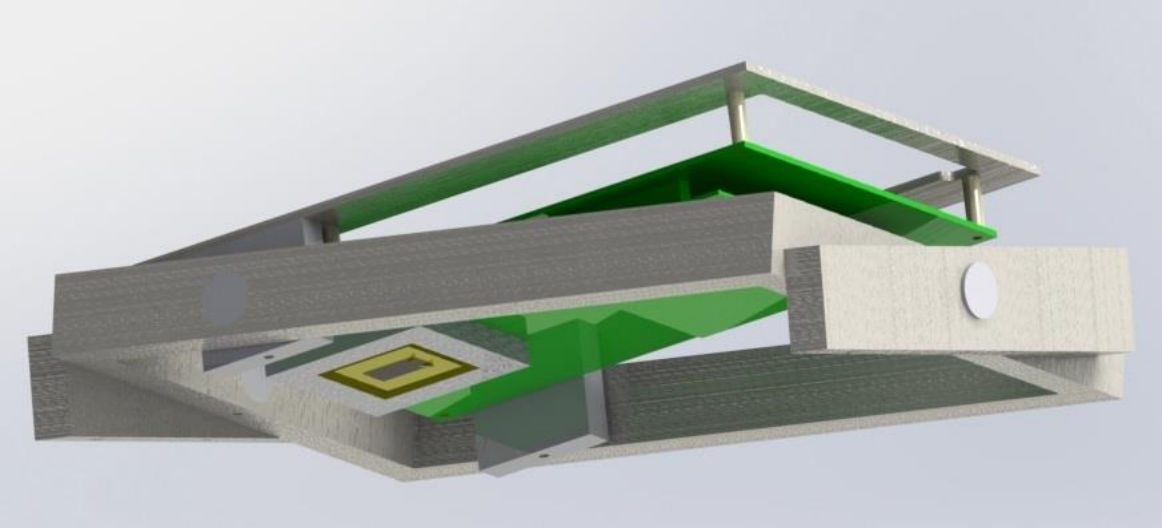

Figure 3-5: FlexLight X1 DMD mount.

3.2.2. Light Source

The light source chosen for this design is the LightningCure LC-L1V3 UV LED system by Hamamatsu. This system was selected due to the availability of a light guide, as well as a selection of head types to match certain applications, including a collimating head attachment. This collimating head reduced the need for an extra collimating optical component, and produces an even intensity of light along a 4mm point at a specified distance from the guide [44]. The radiation intensity profile for the collimating type head is shown in Figure 3-6.

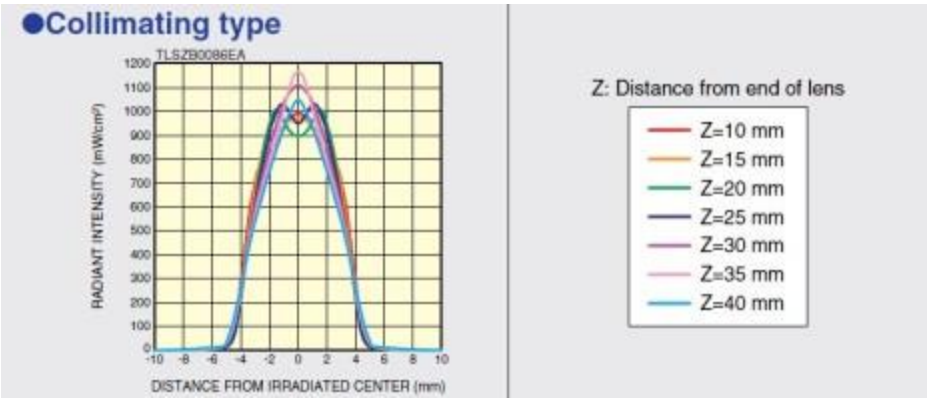

Figure 3-6: Intensity radiation profile for the LC-L1VC at 365nm wavelength (Hamamatsu, "UV-LED Spot Light Source LightningCure LC-L1V3." Iwata City, japan, p. 4, 2012, Used under fair use, 2014).

3.2.3. Optics

The optical systems designed and implemented in this system are explained in the following sections. They are categorized, per the suggestion of the morphological matrix tool in Figure 2-2 into Conditioning Optics and Imaging Optics.

3.2.3.1. Conditioning Optics

Conditioning optics are the optics that prepare the beam of light for reflection off of the dynamic mask and projected onto the resin surface. There are three optical systems that condition the light: Beam Expander, Filter, and Diffuser.

Beam Expander

As the diagonal dimension of the DMD is 0.95", a beam expander was designed to enlarge the 4mm beam from the UV LED to a 25mm beam so the entire surface of the DMD is illuminated. A Galilean telescope, a refracting telescope composed of a positive and negative lens, can function as a simple beam expander for collimated light. In a Galilean telescope, the objective lens is a positive lens and the negative lens is the image lens, separated by the sum of their focal lengths. This design can be used as a beam expander by reversing the direction of collimated light, and having the negative lens serve as the objective lens and the positive lens as the image lens, still separated by the sum of their focal lengths [45] .

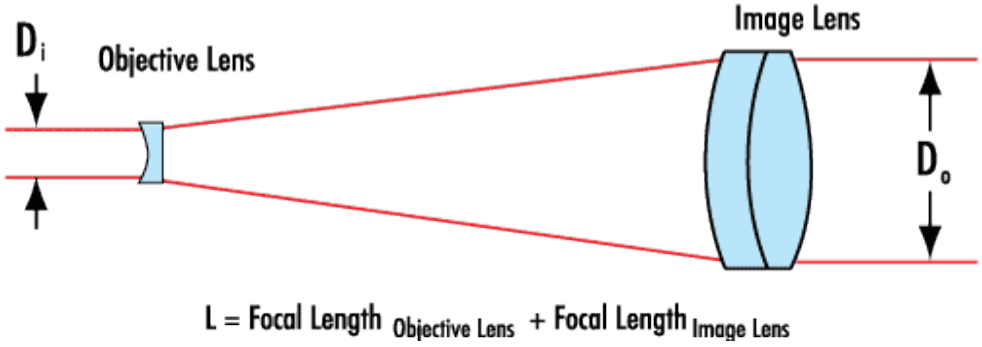

Figure 3-7: Diagram of a Galilean telescope beam expander. Also shown is the equation for the distance between the two lenses in the beam expander (Edmund Optics, "Beam Expanders." [Online]. Available: http://www.edmundoptics.com/learning-and-support/technical/learning-center/application-notes/lasers/beam-expanders/. [Accessed: 17-Jan-2013], Used under fair use, 2014)

An added benefit of a beam expander is that as beam diameter increases, beam divergence decreases. This means by using this optics feature, the divergence of the collimated light will be reduced, allowing for a longer working distance of the collimated light.

Lens choice and rationale

To design the appropriate beam expander that matches the requirements of the system, the following equations were used. To begin,

$$\boldsymbol{MP = \frac{1}{magnification}} \qquad \textbf{Equation 3-1}$$

where MP is magnifying power and

$$\boldsymbol{MP = D_O / D_I} \qquad \textbf{Equation 3-2}$$

where D_O is the output beam diameter and D_I is the input beam diameter. We define magnification as

$$\boldsymbol{magnification = -f_{Objective}/f_{Image}} \qquad \textbf{Equation 3-3}$$

where $f_O$is the focal length of the objective lens (negative lens) and f_I is the focal length of the image lens. Therefore, by substituting magnification into Equation 1 and setting Equation 1 and 2 equal, we have Equation 4:

$$\boldsymbol{\frac{D_O}{D_I} = -\frac{f_{Image}}{f_{Objective}}} \qquad \textbf{Equation 3-4}$$

Since $f_{Objective}$ = -25mm, D_O = 25mm and D_I= 4mm, and solving forf_{Image},

$$\boldsymbol{f_{Image} = -f_{Objective}\, D_O / D_I} \qquad \textbf{Equation 3-5}$$

and therefore $f_{Image} = -(-25)(25/4)$ = 156.25. The -25mm focal length lens was available from Edmund Optics as a UV Plano-Concave 12mm diameter lens (EO #48-050). However, design is limited by lenses that are available by vendors, and the optimal focal length of 156.25

was not an option. The closest lens was a UV Plano-Convex Lens with 150mm focal length and a 50mm diameter. This means that the magnification of the expander is $-f_{Objective}/f_{Image} = -(-25)/150 = .1\overline{66}$, and the inverse of which is a MP of 6, making the output beam diameter 24mm. The distance between the two lenses follow the equation $L = f_{Objective} + f_{Image}$, shown in Figure 3-7, which means the lenses will be 125mm apart on the optical rail.

Filter

The photopolymers in this system cure at 365nm. To isolate this wavelength for testing and characterization purposes, a bandpass filter (EO #65-130) was placed (FWHM of 10nm) directly after the LED head in the path of light.

Diffuser

Testing the LED light source with a UV dosimeter revealed that the beam of light emitted from the head is not as homogenous as expected. In order to homogenize the light, a UV holographic diffuser is placed after the beam expander. The diffusing angle describes how the light diverges when exiting the diffuser, which will negatively affect the collimation. For the chosen diffuser (EO #48-513), the diffusing angle is 0.5°.

3.2.3.1. Focusing Optics

The focusing optics are the optics that focus the DMD generated image and project it onto the resin surface. While the light illuminating the DMD is collimated, the divergence off of the mirror array itself is uncertain (and perhaps indeterminate.) In order to insure that all the light reflecting off of the DMD is projected onto the surface, a lens with a large diameter and a relatively short focal length was needed. However, as the desired final image projection diameter was 0.5" or less, image reduction of ½ is required. To accomplish this, an infinity corrected microscope system was designed.

Lens choices and rationale

Based on the limited availability of 50mm (large diameter) UV Plano-Convex lenses, one with a relatively short focal length was chosen. This first lens, the objective lens, has a 75mm focal length (EO #67-218). In the system, the desired magnification is -0.5, a lens with a focal length

of 150mm was chosen (EO #67-223). The first lens, the objective lens, was placed its focal length away from the DMD, and the image lens was placed its focal length away from the resin surface. The distance between the two lenses is unrestricted, but too great a distance between the lenses will lead to vignetting.

3.2.4. Projection Orientation

To facilitate the projection orientation, a frame was designed to hold the DMD sub-assembly (Flexlight X1, Flexlight X1 mount).

The Flexlight X1 mount was attached to a frame constructed of 80/20 extruded aluminum, which was fastened to the breadboard (Figure 3-8) using L-brackets. The frame was constructed to support the Flexlight X1 Mount above the build area for the “from above” projection. The frame features more L-brackets that support the cross beams so the height of the mount can be changed relative to the breadboard.

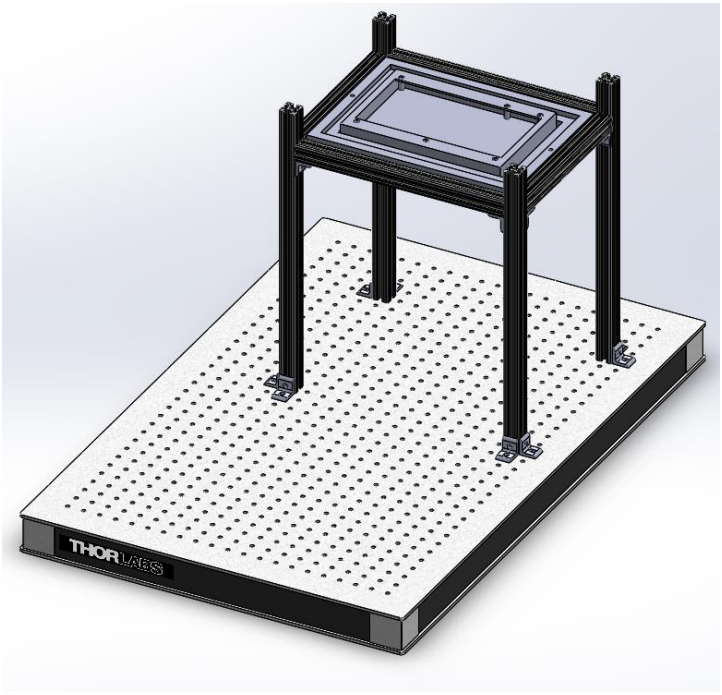

Figure 3-8: The 80/20 Frame attached to the optics table supporting the DMD mount.

3.2.5. Recoat Method

The surface of the resin is refreshed by dipping, sometimes called the “deep dip.” This is accomplished by submerging the surface of the part being printed to a significant depth below the resin surface, and then returned to the build plane. This is accomplished by using a high resolution stepping linear actuator, mounted on a linear slide, to which a build platform is attached.

3.2.5.1. Linear Actuator

The stepper motor, Figure 3-9, used for this system was a linear actuator by Zaber (#NA11B60) with a travel length of 60mm and 15 lb force.

Figure 3-9: Image of the NA11B60 linear actuator used in this system (www.zaber.com, used under fair use, 2014).

The D-sub 15 pin connector was removed, exposing four wires. The wires were stripped and attached to an Allmotion EZ10EN Stepper motor controller paired with an RS485 converter. The converter communicates serial data through a PC com port (via USB) to the controller 4 wire bus. The actuator was attached to the end of a 15cm long linear slide rail that was available in the DREAMS Lab. The mount for the linear actuator is shown in Figure 3-10, which was printed in ABS on the Stratasys Dimension SST 768.

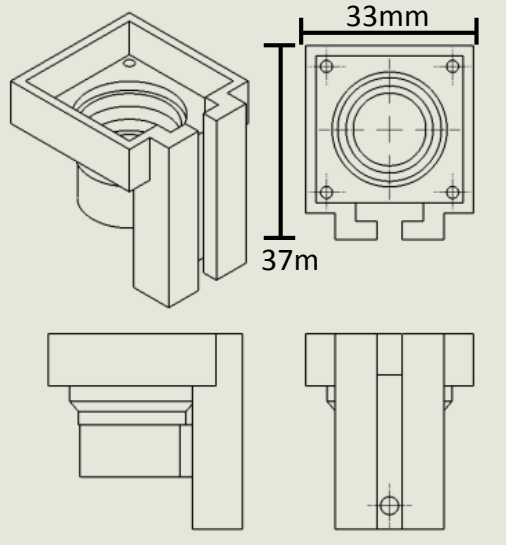

Figure 3-10: Mount for the linear actuator.

An assembly was designed that connected the build platform to the motor. The assembly was also printed in ABS plastic, and features a stage that slides into an adapter, allowing for stage removal and replacement. This design made it easy to remove delicate parts from the build platform. A brass threaded insert was inlaid into the part so a set screw could be used to secure the stage. The stage adapter and stage are presented in Figure 3-11 and Figure 3-12, respectively.

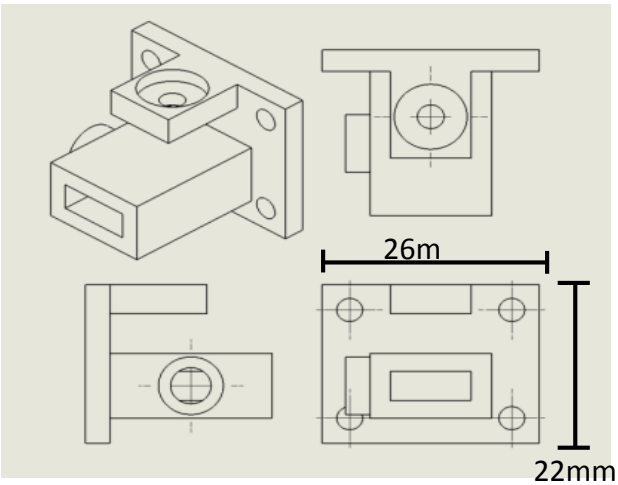

Figure 3-11: The stage adapter, which attaches to the linear actuator using the top tab, holds the stage in the main slide, and attaches to the linear slide with the four mounting holes.

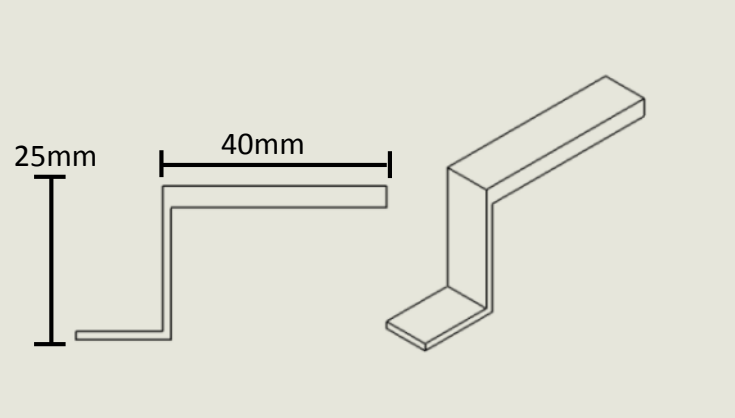

Figure 3-12: The slide-in stage.

The vat in this system is a Fisher Scientific 20 mL beaker. To support this beaker, a vat adapter (Figure 3-13) and slide (Figure 3-14) were designed and printed in ABS plastic. The vat support system is used to insure the vat position is constant and provides a fill-line for the photopolymer.

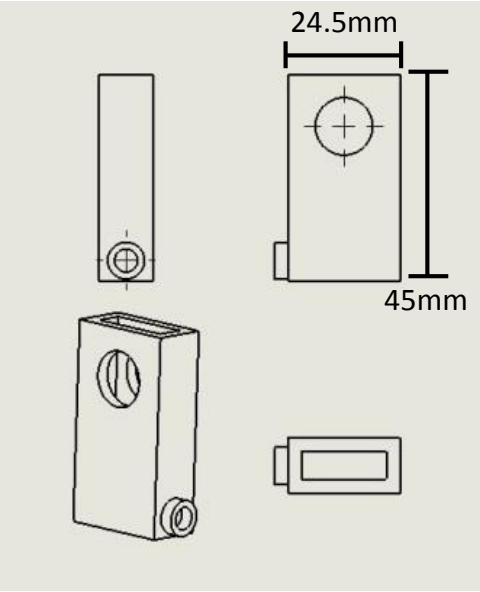

Figure 3-13: The vat slide adapter. A brass insert is embedded in the side hole for a set screw.

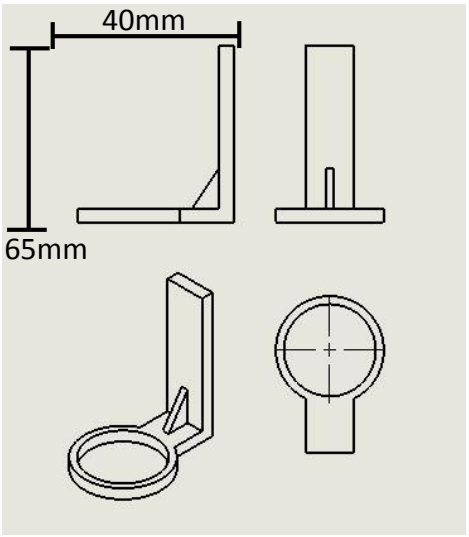

Figure 3-14: The vat slide, which slides lengthwise into the vat slide adapter.

The entire build sub-system assembly, which includes the motor, the linear slide rail, the motor mount, the stage adapter, the stage, the vat, and the vat support, is shown in Figure 3-15.

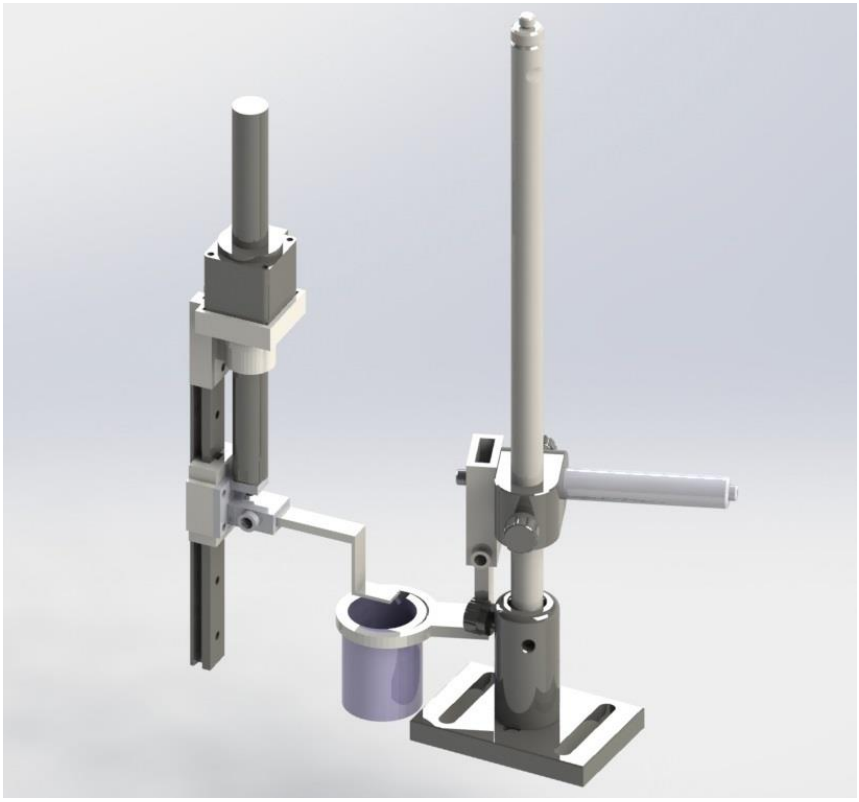

Figure 3-15: A model of the build sub-assembly.

3.2.6. Embodiment

The remainder of the system design does not specifically fall within the context of the morphological matrix. Much of the design from this point forward is highly specific to each individual system and is at the discretion of the engineer.

3.2.6.1. Alignment

This system was designed for high precision, and high precision mounts were needed for alignment of optical components. For this reason, a Performance Series I Breadboard was chosen as a base for the MPµSL system. The breadboard features ¼"-20 tapped holes, spaced at one inch on center, with overall dimensions of 3' x 2' x 2.4". To align the conditioning optical components, a dovetail optical rail was used, paired with rail carriers from ThorLabs. Sets of post holders, mounting posts, and the appropriate optical mounts were assembled for each optical component, and properly spaced out along the optical rail based calculations demonstrated in the Conditioning Optics section. However, due to the abnormal geometry of the Flexlight X1, the alignment holes on the breadboard and the DMD location on the Flexlight X1 did not align precisely. To compensate for this, wedged table clamps were used to attach the optical rail to the breadboard independent of the grid of tapped alignment holes.

3.2.6.2. Light Path

The path of light for the MPµSL system is illustrated in the diagram presented in Figure 3-16. The light is emitted from the UV LED as collimated light. The UV filter removes all bands of light that do not fall within 5nm of the 356nm wavelength. The beam expander broadens the beam of light to 25mm, which then passes through the diffuser to be homogenized. Ideally, at this point, the beam is a 25mm homogenized beam of collimated light. However, empirical testing of the system indicates that the beam is diverging slightly and is not entirely homogenized. Regardless, the beam reflects off a mirror positioned to shine the light on the DMD. The DMD shapes the light, which is focused down to 0.5 times the size of the DMD image at the surface of the photopolymer in the vat.

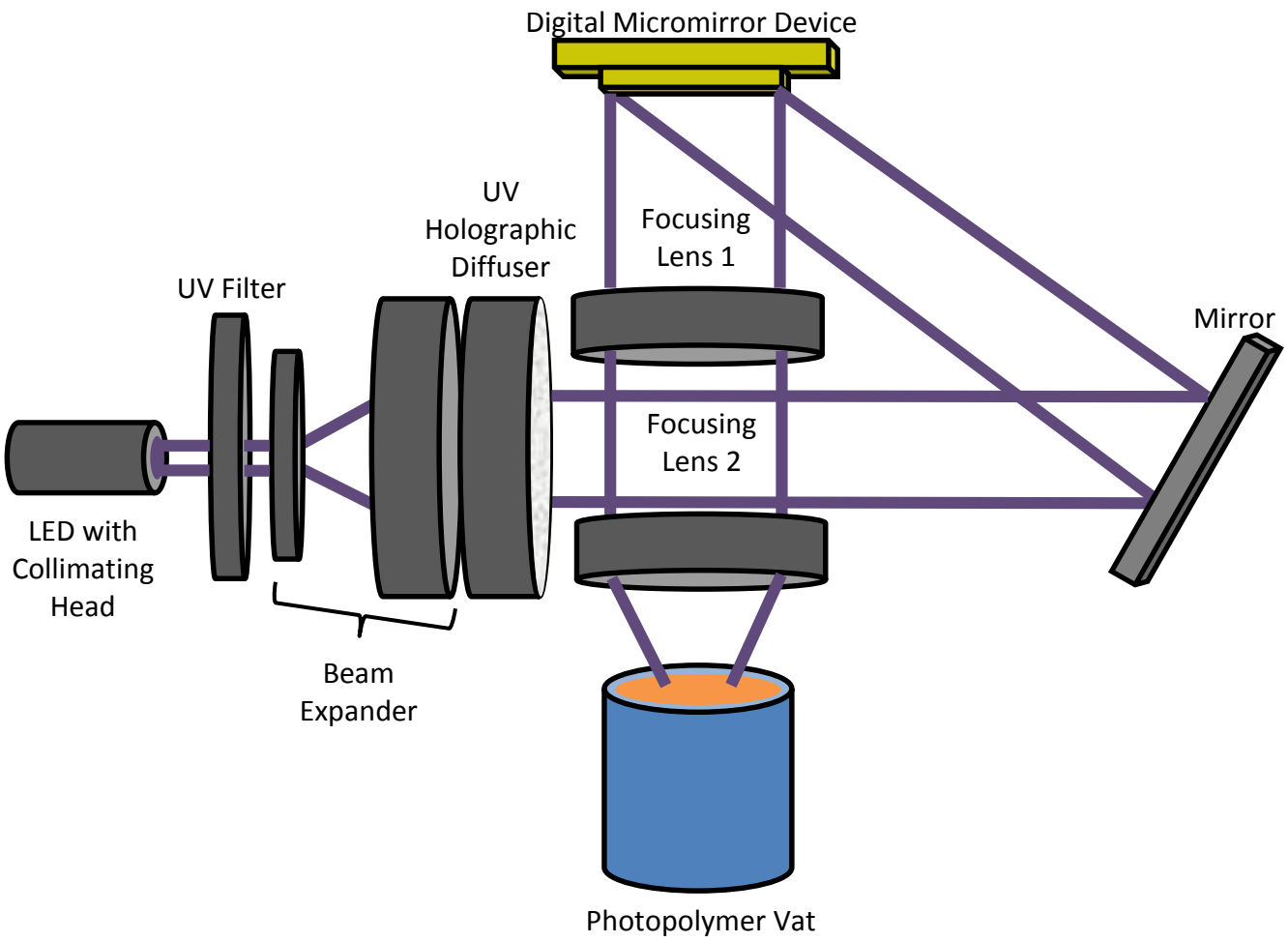

Figure 3-16: Diagram illustrating the path of UV light through the optical components of the MPµSL system.

Mirror Angle

Based on experimentation, the mirror was oriented at 63° from horizontal. This angle was determined by adjusting the mirror angle and observing when the DMD was fully illuminated.

Flexlight X1 Mount Angle

Using the DMD specifications from Figure 3-2 and Figure 3-3, the "ON" angle of the DMD mirror is 12° from horizontal along the diagonal of the mirrors. However, as the DMD is mounted in such a manner that the axis of rotation for the mirrors is not parallel to the axes of rotation for the mount, compensation angles need to be determined so an accurate DMD mount

orientation can be determined. Using trigonometry and the geometry of the mount, which was confirmed in the CAD model, the angles necessary to align the DMD "ON" mirrors parallel to the build surface (the horizontal) are 5.93° along the Y axis, and 10.45° along the X axis. The X axis can be set to 10.45°, but the Y axis orientation is dependent on the angle of the reflecting mirror. The axes are labeled for clarification in Figure 3-17.

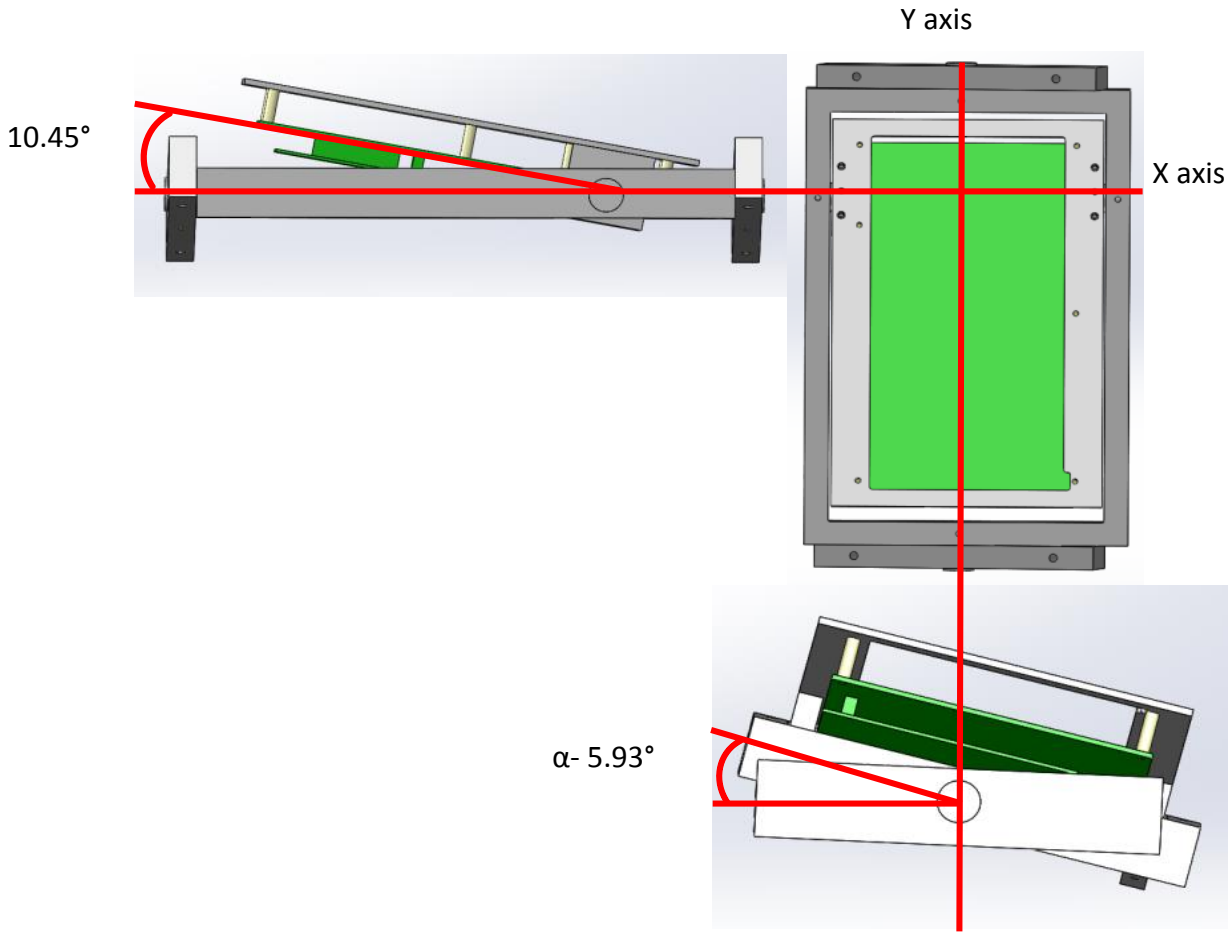

Figure 3-17: Diagram of the Flexlight X1 Mount presenting the names of the axes of rotation.

Figure 3-18 labels the angles critical to orienting the Flexlight X1 mount such that the light is projected perpendicular to the build surface.

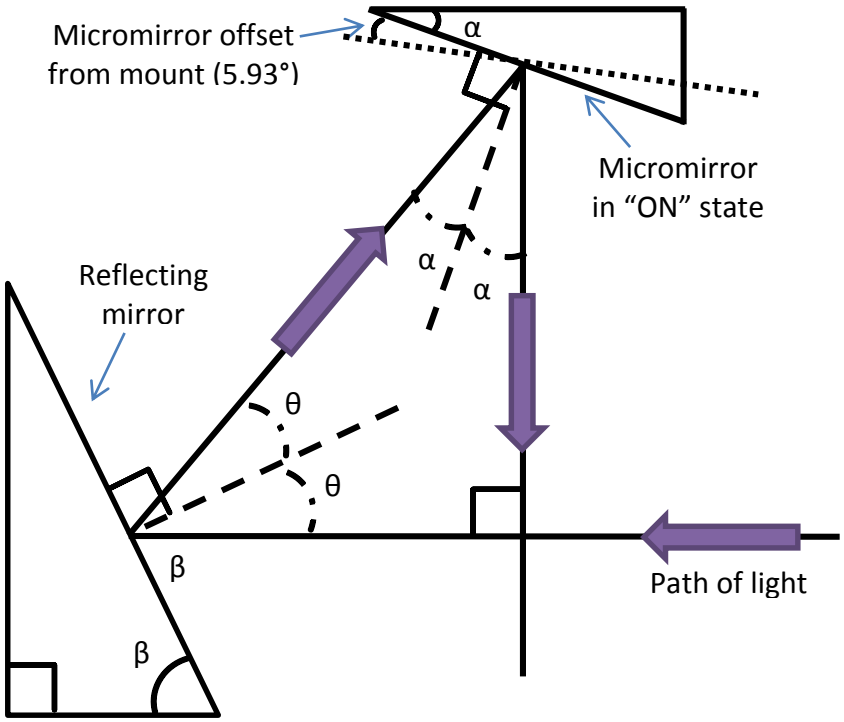

Figure 3-18: Diagram of the path of light as it reflects off the mirror and DMD. Angles are labeled for reference.

As mentioned earlier, the orientation of the mount is reliant on the orientation of the reflecting mirror. The mirror was placed on the optical table at a distance compatible with the geometry of the remainder of the system, while minimizing the horizontal distance between the DMD and the mirror to maximize light intensity. The actual angle was an empirical measurement determined by orienting the mirror such that the light beam fully illuminated the DMD. Later, small adjustments were made to optimize performance, but for the purpose of explaining this orientation process, the angle β was set to 63°. As β is 63°, θ is calculated to be 27°. Furthermore, this means that 2θ is equal to 54° and 2α is equal to 36. Thus, the angle α is 18°. However, compensating for the angle of the "ON" state of the DMD in the Y axis (5.93°), the angle of the Y axis needs to be 12.07° from the horizontal.

3.2.6.3. Final Model

A CAD model was developed to help with design embodiment, and confirm location and angles of components. A render of the final model is below, in Figure 3-19, and an image of the final system is shown in Figure 3-20.

Figure 3-19: Final render of the CAD model of the MPµSL system.

3.3.System Control

There are multiple components of the system described above that require computer based direction. This primarily includes linear motor (stage) position and image projected from the DMD. It is critical that the software precisely controls not only the position of the stage and the duration of a unique image projection, but also the timing between the two.

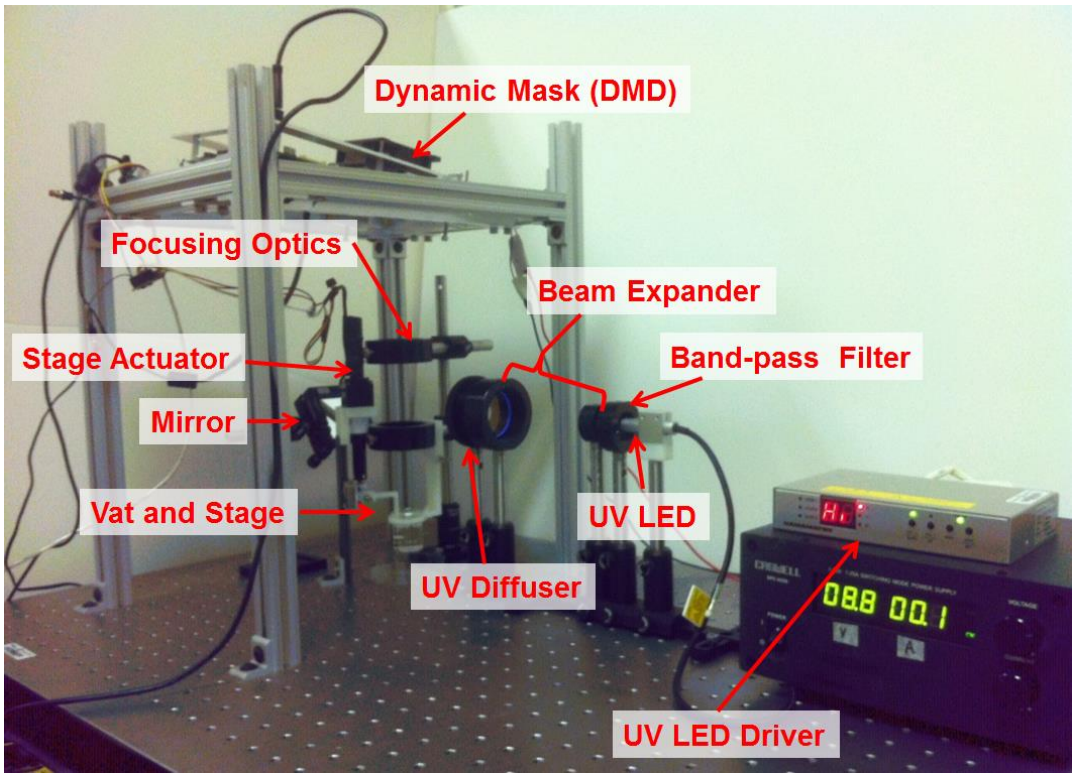

Figure 3-20: Image of the complete mask projection microstereolithography system with major components labeled.

3.3.1. Hardware Interfacing and Control

The Flexlight X1 kit interfaces with the computer via mini HDMI port. By setting up the DMD as a secondary computer monitor, images can be sent to the chip via the HDMI cable with a frame rate more than suitable for projection curing.

The linear actuator communicates with the computer via the EZ10EN EZstepper motor controller (Figure 3-21). The motor controller connects to a PC via a USB to RS485 converter (Figure 3-22). This converter combines the power wires and the serial communication data for the controller/motor from a standard USB connector and sends it to a four pin connector that has the same pinout as the EZStepper 4 wire bus.

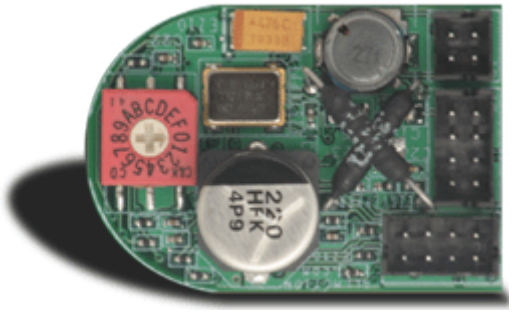

Figure 3-21: Image of the EZ10EN stepper motor controller (www.allmotion.com, used under fair use, 2014).

Figure 3-22: Image of USB to RS485 converter (www.allmotion.com, used under fair use, 2014).

3.3.2. Software Design

The software that controls the system was developed in LabVIEW and follows typical state machine (event driven) architecture. A state machine consists of a set of states and a case selector that determines when the program transitions from one state to the next. The state machine waits for an event to occur before transitioning to the next state, which can either a user controlled event or an in-state calculation [46]. In this case, the program is begun via user input, and then proceeds autonomously until the print has finished. The states within this system are detailed below.

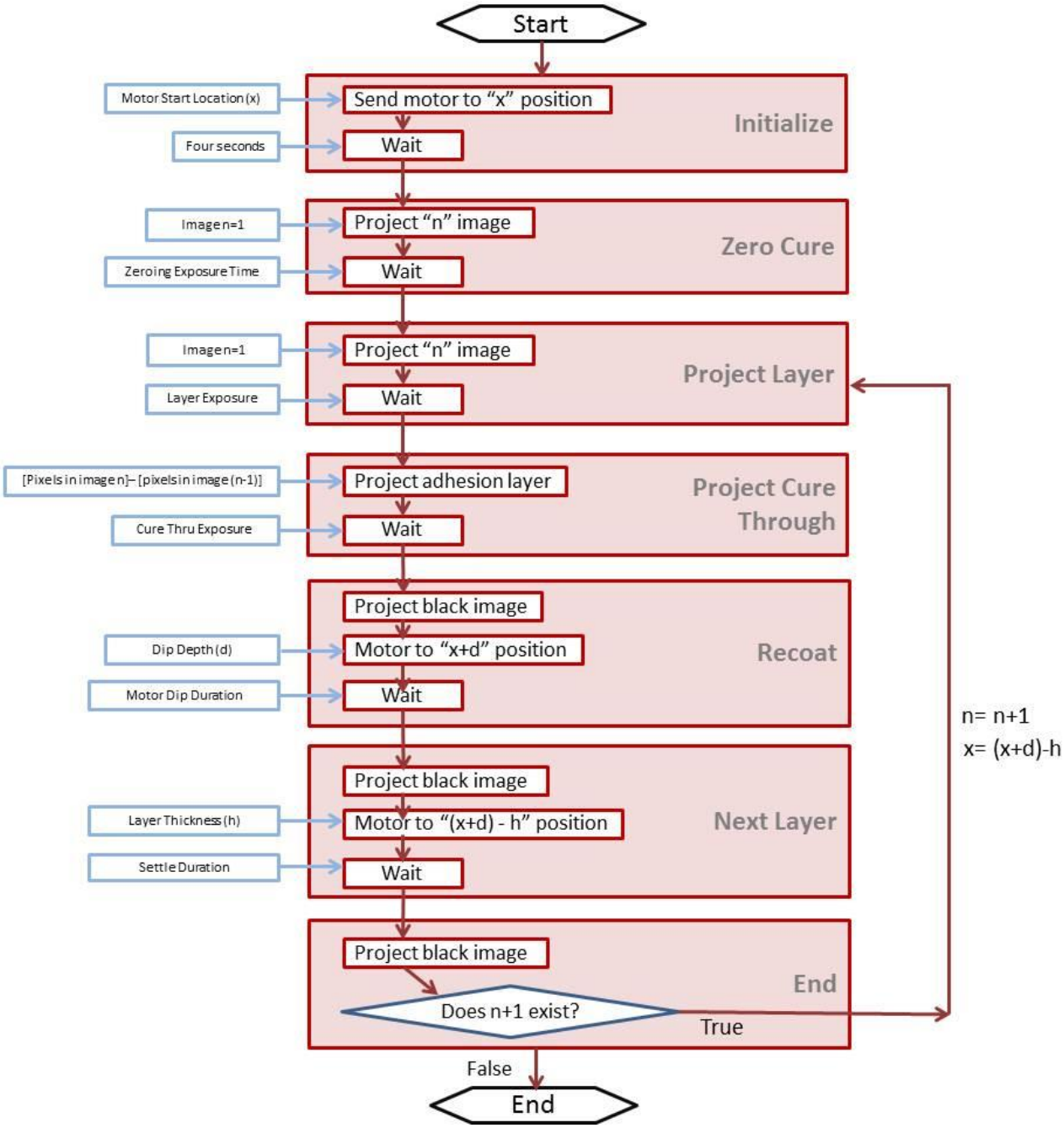

Figure 3-23: A flowchart of the software that controls the MPµSL system.

3.3.2.1. Initialize

This is the preliminary state in the controls software. The main purpose of this state is to set the initial motor location, orienting the build platform into the focal plane of the projection, just under the surface of the resin.

3.3.2.2. Zero Cure

This state follows immediately after the “initialize” state, and serves to level the build surface by over exposing the resin directly over the build platform. This insures that, regardless of user input, the first layer of the part being printed is exactly level and exactly aligned with the resin surface.

3.3.2.3. Project Layer

The program then enters into the first of five states that compose of the loop that builds the designated part. “Project layer” shows the image of the called upon file, which in the first time through the loop is the first image of the sliced part. The image is projected for the user designated time, and then transitions to the next state.

3.3.2.4. Project Cure Through

This state is a unique option in this software that gives the user the ability to control the adhesion between the current layer and the previous layer. The design of this state derived inspiration from work by Limaye and Rosen based on a process called the “compensation zone approach” [27]. The purpose of this state is to increase the dimensional accuracy of downward facing surfaces, and reduce unintended cure through. This state conducts an image subtraction process that identifies the shared locations of exposure between the current layer and the previous layer images, and creates a new image that contains only these locations. When this state is active, the “Project Layer” state provides only enough energy to create the layer with the desired thickness, while “Project Cure Through” uses the newly generated image to adhere the current layer to the previous layer. This process ensures that cure through, which is needed for layer adhesion, only occurs where cured material exists in the previous layer, and works to prevent unwanted curing. Once this state has completed its instructions, it triggers the transition to the next state.

3.3.2.5. Recoat

At this point, the layer has been built, and the program then enters the state that applies a fresh layer of resin to the top surface of the part. This is done via the “deep dip” process. The

state sends word to the linear actuator to move to a depth in the resin vat based on predetermined user input.

3.3.2.6. Next Layer

The program then conducts a calculation to determine where to send the linear actuator to build the next layer. This calculation, based on dip depth and layer thickness, sets the motor location to such that the part being built is precisely one layer thickness below the resin surface. Once the motor has finished moving, the system transitions to the final state in the loop.

3.3.2.7. End?

The last state of the five state loop exists to simply determine whether the last image of the part has been projected. If that is not the case, the system then transitions back to the "Project Layer" state, and references the next image in the part. If the last image has been called, the program ends and sends a signal to the linear actuator to return to the initial position, removing the final part from the resin vat.

3.3.3. User Interface

The control panel that the system user operates contains fields in which specifications of the print can be entered. The LaBVIEW front panel user interface is shown in Figure 3-24.

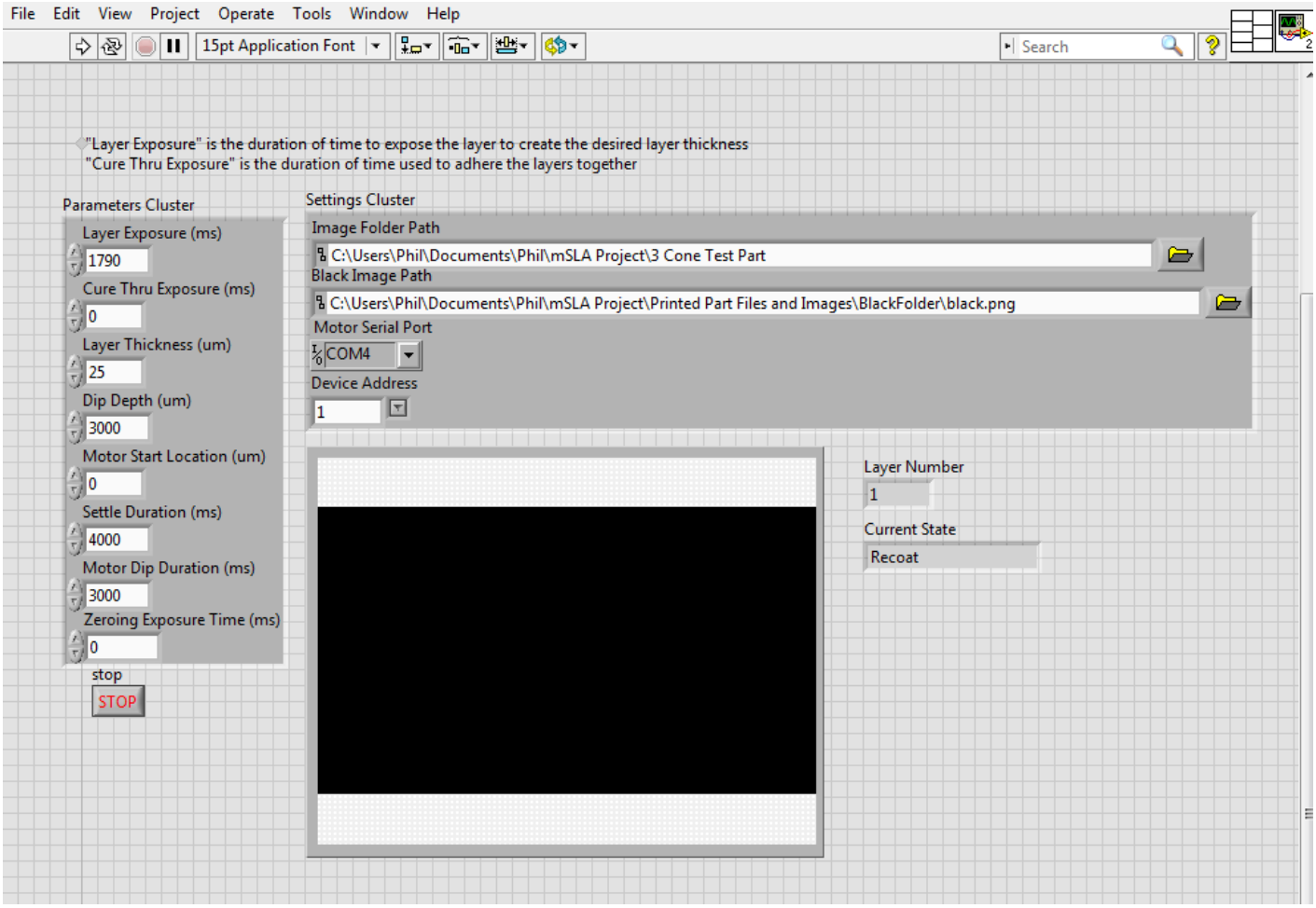

Figure 3-24: LabVIEW front panel user interface for the system software.

Each field in the UI is described below. The next section explains the function of each of the fields.

3.3.3.1. Parameters Cluster

- *Layer Exposure*: This designates the time, in milliseconds, the user wants to expose each layer to UV light.
- *Cure Thu Exposure:* This designates the time, in milliseconds, the user wants to expose an adhesion image (this is currently an unused feature of the software).
- *Layer Thickness:* This field allows the user to choose a layer thickness in microns. This should match the layer thickness chosen in the slicing of the part.

- *Dip Depth:* This gives the user the option to choose the dip depth (in microns). The user may want to select greater dip depths for more viscous resins.
- *Motor Start Location:* This field allows the user to select the starting position of the motor, also in microns. This position should be chosen based on the level of the resin and the dimensions of the build stage.
- *Settle Duration:* The user can select a time, in milliseconds, to allow the resin to settle prior to beginning the next layer (after returning from the recoat deep dip).
- *Motor Dip Duration:* The motor takes a specific amount of time to conclude its movement during the dip process, but this is not information that the motor feeds back to the software. Therefore, the user must input a time (milliseconds) to allow the motor to complete this process; else the transition to the next state will occur prematurely.
- *Zeroing Exposure Time:* In this field, the user can designate an exposure time of the first image (independent of the "project layer" state) for leveling purposes described earlier.

3.3.3.2. Settings Cluster

- *Image Folder Path*: The user must select a folder path, located locally, that contains a series of 1920x1080 images (with increasing reference numbers) organized in ascending order. This is the folder that the software checks for the projection images.
- *Black Image Path:* The user must select an image path, located locally, that contains a 1920x1080 entirely black image. This is the image that is projected while motor motion and resin settling occurs.
- *Motor Serial Port:* The user must select the correct port number that the linear actuator is plugged into.
- *Device Address:* The user must leave this defaulted at 1.

3.3.3.3. Indicators

The following fields on the control panel contain data transmitted from the program as indicators of build progress.

- *Unlabeled image*: This is a representation of the current image being projected.

- *Layer Number:* This is the number of the current layer being projected.
- *Current State:* This is the name of the state that the program is currently running.

3.4.Finalization

After the system was assembled and the software written and implemented, significant fine tuning was conducted to achieve repeatable functionality. This included diligent alignment of all optics and mounts to match calculations, as well as determining the precise location of the build plane. As mentioned earlier, any vertical variation from the focal point of the projection greatly impacts minimum feature size and UV light intensity. For repeatability, it is essential to have the build plane constant from print to print.

With the process developed and the system aligned, the next step was to develop a process to characterize the polymers that will be used to fabricate 3D structures with this MPμSL system.

4. Methods for Characterizing Novel Polymers (CQ1)

The performance of an MPμSL system is dependent upon the limitations inherent in system design as well as the curing characteristics of the photopolymer resin used to fabricate parts. Characterization Question 1 asks: ***"H**ow can the curing characteristics and performance of a photopolymer in the MPμSL system be determined?"* This chapter presents the overall research methods employed to answer this question, and thus to understand the performance of the system. Specifically, the research methods described here are used to determine the curing characteristics of a photopolymer and to identify the manufacturing limitations of that polymer on the designed system.

4.1. Photopolymer

The general ingredients for a photopolymer include the base material (a polymer, oligomer or monomer), photoinitiator, and could also include photoinhibitors and surfactants. The polymer/oligomer/monomer is the functionalized base molecule, meaning it has reactive groups located at the end of the molecule. The photoinitiator is the component that initializes the polymerization reaction. When irradiated, the initiator produces free radicals (for acrylates) or cations (for epoxies) that induce polymerization. The liquid monomer polymerizes by a chain reaction, cross linking the polymer chains and forming a solid polymer. A photoinhibitor is a light absorber, and is used sparingly to tune the reactivity of the photopolymer to irradiation [47], [48].

4.2. Working Curve

In 1992, Paul Jacobs presented a method for identifying the photosensitivity of UV curable resin during the stereolithography process. The expression is based on the Beer-Lambert law of absorption, and is written as [49]:

$$C_d = D_p \ln(E/E_C) \qquad \textbf{Equation 4-1}$$

The term C_d represents the cured depth, or the thickness of gelled resin. E is the UV exposure provided to the resin at the curing wavelength. The critical exposure, E_c, is the UV energy

required to initiate polymer curing. D_p is the depth of penetration of UV light into the resin. The expression presented in Equation 6 is used to generate the fundamental "Working Curve." The Working Curve is a semi-logarithmic plot of cure depth vs. the natural log of exposure, an example of which is presented in Figure 4-1.

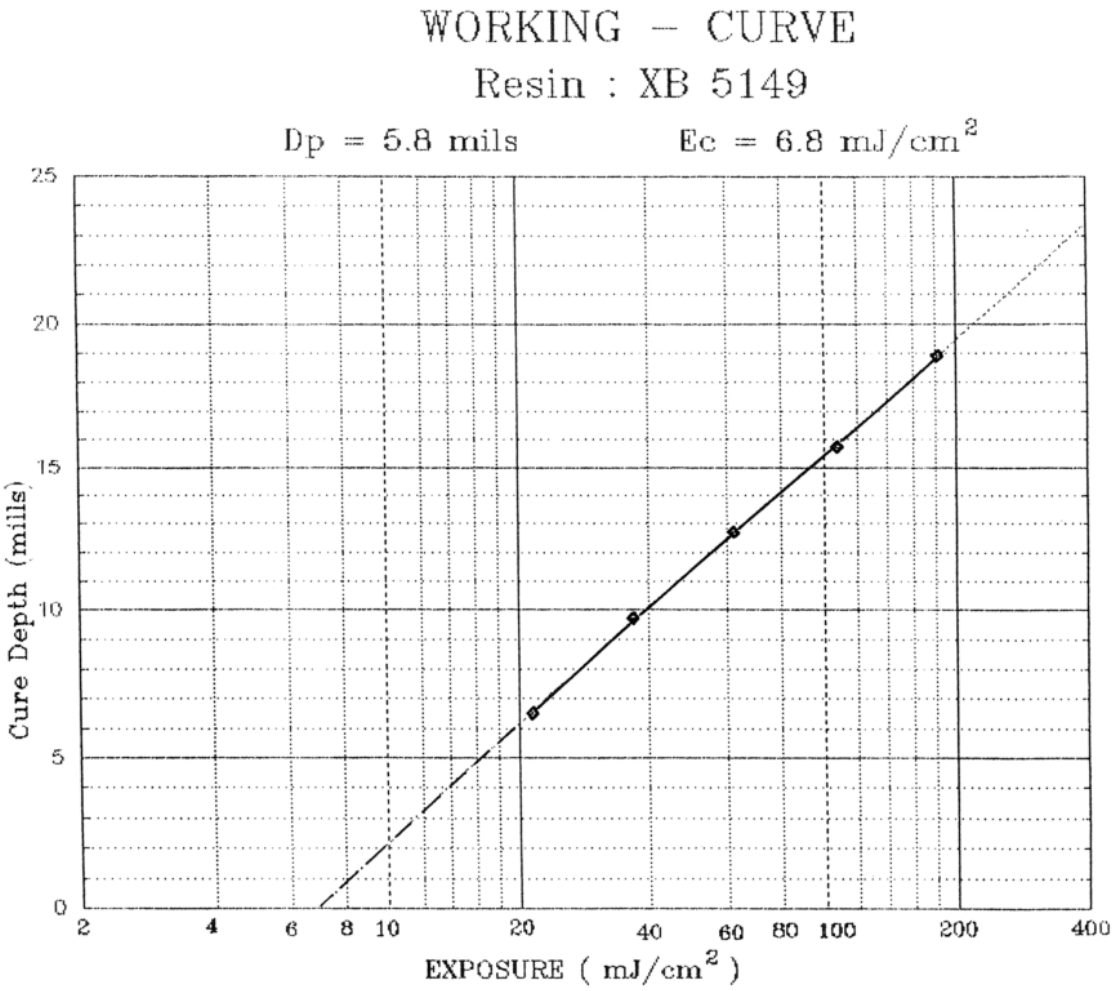

Figure 4-1: A Working Curve, developed by Jacobs, for Ciga-Geity resin XB 5149, where the D_p is 5.8 mils, and the E_c is 6.8 mJ/cm^2 (P. Jacobs, "Fundamentals of stereolithography," *Proc. Solid Free. Fabr.,* July, 1992., Used under fair use, 2014).

The working curve shows several important fundamentals to understanding stereolithography. The first of which is that the semi-logarithmic plot should result in a linear relationship between cure depth and the natural log of exposure. The slope of this straight line relationship is

equivalent to the penetration depth, D_p, of the resin. The value where cure depth is equal to zero, the x-intercept, is the *E* value where polymerization begins, known as critical exposure, E_c. Depth of penetration and critical exposure are both purely resin characteristics, which means that they should stand independent of UV intensity.

4.3. Characterization Method

Prior to printing with any resin, the primary step is identifying the curing characteristics of the resin by generating a working curve. Once the curve has been developed, the relationship between exposure energy and cure depth is known and proper print parameters can be chosen. A method was employed to accurately determine the working curve for new resins introduced into the MPμSL system.

4.3.1. Generating a Working Curve

The following steps outline the method that was used to generate a working curve for photopolymers used with this MPμSL system.

Step 1: Mix the photopolymer.

The photo-initiator used in this body of research was DMPA (2, 2-dimethoxy-1, 2-diphenylethan-1-one). In all experiments, 2 wt% of the DMPA initiator was dissolved in acetone and mixed into the polymer resin.

Step 2: Prime light source, measure light intensity.

After the UV light source has been powered on, there is warm up period before the UV light intensity becomes stable (approximately 2 hours). Once the light source is primed, the UV light intensity was measured. This was accomplished by shining a white image across the entire projection area and measuring the UV intensity (mW/cm^2) at the build plane with a UV radiometer.

Step 3: Fill vat.

In the third step, the light source was blocked (not turned off), and the vat was aligned beneath the projection area. The vat was filled with photopolymer precisely to the location of the build plane (the focal length of the final focusing lens, 75mm).

Step 4: Generate test samples.

To develop a working curve, the cure depth of the resin is measured according to the precise exposure provided. With the UV light intensity known, the exposure was varied by adjusting the exposure time. The samples were fabricated by exposing the resin vat to the entire projection area of the MPµSL system for a set period of time. Four test samples were generated at four different time steps (corresponding to different exposures), which vary according to each resin's UV sensitivity. The samples were gently retrieved from the resin with tweezers.

Step 5: Dry and measure samples.

The 12 samples were washed gently with IPA and left to dry. Using a micrometer, the thickness of each sample was measured and recorded. Due to the fragile nature of the thin film samples, extra care was taken not to fracture the samples with the micrometer before an accurate measurement is recorded.

The recorded data from the experiment was then inputted into a MATLAB program that averages the four sample measurements for each exposure time and plots the average cure depth C_d versus the exposure (in mJ/cm^2). The program generates a working curve and calculates the critical exposure and depth of penetration based on the data using Equation 6. The working curve for the resin is then used to calculate the exposure necessary to cure a certain layer depth. As mentioned earlier, the slope of the curve is equal to the depth of penetration of light into the resin (Figure 4-1). As this value grows, the greater affect a small change in exposure will have on cure depth. Photocurable resins with a high depth of penetration are very sensitive to changes in exposure energy, making fine control over cure depth a great challenge.

4.3.2. Performance Characterization

The next important step in determining the performance of a polymer in the MPμSL system is to identify the XY plane minimum feature size, the lateral (XY plane) accuracy, the Z-axis minimum feature size, and the Z-axis (XZ and YZ planes) accuracy. A benchmark part was designed with SolidWorks to quantify these parameters.

The benchmark part was designed such that the XY minimum feature size, the XY accuracy, the Z minimum feature size and the Z accuracy could be measured and quantified. The part was designed to be sliced and printed with 25 micron layers. A drawing of the part can be seen below in Figure 4-2.

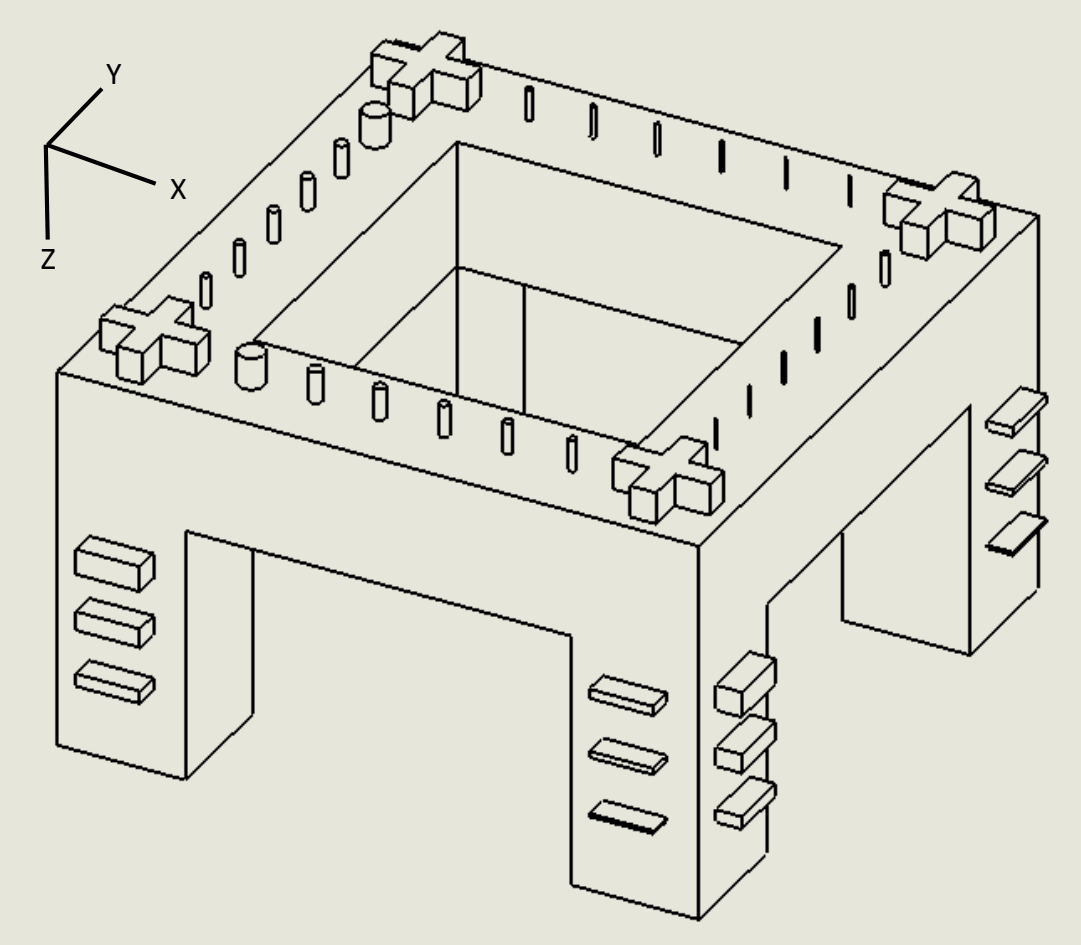

Figure 4-2: Isometric image of the benchmark characterization part.

There are four critical sets of features on the part, and each set is designed to quantify a different performance metric.

- The first feature on this part is the cross beam on the four lateral faces. Measuring the thickness of the cross beams contributes to the Z-dimension accuracy (Figure 4-3).
- The second set of features is the extrusions on the XZ and YZ faces. These extrusions are reduced incrementally in Z height thickness, from 200 microns to 25 microns. Measuring the thickness of the smallest structure, the Z accuracy (along with the cross beams) and minimum Z axis feature size can be determined (Figure 4-3).
- The cylindrical extrusions on the top plane of the part incrementally reduce in diameter from 200 microns to 5 microns (dimensions in Figure 4-4), along both the X and Y axes. These cylinders are used to measure the minimum printable feature size in the XY plane.
- The cross-shaped extrusions on the top plane of the part. They all have the same dimensions and are located equidistant from one another. By measuring the relative distances of the cross-features, the accuracy of the XY plane can be determined.

The dimensions of the benchmark part are presented in Figure 4-3 and Figure 4-4.

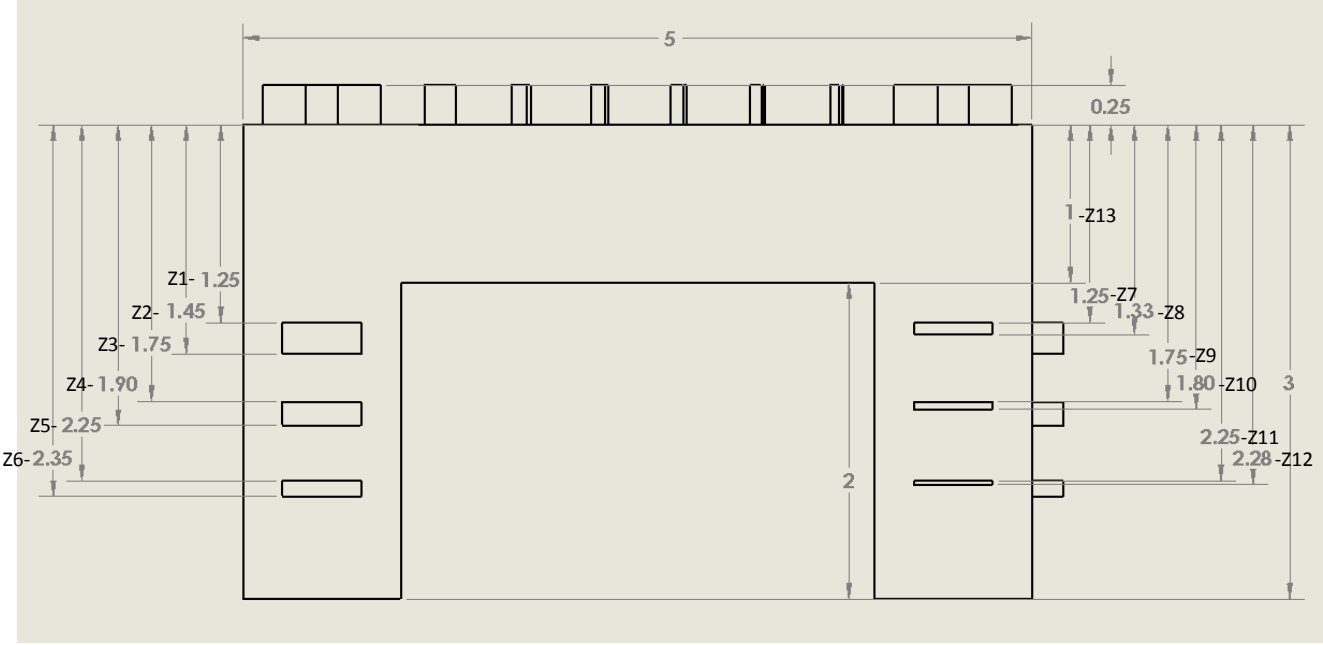

Figure 4-3: A lateral view of the benchmark test part with dimensions in millimeters.

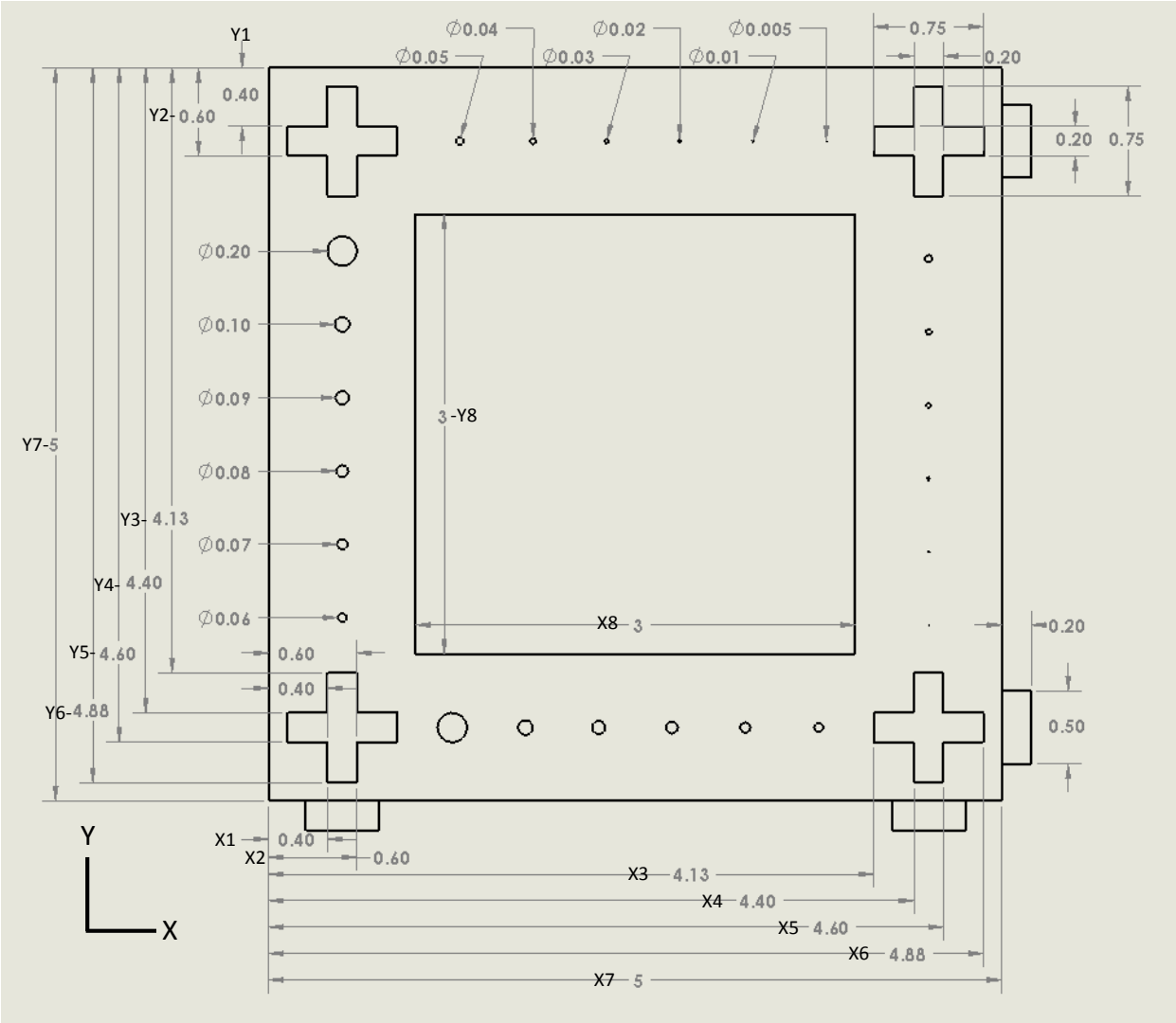

Figure 4-4: Top down view of the benchmark test part with dimensions in millimeters.

4.3.2.1. Step-By-Step Process

With curing characteristics of the photopolymer known from the generation of the working curve, the following step by step method was used for determining the polymer performance on the designed MPµSL system.

Step 1: Slice the test part.

The file was exported from SolidWorks as a .STL file and imported into NetFabb. In NetFabb, the part was sliced at 25 micrometer increments (i.e., the layer thickness), and the slices were exported as PNG files into a folder.

Step 2: Load the folder, and prepare the printing software.

In the user interface of the MPµSL software, direct the "Image Folder Path" field to the folder that was generated containing the sliced images. Use the working curve to determine the exposure necessary for 25 micrometer cure depth, and input that number into the "Layer Exposure" field. The remaining fields should read as follows in Figure 4-5:

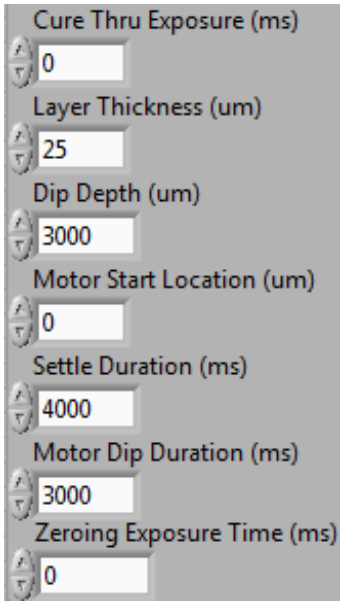

Figure 4-5: The settings required for the benchmark characterization part.

Step 3: Fill vat and insert stage.

In the third step, the vat was filled with the photopolymer and the stage was inserted into the stage adapter. Care was taken to be sure that the image projection was entirely on the stage. The stage build area should sit exactly level with the build plane, slightly below the photopolymer surface.

Step 4: Generate test samples.

The LabVIEW VI was started, and the print began. The once the print has finished, the stage was gently removed from the stage adapter and replaced with a new stage. The print was repeated twice more.

Step 5: Prepare the parts.

The printed parts were allowed to drip dry for a few minutes to allow the uncured resin to be recollected. IPA was then used to gently rinse the part of any remaining uncured photopolymer. The parts were allowed to dry for an hour.

Step 6: Measure the parts.

In the final step, parts were measured using a DinoLight digital microscope. The measurements taken were the diameter of the smallest printed cylinder, the X dimensions and Y dimensions labeled in Figure 4-4, and the Z dimensions labeled in Figure 4-3, and the thickness of the cross beams at their center.

With the smallest cylinder measured, the minimum printable feature in the XY plane for this polymer was determined. With the thickness of the XZ and YZ extrusions measured, the minimum feature size in these planes was determined as well. The measurements of the Z-axis cross beams and the distance between the XY plane cross-shapes were then compared to the designed measurements to determine the accuracy of these features.

4.4. Application

The methods outlined in this chapter are used to classify the performance of a resin in this Mask Projection Microstereolithography system. The work presented in Chapter 5 utilized this method to characterize the performance of the designed system with a baseline resin. Section 6.2 utilized these methods to determine the effect of Tinuvin 400 on cure depth and depth of penetration in the baseline resin. Finally, in Chapter 7, two novel photopolymers are introduced, characterized, and their performance with the system determined using the aforementioned characterization methods.

5. Benchmarking the MPμSL System

In this chapter, the performance of the system is characterized and compared to systems of similar embodiment within the context of Characterization Question 2 (CQ2): "*How does the performance of the system designed as part of this work compare to other systems of similar morphology?"* The four system performance parameters are (i) minimum feature size, (ii) minimum layer thickness, (iii) maximum part size, and (iv) vertical build rate. Furthermore, the accuracy of the system is determined by answering Characterization Question 3 (CQ3) "*How well does the printed part dimensionally compare to the designed model?"*

5.1. System Characterization

To benchmark the system, the polymer poly (propylene glycol) diacrylate (PPGDA) was chosen as the standard. A detailed explanation of the polymer is presented below, followed by the characterization of the polymer and its performance with the MPμSL system.

5.1.1. Poly (Propylene Glycol) Diacrylate

Poly (Propylene Glycol) Diacrylate is a polyfunctional acrylic monomer that was acquired from Sigma Aldrich (CAS 52496-08-9). The PPGDA has an average M_n of 800, and contains 100ppm of BHT (butylated hydroxytoluene) as inhibitor, and 100 ppm MEHQ (mono methyl ether of hydroquinone) as inhibitor. Figure 5-1 shows the chemical structure of the monomer.

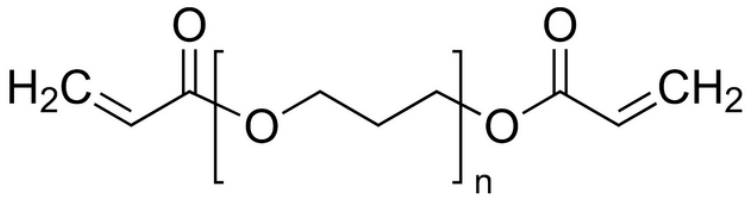

Figure 5-1: Chemical structure of poly (propylene glycol) diacrylate.

5.1.2. Preparation and Characterization

The prepolymer consisted of 2 wt% photo-initiator DMPA (2, 2-dimethoxy-1, 2-diphenylethan-1-one) dissolved into 50 mL of PPGDA. Following the process outlined in Chapter 4, a working curve was developed for the PPGDA photopolymer. The intensity at the build plane (resin

surface) was 4.9 mW/cm^2. The thickness of the fabricated four samples per tested exposure dosage were measured using a micrometer, and are listed below in Table 5-1.

Table 5-1: Cure depth thicknesses for increasing exposure energy for PPGDA with 2wt% initiator.

Exposure (mJ/cm2)	**9.8**	**12.25**	**14.7**	**17.15**
Sample 1 (μm)	185	284	345	425
Sample 2 (μm)	196	286	338	427
Sample 3 (μm)	203	284	340	413
Sample 4 (μm)	185	290	345	421
Average	192.25	286	342	421.5
Std. Dev.	8.8	2.8	3.6	6.2

The data was entered into the MATLAB software, and a working curve (Figure 5-2) was generated and the critical exposure and depth of penetration were calculated. The critical exposure E_c is 6.05 mJ/cm^2, and the depth of penetration D_p is 398 micrometers.

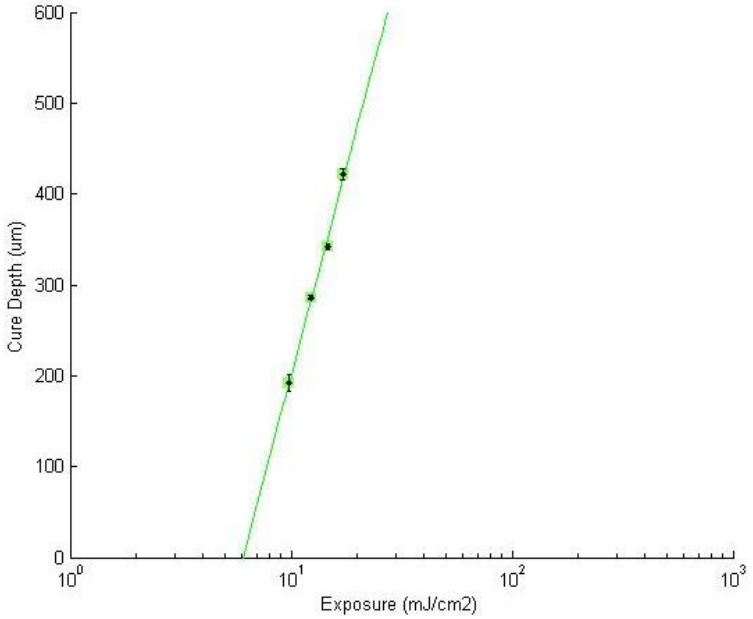

Figure 5-2: The working curve for PPGDA with 2wt% DMPA initiator.

5.1.3. Minimum Feature Size

The minimum feature size of this system is difficult to characterize, as the minimum feature size was determined to be reliant on the shape being manufactured. Two experiments were

conducted to analyze the minimum feature size the system can fabricate. The first experiment utilizes the benchmark part presented in Figure 4-2, which was designed with cylinders of decreasing diameter on the top XY face to determine minimum printable feature size. The cylinders decreased equivalently in size on both the X and Y axes of the part, so as to identify any differences in feature size between the axes.

The benchmark test part was printed three separate times with an exposure time of 1.19 seconds. This is the time necessary to provide exposure energy of 6.44 mJ/cm^2 - the exposure required for 25 micron cure depth according to the working curve in Figure 5-2. The smallest printed cylinders are presented in Table 5-2.

Table 5-2: The measured diameter (mm) of the smallest cylinders printed on the sample benchmark parts (Figure 4-2).

	Part 1	Part 2	Part 3	Average	Std. Dev.	Error
X	0.218	0.206	0.204	0.209	0.006	5%
Y	0.21	0.218	0.216	0.215	0.003	7%
			Overall	0.212	0.006	6%

"X" refers to the smallest feature measured on the X axis of the first sample benchmark part, and "Y" refers to the smallest feature measured on the Y axis of the first sample benchmark part. The smallest diameter cylinder printed on all samples was the cylinder deigned with a diameter of 200 micrometers (0.2mm) – the cylinders designed smaller than 200 micrometers did not print successfully. The measured diameter varied slightly compared to the designed size, and the average diameter of the measured cylinders was 212 micrometers (6% error) with a standard deviation of 6 micrometers.

The second experiment used a test part that was specifically designed to identify the smallest feature that was able to cured by the machine. The part was designed as series of three cones aligned along one axis. Each cone is 6 mm tall, with a base diameter of 2mm and a tip diameter of 0.002mm (2 microns). A 3D drawing and dimensions of the model are shown in Figure 5-3.

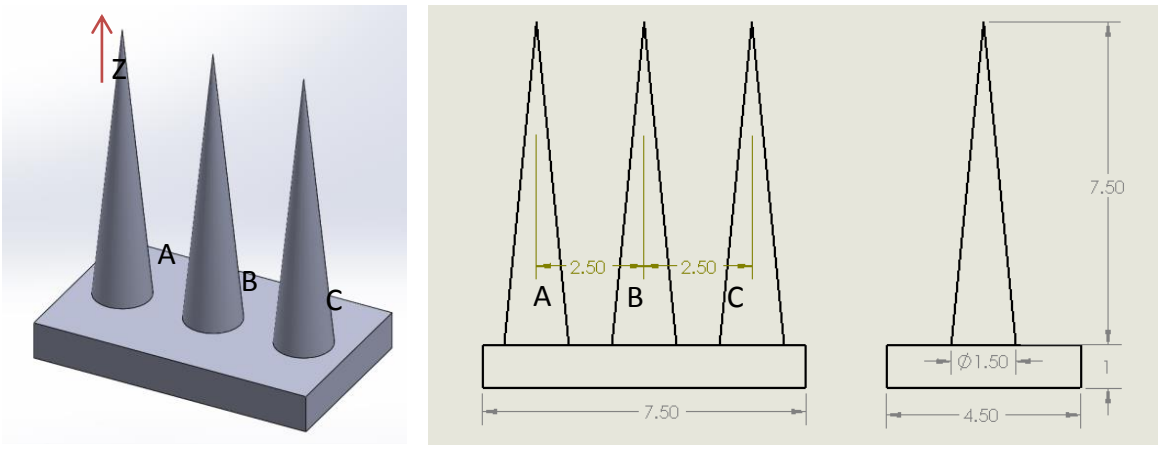

Figure 5-3: (Left) 3D model of the 3 cone test part. (Right) Dimensions of the test part.

This part design was chosen due to the decreasing feature size of the cone geometry. When sliced, each consecutive layer is a projection of a solid circle slightly smaller than the previous image. As the images progress through the print process, the system will eventually reach an image that no longer cures or adheres to the previous layer. The final layer that polymerizes will be the tip of the cone, and represents the threshold limit for feature size of the cone. The cone geometry was designed such that when sliced for 25 micron layers, each projected circle changes in diameter by 5 microns, with the final circular image having a diameter of 5 micrometers. Each cone was labeled with an A, B, or C for ease of reference, with the difference between the cones limited only to its location in the XY projection plane.

The material used for this experiment was the same used in the previous experiment: 2wt% DMPA photo-initiator dissolved within functionalized Polypropylene Glycol Diacrylate (PPGDA). For this experiment, UV intensity at the build plane was measured to be 5.4 mW/cm^2. From the working in Figure 5-2, with an intensity of 5.4 mW/ cm^2, the required exposure time per layer is 1.02 seconds. Three sample parts were generated. The diameter of the tip of each cone was measured with a DinoLite Pro digital microscope. The data from the experiment is shown below in Table 5-3.

Table 5-3: Data from feature size experiment with measurements in micrometers.

	Cone A	Cone B	Cone C
Part 1 (μm)	49	38	51
Part 2 (μm)	61	38	59
Part 3 (μm)	55	40	47
Average	55	39	52
Std. Dev	4.9	0.9	5.0
Total Average	48.7		
Total Std. Dev.	8.2		

When making the measurements for the cone tips, the DinoLite Pro microscope was at full magnification (225x). At this magnification, each pixel on the image was representative of ~2 microns. Therefore, the resolution limit of the measurements was 2 micrometers. The difference from one pixel to another is almost indistinguishable; making the measurement error for each data point is at least ±2 micrometers (0.002 mm), if not more. Figure 5-4 shows the tip of the smallest measured cone for the entire experiment.

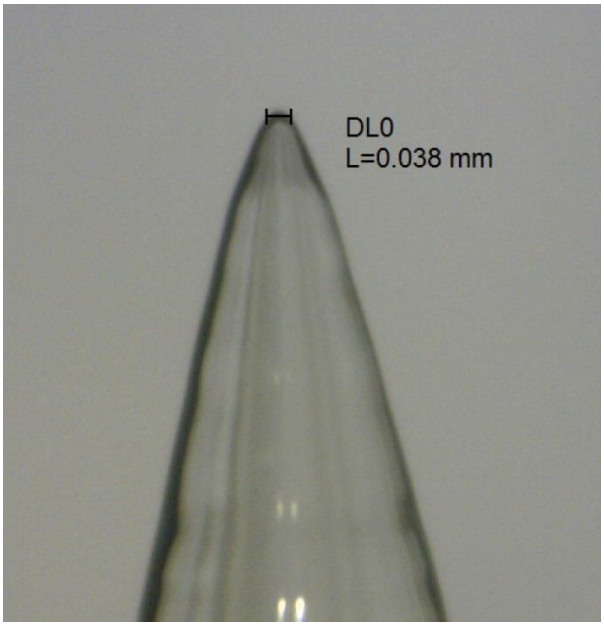

Figure 5-4: Image of a printed cone shape with a tip diameter of 38 micrometers.

The cone structures were imaged using Scanning Electron Microscopy (SEM), as shown in Figure 5-5.

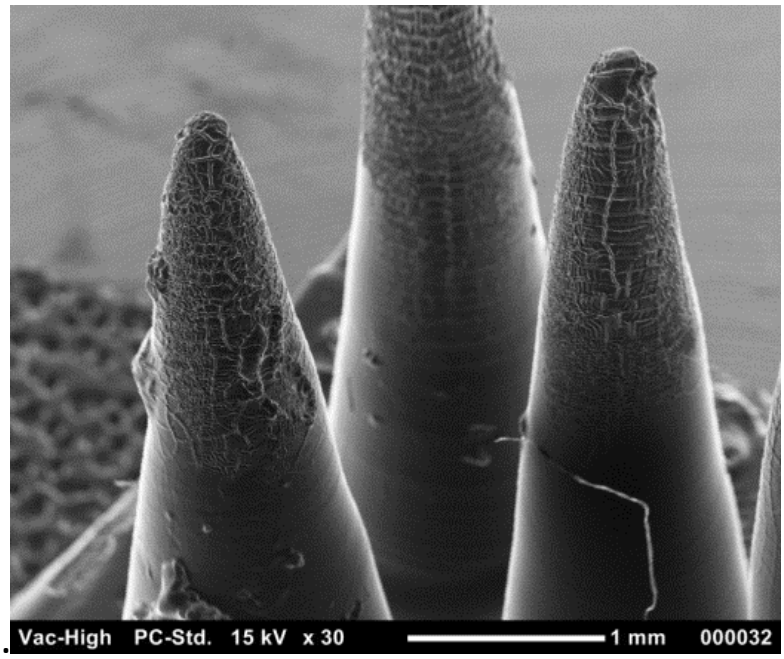

Figure 5-5: SEM image of the cone structures.

The tip of the cone in Figure 5-4 comes to a point of 38 micrometers, and the measurement is only 15 pixels wide (the image here is blown up significantly). The limitations of the microscope and corresponding software make this measurement difficult to confirm with efficacy. Considering the scale of the measurements and the resolution of the measurement tool, the absolute measurements may be inaccurate by a non-trivial amount. However, all measurements were made with as much attention to detail as is possible, and conducted in the same manner throughout all measurements.

To compare the results of the two experiments, refer to the Table 5-4 below.

Table 5-4: Comparison between the minimum achievable feature sizes of the benchmark part and the three cone part.

	Average (μm)	Std. Dev.
Benchmark	212	5.7
Three Cones	48.7	8.2

The second experiment exhibited minimum achievable features sizes as small as 38 micrometers, whereas with the first experiment the smallest feature was 204 micrometers in diameter. This means that feature size is very likely dependent on geometry. However, the critical issue with the cone design for measuring the minimum feature size is that it was impossible to determine what layer was the final layer to cure. This means that it was impossible to determine what the designed diameter of the final exposed image to cure was.

While the second experiment revealed that the system can achieve smaller features than the benchmark part suggests, the features do not demonstrate a relationship between designed feature size and achieved feature size. The system's minimum feature size with PPGDA is reported as 212 micrometers, per the result of experiment conducted with the benchmark part.

5.1.4. Minimum Layer Thickness

A photopolymer may be capable of curing at very small depths without breaking, creating very thin structures. However, on this MPµSL system, the stepper motor being used to move to the build platform from one layer to the next has positioning resolution limits. An experiment was derived to determine the minimum layer thickness that the system's stepper motor can repeatedly achieve.

Using the DinoLight Pro digital microscope at 225x magnification, the stepper motor was commanded to move to absolute positions exactly equivalent to the commands that the software would deliver during a print process. For example, when testing for a 20 micron layer thickness, the following command sequence would be followed (sent to the stepper motor via USB using software called "EZCommander"):

- **Origin:** Command 0
- Dip: Command 2000 (motor moves to 2000 micrometers from the origin)
- **L1:** Command 20 (motor moves to 20 micrometers from the origin)
- Dip: Command 2020 (motor moves to 2020 micrometers from the origin)
- **L2:** Command 40 (motor moves to 40 micrometers from the origin)
- Dip: Command 2040 (motor moves to 2040 micrometers from the origin)

- **L3:** Command 60 (motor moves to 60 micrometers from the origin)
- Dip: Command 2060 (motor moves to 2060 micrometers from the origin
- **L4:** Command 80 (motor moves to 80 micrometers from the origin)
- Dip: Command 2080 (motor moves to 2080 micrometers from the origin
- **L5:** Command 100 (motor moves to 100 micrometers from the origin)

This command sequence mimics the deep dipping process used in the print process, as exhibited by the "Dip" 2000 micrometer movement between each simulated layer. The L1-L5 commands represent the first five layers of a simulated print.

The initial simulated layer thickness was 10 micrometers, which was increased in increments of 5 micrometers until a reliable and repeatable layer thickness was discovered. The experiment observed the motor locations with a 10 micrometer simulated layer thickness (henceforth referred to as intervals), 15 micrometer intervals, 20 micrometer intervals, and 25 micrometer intervals. The image in Figure 5-6 is a screenshot from the DinoLight Pro software, where each yellow line represents the location of the motor at a specific motor command. The left most line of each cluster of lines represents the origin, and 5 sequential data points were collected for each interval distance.

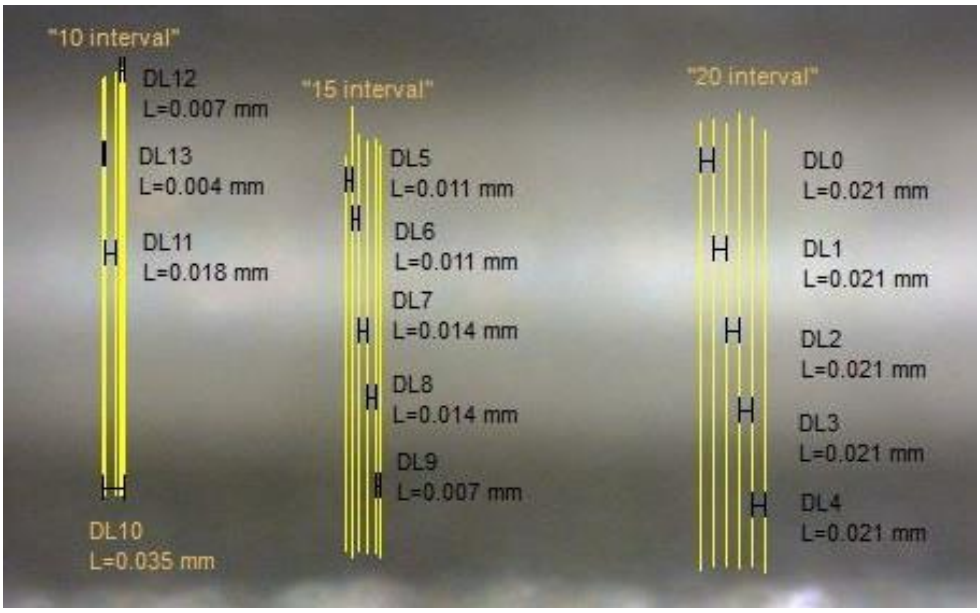

Figure 5-6: Measurements of the motor location with 10, 15 and 20 interval commands.

The 10 micrometer interval commands resulted in almost no perceivable motor movements, and a complete set of data could not be collected. The 15 micrometer interval was measurable, but by no means accurate with a range of distances from 7 micrometers to 14 micrometers. At 20 micrometer intervals, the motor started to demonstrate observable accuracy and repeatability. The 20 micrometer interval was repeated twice more to confirm the results.

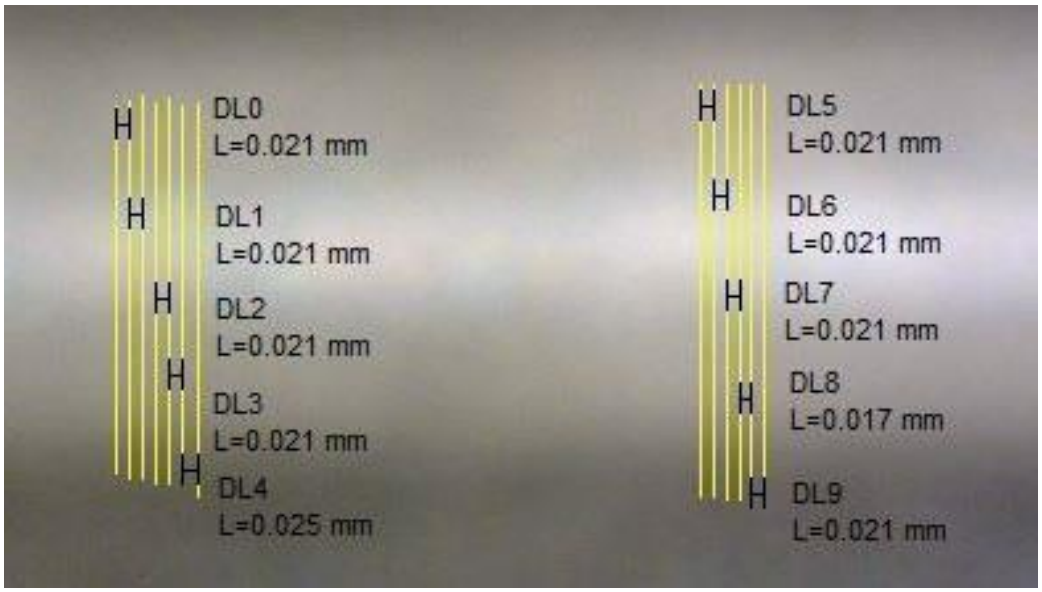

Figure 5-7: Confirmation data sets showing the measurements of the motor location with 20 interval command.

Overall, three sets of data were collected for the 20 micrometer interval, with 5 motor location commands (denoted as L1-L5 in Table 5-5) for each data set. A total of 15 motor locations were collected, and are presented in Table 5-5 below.

Table 5-5: Measurements for the 20 micrometer interval motor resolution test.

	L 1	**L 2**	**L 3**	**L 4**	**L 5**
Set 1 (µm)	21	21	21	21	21
Set 2 (µm)	21	21	21	21	25
Set 3 (µm)	21	21	21	17	21
Average	21	21	21	19.7	22.3
Std. Dev	0	0	0	1.9	1.9
Total Average	21				
Total Std. Dev	1.5				

The DinoLight Pro microscope and corresponding software at full 225x magnification has a measurement resolution of 2 microns. When measuring an object, each pixel on the screen represents a 2 micrometer change in distance. This means that each data point has an associated error of at least ±1, providing there are no other sources of error.

The median of this data set is 21 micrometers which falls within the expected ±1 micrometer error range from the 20 micrometer command. Furthermore, the data reveals that out of the 15 sample points collected, there were only two outliers. This suggests that at a 20 micrometer distance interval, the motor has 87% repeatability with zero margin for error, and 100% repeatability with a 4 micrometer margin for error. This falls within acceptable limits for the scope of this system, which means the minimum layer thickness that the motor can reasonably achieve is 20 ±1 micrometers.

5.1.5. Maximum Part Size

The maximum part size is a performance parameter that is not truly restricted to the 6mm x 8 mm x 36 mm volume as is currently listed. The projection area, approximately 6 mm x 8mm will not change, but the height of the part is listed as 36 mm due to the current geometry of the vat choice and stage design. By substituting the 20mL glass beaker with a deeper vat, and redesigning the stage to have a longer Z-dimension, the height of a printed part could be increased to the entire length of the motor travel distance, 60mm.

5.1.6. Vertical Build Rate

The final performance parameter is the vertical build rate. This parameter is highly dependent on resin properties such as critical exposure and viscosity. With higher critical exposure, a resin takes longer to reach the gel point, and extends the time per layer. Similarly, the viscosity of the resin contributes to the refresh duration required after the dipping recoat process. Higher viscosity resins take longer to settle, extending the time per layer, and thus the vertical build rate. Experiments suggest that exposure times are no greater than 2 seconds per layer (for 100 micron layers), and resin settling times are generally around 4 seconds per layer. Adding these

times to the time allotted for the dipping process, each layer requires approximately 10 seconds to print. Thus, the vertical build rate is estimated to be 360 layers per hour. Thus, with a layer thickness of 25 micrometers, it would take about 33 minutes to print a part that is 5 mm tall.

Other factors contribute to build rate, such as light intensity and presence of photo absorbers in the resin. However, light intensity is held constant from print to print, and photo absorber impact is difficult to qualify and changes on a resin to resin basis.

5.2. System Embodiment Comparison (CQ2)

In this section, the second characterization question "*How does the performance of the system designed as part of this work compare to other systems of similar morphology*?" is answered. To accomplish this, the embodiment of this system is again presented in the context of the morphological matrix, though this time along side systems with similar embodiments.

5.2.1. Morphology Comparison

Below in Table 5-6, the four performance parameters minimum feature size, minimum layer thickness, maximum part size, and vertical build rate of this MPµSL system are summarized.

Table 5-6: Chart of performance parameters for the MPµSL system.

	Performance
Min. Feature Size	212 µm
Min. Layer Thickness	20 µm
Max. Part Size	6 x 8 x 36 mm
Vertical Build Rate	360 layers per hour

The designed system embodiment is shown along side systems of similar morphology in Figure 5-8. The system designed as part of this body of reseasrch is highlighted with a purple diamond.

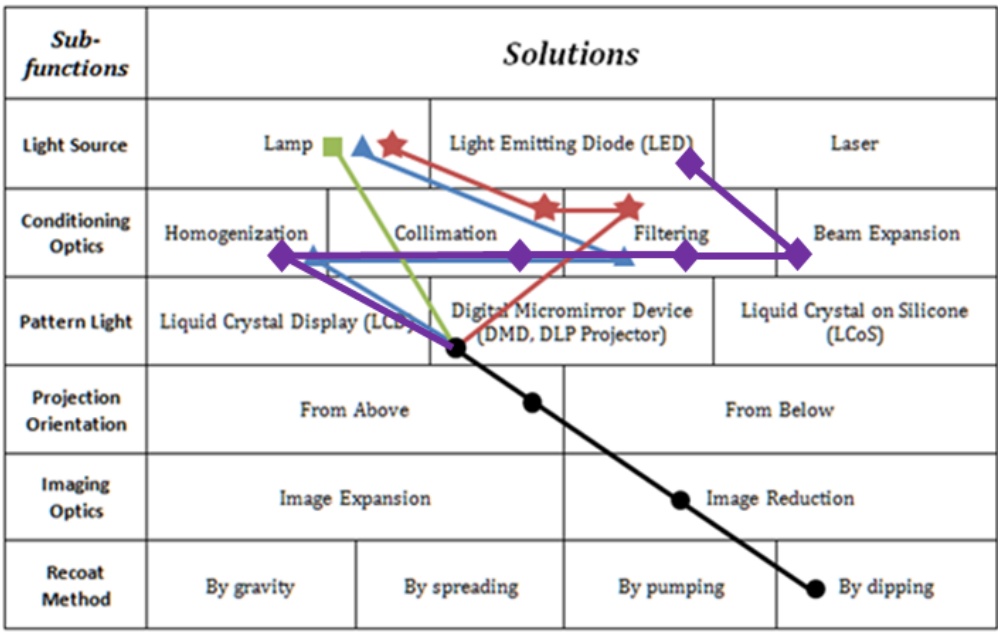

Figure 5-8: The designed MPμSL system embodiment outlined in the morphological matrix (purple diamond) with systems of similar embodiment.

As was stated in Chapter 2, "Design Considerations for Mask Projection Microstereolithography," it is very uncommon for projection stereolithography systems to have a UV LED as an energy source. With that under consideration, the performance metrics of the system embodiments outlined in Figure 5-8 are presented in Table 5-7.

The major differences between the system described with the purple diamond in Figure 5-8 and the other described systems are the light source and conditioning optics sub-functions. According to the QFD process planning matrix in Table 2-1, these sub-functions have weak interactions with all performance parameters, expect for the relationship between light source and vertical build rate (which was described as a medium strength relationship). In reality, there is much more that influences vertical build rate in the system design than the light source (motor speed, resin viscosity and critical exposure, software and processor delays, etc.) so this relationship can be largely disregarded as influential as well.

Table 5-7: Performance parameters of system embodiments similar to the MPµSL system designed in this research.

	Ref	Research Group	Year	Special Feature	Min. Feature Size	Min. Layer Thickness	Maximum Part Size	Vertical Build Rate
♦	N/A	*Williams*	*2014*	*DMD, 365 nm*	*212 µm*	*20µm*	*6 x 8 x 36 mm*	*360 layers/hr*
★	[6]	Rosen	2007	DMD, 365 nm	6 µm	400 µm	2 x 2 x 1 mm	90s per layer
★	[7]	Rosen	2007	DMD, 365, 435, 647 nm	5 µm	5 µm	not reported	60s per layer
★	[30]	Wicker	2009	DMD, 365 nm	30 µm	4 µm	1.95 x 1.95 x 2.4 mm	<1s per layer
★	[4]	Lee	2008	DMD, 365nm, XY translation	2 µm	5 µm	10 x 10 x 2.68 mm	100s per layer
★	[8], [9]	Bertsch	1999	DMD, visible	5 µm	5 µm	6 x 8 x 15 mm	280 layers/hr
★	[31], [36]	Bertsch	2000	DMD, UV	10 µm	10 µm	10.24 x 7.68 x 20 mm	200 layers/hr
▲	[5]	Zhang	2005	DMD, 364 nm, fly-eye lens	0.6 µm	5 µm	not reported	not reported
■	[32]	Roy	2006	DMD, 355 nm	20 µm	150 µm	not reported	90s per layer
■	[33]	Hadipoespito	2003	DMD, 365 nm	20 µm	100 µm	not reported	not reported

As a result, performance comparisons will be made between the systems from literature and the designed system with regard to the four remaining sub-functions. However, as was mentioned earlier, layer thickness is dependent upon motor selection (resolution). This makes it trivial to compare the minimum layer thickness parameter. Vertical build rate is also trivial to compare due to the non-normalized method of print speed reporting, and the multitude of factors that contribute to overall vertical build rate. The recoat method and the projection orientation contribute to the overall build rate, but are no way indicative of any trends in print speed.

Therefore, the focus of the comparison analysis to answer CQ2 will be minimum feature size and maximum part size.

5.2.2. Performance Parameters Analysis

From the QFD matrix, the remaining sub-functions Pattern Light, Projection Orientation, Imaging Optics, and Recoat Method, are all listed as having strong relationships with minimum feature size. These sub-functions' design decisions are shared between the systems presented in Table 5-7 found in literature and the designed system. This means that similar performance is expected between these systems, and that these four shared sub-functions are critical to minimum feature size performance.

The minimum feature size achieved in this system design is reported as 212 micrometers. This is significantly larger than all systems reporting similar embodiments. The range of achievable feature sizes for this group of systems is 30 micrometers down to 0.6 micrometers, with the average being about 12 micrometers. The systems that report feature sizes from 2-6 micrometers (close to the theoretical resolution of the designed system) list X-Y build areas similar to the designed system. This suggests that with pattern light, projection orientation, imaging optics, and recoat sub-functions employed in this system, a 5 micrometer feature size is attainable.

5.2.3. Improvement Considerations

The current system is underperforming by a large margin with a feature size reaching only as small as 204 microns with the benchmark test, and 38 microns with the cone experiment. During experimentation, it was noticed that if the build plane was moved any significant distance away from the focal plane of the projected image, light intensity and image focus changed drastically. Initially, this was considered by the author to be the limiter in feature size. However, regardless of the diligence taken to ensure the correct positioning of the focusing lens system, build platform, resin level, and DMD mount, the smallest feature size of the cone could be reduced to no smaller than 38 micrometers. This suggests that there are other factors impacting the resolution limit of this MPµSL system, which are explored further in Section 6.1.

5.3. Dimensional Comparison (CQ3)

The dimensional accuracy of the printer is critical to characterizing system performance, but cannot be easily classified as a performance parameter like maximum part size or minimum

feature size. Dimensional accuracy is instead classified by comparing the digital, designed model to the printed 3D part. The analysis tools used to determine dimensional accuracy were digital microscopy and micro-computed tomography (micro-CT) scanning.

5.3.1. XY Plane Accuracy

The sample benchmark parts printed for accuracy measurements were fabricated according to the 25 micrometer layer exposure as determined by the working curve. The benchmark part presented in Figure 4-2 was printed three times, and 16 key measurements were made on each sample to determine the dimensional accuracy of the printer in the XY plane. The 16 critical measurements are presented and labeled in the CAD schematic Figure 4-4.

A top down image of a printed test part is shown in Figure 5-9 to demonstrate how the measurements were conducted in the XY plane.

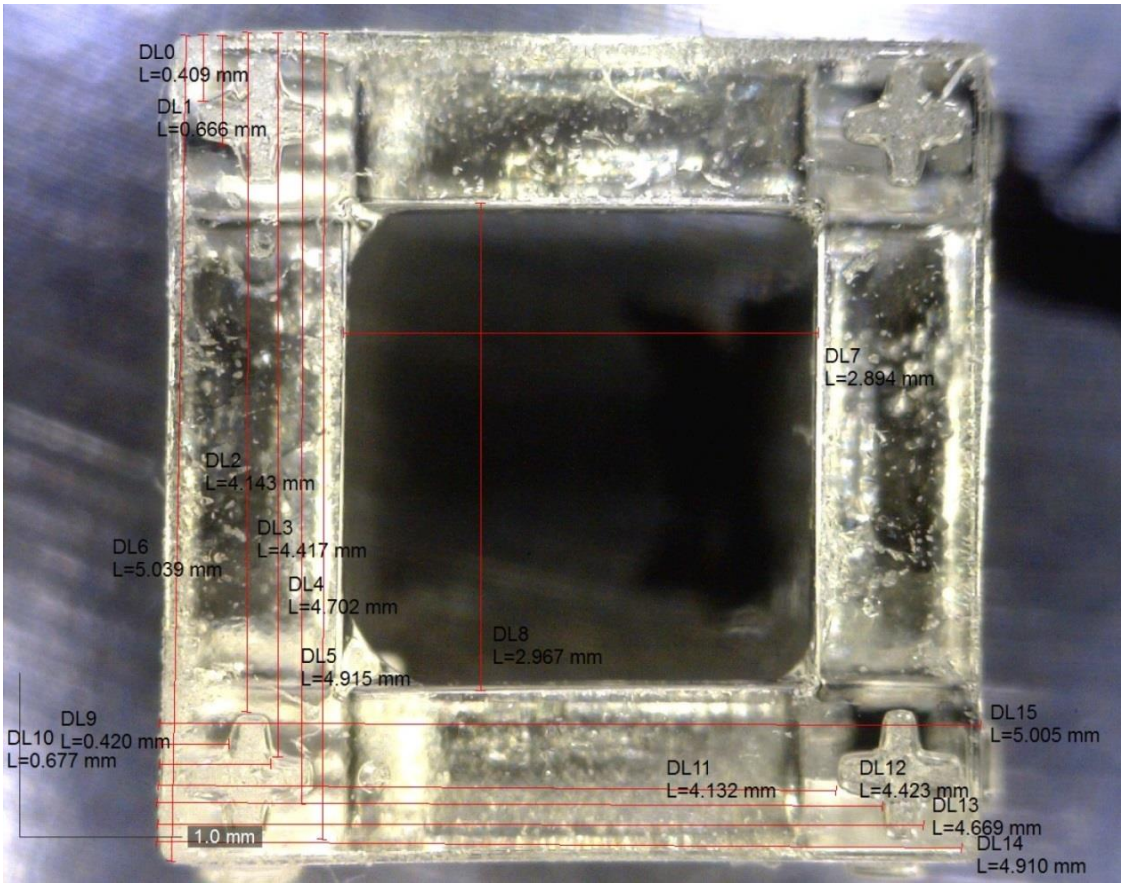

Figure 5-9: Image of a printed benchmark sample part with critical dimensions measured.

As mentioned, three sample benchmark parts were fabricated and measured using the method described. The data from the measurements of the three samples is shown below in the Table 5-8.

Table 5-8: Data collected from the XY plane dimensional accuracy analysis of the benchmark part.

	Design (mm)	*Sample 1 (mm)*	*Sample 2 (mm)*	*Sample 3 (mm)*	*Average*	*Std. Dev.*	*% Error*
X1	0.4	0.386	0.42	0.403	0.403	0.014	0.8%
X2	0.6	0.655	0.677	0.621	0.651	0.023	8.5%
X3	4.13	4.064	4.132	4.075	4.090	0.030	1.0%
X4	4.4	4.333	4.423	4.305	4.354	0.050	1.1%
X5	4.6	4.602	4.699	4.591	4.631	0.049	0.7%
X6	4.88	4.809	4.91	4.798	4.839	0.050	0.8%
X7	5	4.966	5.005	4.971	4.981	0.017	0.4%
X8	3	2.861	2.894	2.889	2.881	0.015	4.0%
Y1	0.4	0.403	0.409	0.414	0.409	0.004	2.2%
Y2	0.6	0.705	0.666	0.644	0.672	0.025	11.9%
Y3	4.13	4.131	4.143	4.092	4.122	0.022	0.2%
Y4	4.4	4.355	4.417	4.372	4.381	0.026	0.4%
Y5	4.6	4.63	4.702	4.635	4.656	0.033	1.2%
Y6	4.88	4.876	4.915	4.87	4.887	0.020	0.1%
Y7	5	5.027	5.039	4.999	5.022	0.017	0.4%
Y8	3	2.911	2.967	2.917	2.932	0.025	2.3%

According to the data, the average deviation of all measurements from the designed part was 0.038mm, with a maximum at 0.119mm at X8 and a minimum of 0.03mm at X1. The data was synthesized into percent error and overall standard deviation, which is presented in Table 5-9.

Table 5-9: Percent Error and Standard Deviation information for the XY accuracy experiment.

	% Error
Sample 1	2.9%
Sample 2	2.7%
Sample 3	1.9%
Average	2.5%
Std. Dev.	0.035 mm

The percent error from the designed value of all XY measurements averages at 2.5%, and all XY accuracy measurement data had a standard deviation of 35 micrometers from the designed dimension.

5.3.2. Z Dimension Accuracy

The following image Figure 5-10 shows the lateral view of the benchmark part with the critical dimensions shown, which was used to access the Z dimension accuracy of the printer. The same sample parts used to analyze XY dimension accuracy were also used to access Z dimension accuracy.

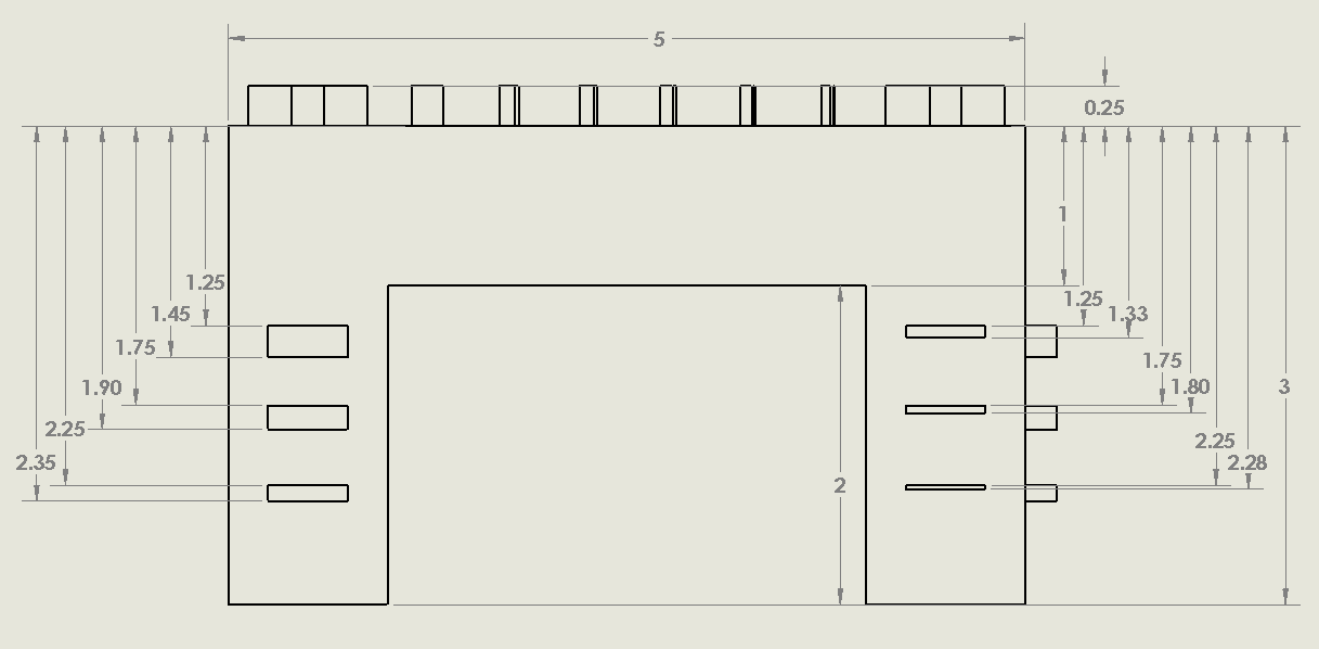

Figure 5-10: CAD schematic of the critical dimensions to analyze Z dimension accuracy.

The image below is a representative image of the 3 test parts (each with XZ and YZ faces).

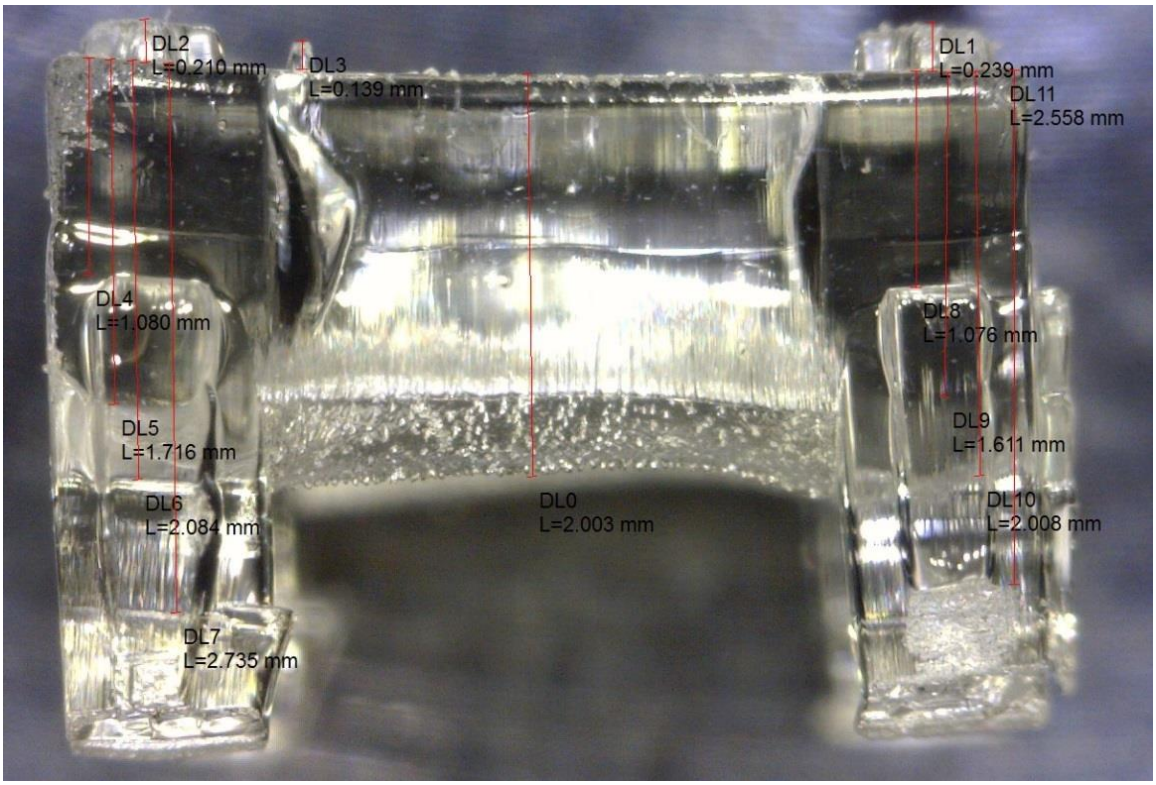

Figure 5-11: Representative image of the XZ/YZ dimensional analysis for Z axis accuracy.

The features on the lateral XZ and YZ face of the benchmark test part are not measurable. As the lateral extrusions have no discernable horizontal edges at which to make measurements, the only meaningful qualitative value is the thickness of the cross beam. As the cross beam in most parts generated an arc-like shape, the measurement was made at the center of the beam for consistency. The lack of lateral definition was somewhat expected due to the high depth of penetration, D_p, of the PPGDA resin with 2wt% initiator. Below, in Table 5-10 , the thickness of the cross beams in the 3 test parts are presented.

Table 5-10: Data for the measurement of the cross beams on the XZ and YZ faces of the sample parts.

	Design (mm)	*Sample 1 (mm)*	*Sample 2 (mm)*	*Sample 3 (mm)*	*Average*	*Std. Dev.*	*% Error*
XZ	1	2.71	2.578	1.979	2.422	0.318	142%
YZ	1	2.07	1.793	2.003	1.955	0.118	96%
				Overall	2.189	0.267	119%

The Z accuracy of the system with the PPGDA resin is extremely poor. Based on the measurements above, the average cross beam thickness was 2.19, over 1.18mm greater than the designed 1mm thickness. This means the system is exhibiting print-through error of 119%.

5.3.3. SEM and Micro Computed Tomography (Micro-CT)

Dimensional accuracy was also analyzed with a basic scaffold shape using Micro Computed Tomography (Micro-CT) and Scanning Electron Microscopy. A CAD model of the test part is presented in Figure 5-12. The overall dimensions are 4mm x 4mm x 8mm with lateral pores of 0.8mm x 1.6mm, and central vertical pores of 0.8 mm x 0.8 mm. All cross beams are 0.4mm width and 0.8mm in depth, and the vertical pillars are 0.4mm width.

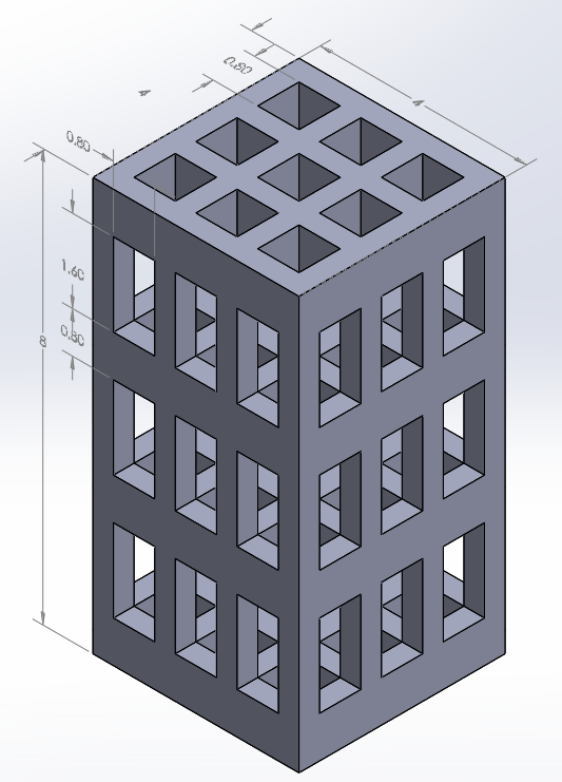

Figure 5-12: CAD model of the scaffold model used for test printing. All dimensions are in millimeters.

A test part was printed from the same PPGDA material characterized in Figure 5-2, with 100 micrometer layers (an exposure energy of 6.11 mJ/cm^2). A SEM image of the PPGDA scaffold part is shown in Figure 5-13.

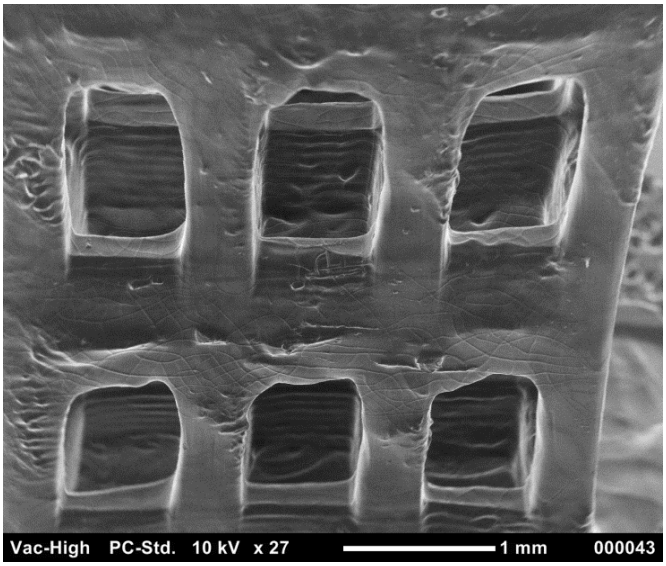

Figure 5-13: SEM image of the scaffold part.

The SEM image shows arching features indicative of the print through error. To determine the extent of which print through caused dimensional inaccuracy, a micro-computed tomography scan was created from the printed scaffold part. In Figure 5-14, the designed scaffold model and the micro-CT generated model are shown side by side.

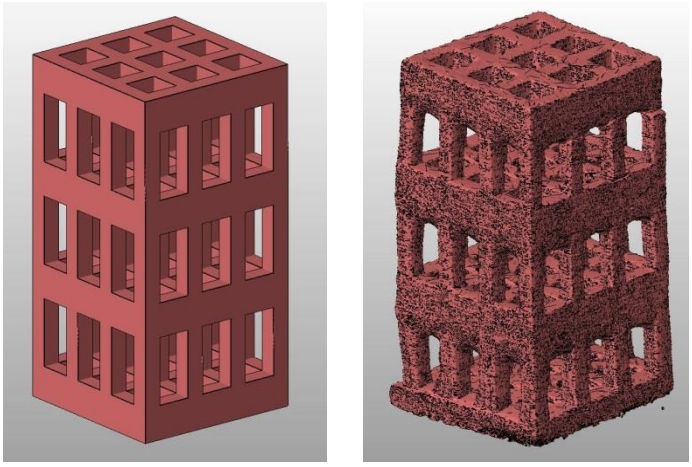

Figure 5-14: (Left) CAD model of designed scaffold. (Right) Micro-CT scan model of the printed scaffold.

With a digital model generated from the actual printed part, the mesh deviation was calculated using Geomagic Design X. By assigning the designed CAD model as the reference model, and the micro-CT scan as the target, and aligning the coordinate system of the two STL models, the mesh deviation was determined (Figure 5-15).

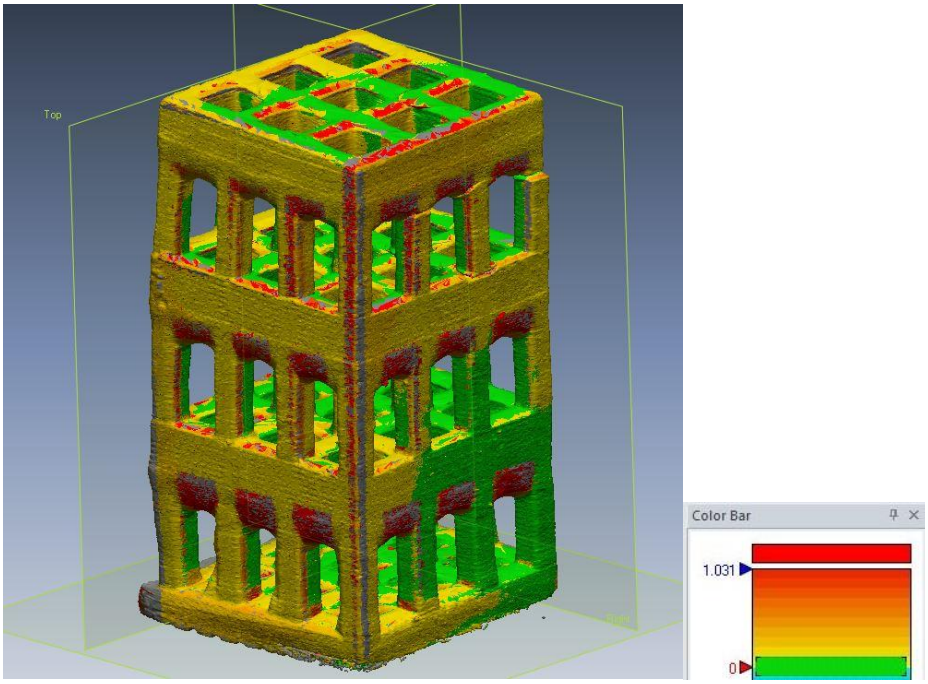

Figure 5-15: Mesh deviation calculation for the micro-CT scan of the printed scaffold.

The color bar on the right indicates the unsigned deviation of the micro-CT model from the reference model, with bright red being 1 mm. The tolerance of the color bar is 0.1mm, meaning that everything that falls within 0.1mm is within the allowable tolerance, and remains green. The value of the data from this micro-CT scan comparison was used qualitatively, confirming the results of the print-through error exhibited in the experiments performed with the benchmark part.

It is clear from the image in Figure 5-15 that print-through is the most constant and critical dimensional inaccuracy that the system is exhibiting. There are other areas of bright red on the top face of the scaffold and along the longitudinal corner facing the viewer, but these are not necessarily representative of dimensional inaccuracy. The printed scaffold part was leaning

slightly when the micro-CT scan was administered, which caused issues when aligning coordinate systems. The result is strong alignment showing little deviation at the bottom of the model, while the top face shows displacement in the mesh. This is not believed to be indicative of the printing process.

5.4. Areas for System Improvement

The take away from the analysis conducted in this chapter is that there are two major areas for improving the system performance: minimum feature size and dimensional accuracy in downward facing surfaces. Presumably, minimum feature size should reach ~5 micrometers, and there is some phenomenon occurring that prevents it. Regarding print through, researchers have demonstrated methods in which these errors have been remediated. The first of which is the use of a UV photo-absorber [4], [26], [34], [38], [50] to tune the working curve of the resin and reduce the depth of penetration. Another technique is to develop a software algorithm that subtracts a tailored volume from underneath the CAD model in order to compensate for the print-through [27].

Chapter 6 presents and tests hypotheses for improving these two areas of underperformance.

6. Improving System Performance

From Chapter 5 "Benchmarking the MPμSL System," two characteristics have been identified where performance can be improved: feature size and Z-accuracy. In this chapter, two experiments are presented. The first experiment, defined by Research Question 1, addresses the feature size performance by comparing exposure energy to minimum printable feature size. The second experiment compares the Z accuracy of a photopolymer mixed with varying amounts of a UV photo absorber, as outlined by Research Question 2.

6.1. XY Minimum Feature Size (RQ1)

The goal of this experiment was to determine the answer to Research Question 1.

RQ1: *How does minimum feature size vary with exposure energy?*

This research question stems from the results of the benchmarking of minimum feature size. It is hypothesized that features smaller than 212 micrometers are not receiving enough energy to reach the threshold energy required for polymerization. Literature suggests that this threshold may be the result of free-radical scavenging of oxygen present on the resin surface. To determine the process/property relationship between exposure energy and feature size, or how minimum feature size varies with exposure energy, the exposure duration was incrementally increased to overcome the oxygen free radical consumption. The theory of oxygen inhibition is explained in 6.1.1, the methods for the experiment are described in 6.1.2, and the results of the experiment are presented in 6.1.3.

6.1.1. Context: Oxygen Inhibition

Oxygen inhibition is the impeding effect that ambient oxygen has on the photo-polymerization acrylate free-radical crosslinking. Oxygen is a radical scavenger and competes strongly for the generated free radicals. Until the majority of the oxygen present at the reaction site is depleted through reaction with radicals, there is very little polymerization. The threshold to start polymerization, E_c, is primarily imposed through this oxygen inhibition [3], [25].

Many researchers speak about the inhibition effects due to the presence of oxygen on the polymerization surface [15], [25], [51]–[54]. Some addressed this issue by conducting the

polymerization reaction in an inert atmosphere [3], [7]. Other groups utilize a technique with a "constrained surface," where the build surface is in contact with a optically clear substrate and isolated from the effects of oxygen inhibition [15], [37], [39], [55].

Jariwala et. al. [25] developed an ODE based model for determining the effects of oxygen inhibition in masked-based stereolithography. The focus of this study was to model cure depth as a function of exposure in atmospheres of varying oxygen concentration. Their results match the findings of those presented by another research group, Zheng et. al [3], showing that cure depth increases with a reduction of ambient oxygen concentration (Figure 6-1).

However, the results of the experimentation conducted by Jariwala show that there is reduction in the width of cured lines when compared to the computational model (dotted line vs. solid in right chart). Furthermore, they observed that cured line width increases with increase in exposure. These findings suggest that increased exposure may indeed overcome oxygen inhibition effects in small features. Presumably, as the line is exposed to greater energy, free radicals are generated at a faster rate than oxygen consumes them. It is this phenomenon that may be driving the limited feature sizes exhibited in the benchmark feature size experiment. The next section outlines the experimental process conducted to determine how exposure effects feature size.

6.1.2. Experimental Method

The benchmark part presented in Figure 4-2 was designed with cylinders of decreasing diameters to access printable minimum feature size (Section 4.3). Using the exposure energy according to the working curve for 25 micrometer layer thickness, the smallest printed cylinder averaged 212 microns in diameter, as was demonstrated in Chapter 5. This experiment addresses RQ1 by incrementally increasing exposure energy (by increasing the time each layer is irradiated).

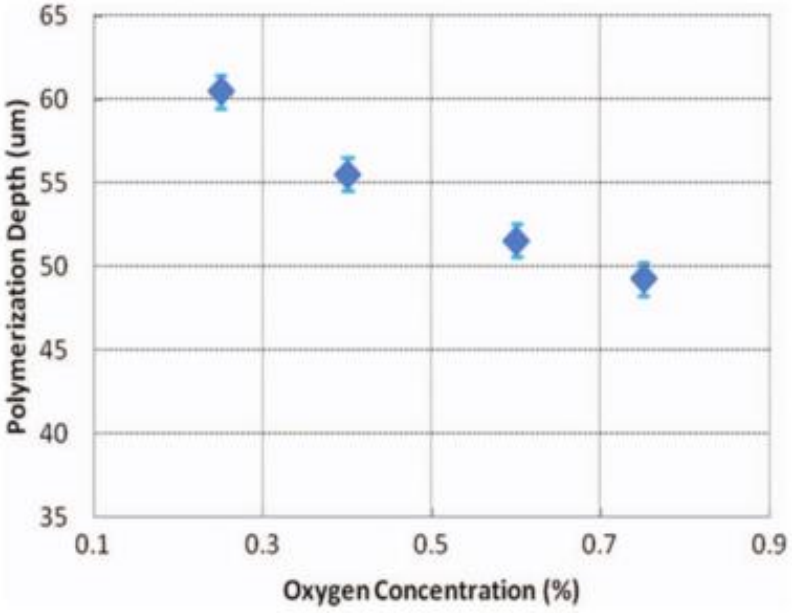

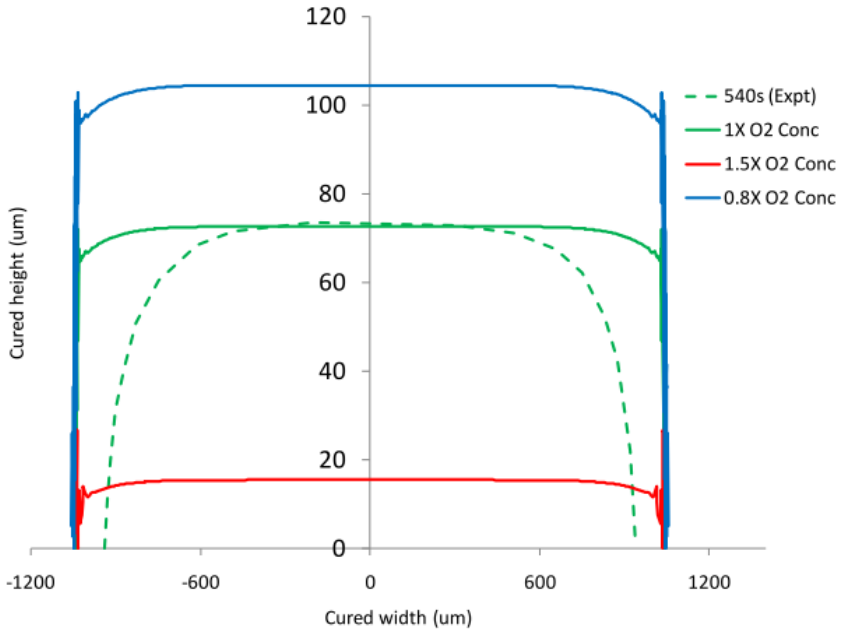

Figure 6-1: (Top) Zheng et. al. demonstrate effects of oxygen concentration on polymerization depth (X. Zheng, J. Deotte, M. P. Alonso, G. R. Farquar, T. H. Weisgraber, S. Gemberling, H. Lee, N. Fang, and C. M. Spadaccini, "Design and optimization of a light-emitting diode projection micro-stereolithography three-dimensional manufacturing system.," *Rev. Sci. Instrum.*, vol. 83, no. 12, p. 125001, Dec. 2012., Used under fair use, 2014). (Bottom) Jariwala

et. al. show reflective results (A. Jariwala, F. Ding, and D. W. Rosen, "Modeling effects of oxygen inhibition in mask-based stereolithography," *Rapid Prototyp. …*, vol. 17, no. 3, pp. 168–175, 2011., Used under fair use, 2014).

In addition to the sample parts fabricated in Section 5.1.3 at 1.19 second exposure (5.83 mJ/cm^2), three additional sample benchmark parts were printed using the PPGDA with 2wt% DMPA initiator at 3 seconds exposure (14.7 mJ/cm^2) and 5 seconds exposure (24.5 mJ/cm2). The parts were removed from the build platform, rinsed with IPA, and left to dry overnight. Using a digital microscope, the XY face of the benchmark part was examined to determine the smallest cylinder that printed. Measurements were made on both the X axis and the Y axis of the benchmark part. Furthermore, the cylinder designed to be 200 micrometers in diameter (the largest cylinder) was also measured on each sample (as it printed on all sample parts) to determine how the larger features are affected by the higher exposures.

The images in Figure 6-2 and Figure 6-3 are examples of how the measurements were collected from the XY plane of the benchmark test part printed samples. Again, the DinoLight Pro Digital Microscope and the associated DinoCapture 2.0 software were used to capture and measure images of the printed samples.

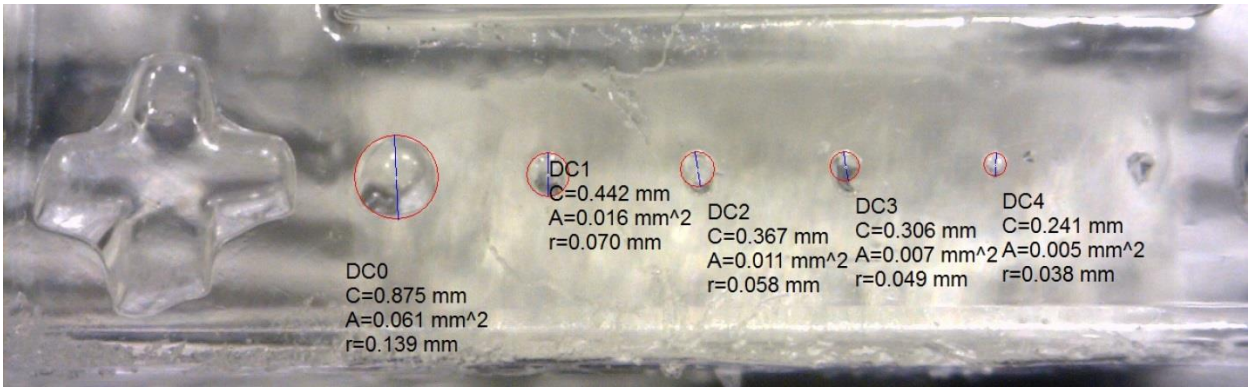

Figure 6-2: X axis measurements for minimum feature size analysis on the benchmark part.

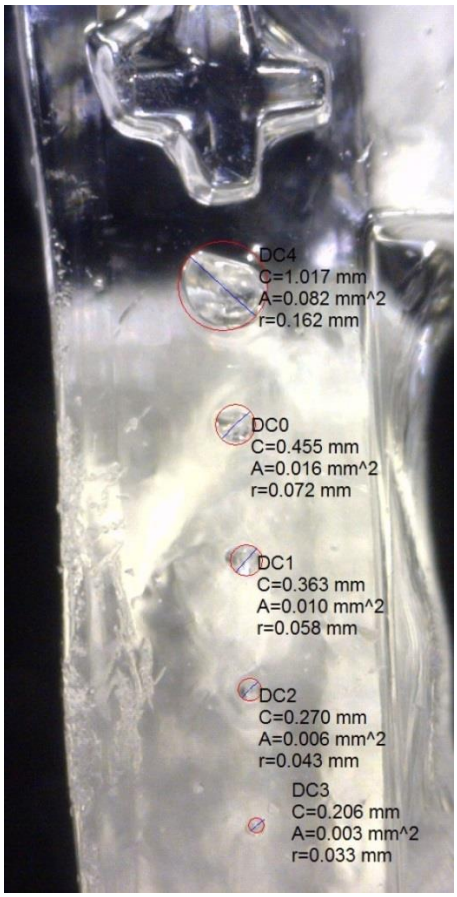

Figure 6-3: Y axis measurements for minimum feature size analysis on the benchmark part.

6.1.3. Experimental Results and Analysis

Overall, 18 data points were collected from the 9 manufactured benchmark sample parts - 9 from each the X and Y axes. The data is summarized in Table 6-1.

Table 6-1: The average designed diameter of the smallest printed cylinder, the average actual diameter of the smallest cylinder, the standard deviation, and percent error.

	1.19 s	**3 s**	**5 s**
Avg. Designed Diameter (mm)	0.2	0.092	0.066
Avg. Diameter (mm)	0.212	0.101	0.070
Standard Deviation (mm)	0.006	0.028	0.008
% Error	6%	10%	5%

The data was synthesized into a chart (Figure 6-4) demonstrating the process/property relationship between the minimum achievable feature size of the benchmark part and exposure energy.

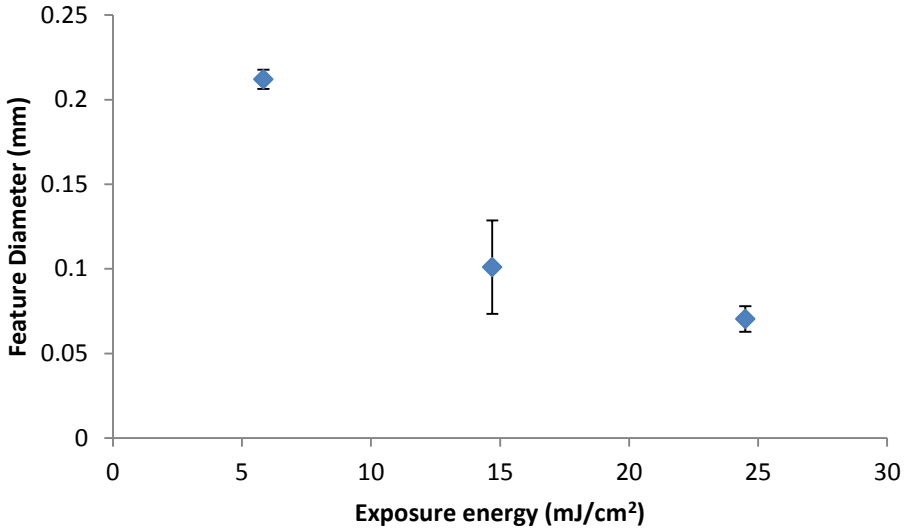

Figure 6-4: Chart demonstrating the relationship between exposure energy and minimum feature size of the benchmark part.

The data demonstrates a notable trend in achievable minimum feature size with increase in exposure. As mentioned earlier, in some cases, the smallest diameter cylinder that printed was not consistent among samples of the same exposure energy. This resulted in high standard deviation (28 micrometers for the 3 second exposure data) and high percent error (10% for the 3 second exposure data). There is also discrepancy between the size of some of the printed cylinders and the designed dimension. Regardless of the repeatability or accuracy of the experiment, there is a clear trend showing a process/property relationship between minimum feature size and exposure energy: with increased exposure, the achievable minimum feature size of the part increases as well.

6.1.4. Discussion

This result does not address the obvious pitfalls of overall exposure increase, such as increased print-through error or feature distortion. While the effects on print-through error were not

characterized in this experiment, the effects of over exposure were analyzed for the larger feature sizes. As the 200 micron diameter cylinder was present on every printed sample part, its printed diameter was also recorded. The results of this experiment are summarized in Table 6-2 and the chart in Figure 6-5.

Table 6-2: The average diameter, standard deviation, and percent error of the 200 micrometer cylinders on the benchmark part in the minimum feature size experiment.

	1.19 s	**3 s**	**5 s**
Avg. Diameter (mm)	0.212	0.286	0.287
Standard Deviation (mm)	0.006	0.029	0.024
% Error	6%	43%	44%

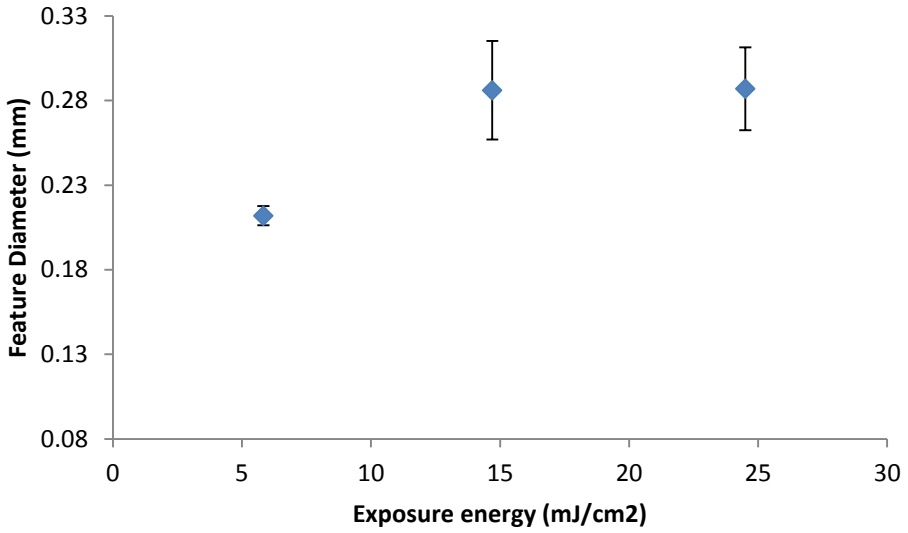

Figure 6-5: Chart demonstrating the effects of high exposure energy on the 200 micrometer cylinder from the benchmark part.

The data shows that the 200 micron diameter cylinder has very accurate dimensions in the 1.19 second exposure. However, the printed cylinder diameter increases with greater exposure durations. Furthermore, it is clear to see from lateral images that the cylinder has a wider base and a more slender tip, especially on greater exposure durations (Figure 6-6).

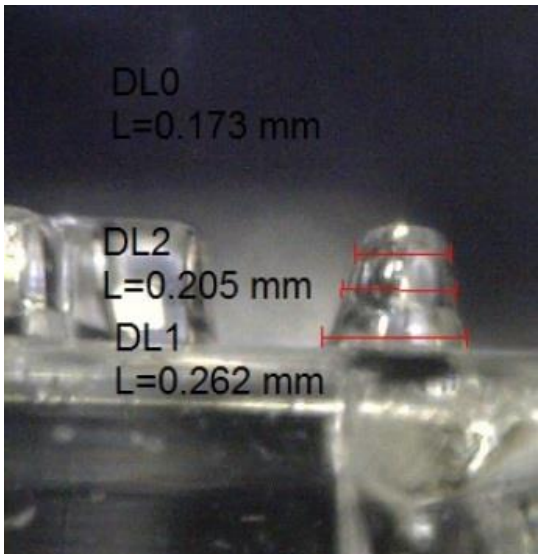

Figure 6-6: The 200 micron cylinder on a benchmark test part exposed for 5 seconds.

This experiment was limited by the form of the measurements conducted for this collection of data. The bird's eye view measurement method on the benchmark parts depended on focus of the image, and focus was put on the base of the cylinders. This was the only place where all cylinders shared an equivalent plane. This means that the tip of the cylinder is not being measured, which is likely where the most accurate and representative measurement can be made. A better way to conduct the measurement of the printed cylinders was a lateral view, looking at the part in the XZ or YZ plane. A view of a benchmark part from the lateral view (XZ plane), is shown in Figure 6-7.

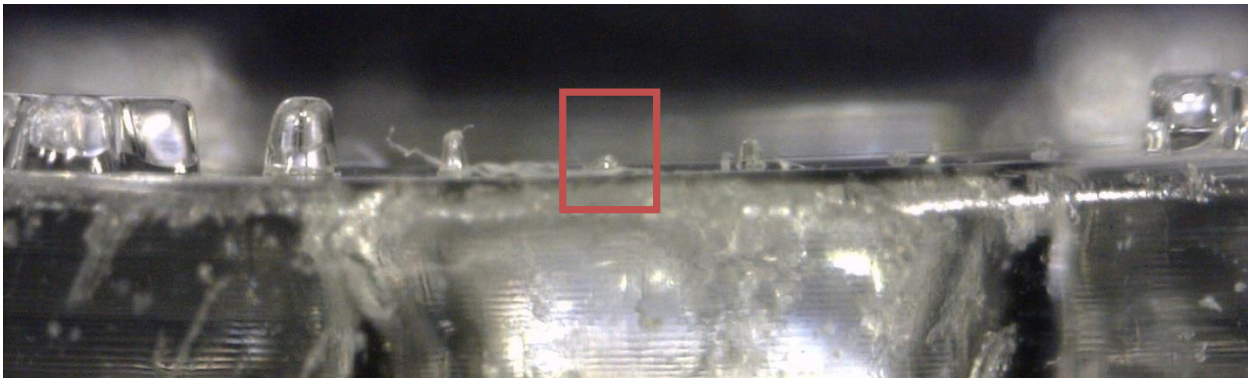

Figure 6-7: Lateral view of a benchmark part. A missing cylinder is outlined by the box.

This method was not chosen for measurement as several of the more fragile cylinders were broken off during the cleaning process, and their bases were not visible from a lateral view (demonstrated by the cylinder outlined in Figure 6-7. The top view was the only method with which to capture all the available data.

Further experiments should be conducted to confirm that feature size is related to oxygen concentration. The experiment conducted by Jariwala to determine oxygen effects on cure depth should be repeated with the focus on minimum feature size. This experiment will confirm suspicions of oxygen effects on feature size, and contribute to the modeling effects of oxygen on curing of photo-crosslinking resins. Ultimately, the goal of oxygen inhibition modeling will provide a greater understanding for MPμSL printing in an oxygen rich atmosphere.

6.1.5. Implementation of Results

For future system improvement, the author suggests that an auxiliary state be introduced into the software state machine architecture. This new state would scan the current image being projected for features smaller than 212 micrometers (minimum feature size of benchmark part with standard exposure energy), and generate a secondary image containing only these features. This secondary image would project some significant duration longer than the original layer to fabricate the small features. This duration would be controllable from the front panel of the user interface.

Prior to implementation, an investigation should be conducted to determine the effects of the increased exposure for small parts on print-through. As overall accurate dimensions are critical to successful fabrication, it may not be a fortuitous tradeoff to increase feature size at the risk of increasing print-through errors.

6.2. Cure-depth Control via Photoabsorber (RQ2)

The results of CQ2 presented a significant accuracy issue in the Z-dimension called print-through. Print-through is a common problem in vat photopolymerization processes, and occurs due the uncontrolled penetration of UV light into photopolymer resin when fabricating down-facing surfaces [26], [56]. Several approaches have been presented in literature to account for

print-through, including a software based “Compensation Zone” approach by Limaye/Rosen [27]. However, a different approach is used where UV photo-absorber is introduced into the resin to alter the curing characteristics and reduce the penetration depth of UV light. A common type of UV photo-absorber is Tinuvin 400, and is the photo-absorber explored in Research Question 2 (RQ2).

RQ2: *How does Z-axis accuracy vary with increasing Tinuvin 400 concentration in the prepolymer?*

This question aims to determine the structure/property relationship between Tinuvin 400 concentration in a photo-curable prepolymer and Z-axis accuracy. The relationship between Tinuvin 400 concentration in an acrylate-based photopolymer and Z-axis accuracy was explored by designing and conducting an experiment that varied the concentration of Tinuvin 400 in the photopolymer resin. A working curve was developed and a benchmark part was printed for each concentration, and XZ and YZ feature accuracy was determined.

6.2.1. Photo-absorbers

Light absorbers, otherwise known as photo-absorbers or light stabilizers, are materials that are used in SLA processes to combat uncontrolled cross-linking of photopolymers. There are two mechanisms by which this process works. The first mechanism, utilized by a class of light absorber called Ultraviolet Light Absorber (UVA), absorbs the UV light and scatters it as thermal energy. The second mechanism, used by a class of light absorber called Hindered Amine Light Stabilizers (HALS), does not absorb UV energy but rather acts to inhibit cross-linking via oxygen inhibition through the removal or entrapment of radicals [57].

This research is focused on the more commonly used UVA class of absorbers, which are used primarily in stereolithography applications to reduce depth of cure and enable the generation of thin layers. Choi et. al. conducted experiments to determine the effect of Tinuvin 327, a UVA class light-absorber, on an acrylate photo-curable resin. The prepolymer consisted of IBXA, HDDA (1,6-hexanediol diacrylate), and BEDA (bisphenol-A-ethoxylated diacrylate) mixed with an 8:1:1 ratio by weight with a 5 w/w% of DMPA (2,2-dimethoxy-2-phenylacetophenone) as

photoinitiator [26]. The Tinuvin 327 was selected due to its high absorption at 365nm, and was mixed into the prepolymer at the varying ratios listed below in Table 6-3.

Table 6-3: Sample description for the Tinuvin 327 experiment as performed by Choi et. al. (J.-W. Choi, R. B. Wicker, S.-H. Cho, C.-S. Ha, and S.-H. Lee, "Cure depth control for complex 3D microstructure fabrication in dynamic mask projection microstereolithography," *Rapid Prototyp. J.*, vol. 15, no. 1, pp. 59–70, 2009., Used under fair use, 2014).

Material sample name	Tinuvin 327™ concentration (w/w) (percent)	Prepolymer
T0.00	0.00	IBXA: HDDA:
T0.05	0.05	BEDA = 8:
T0.10	0.10	1: 1 (by wt. %)
T0.15	0.15	DMPA 5 percent (w/w)

The samples were characterized, and working curves were developed. The working curves for these samples are shown in Figure 6-8 and the critical exposure and penetration depth are presented in Table 6-4.

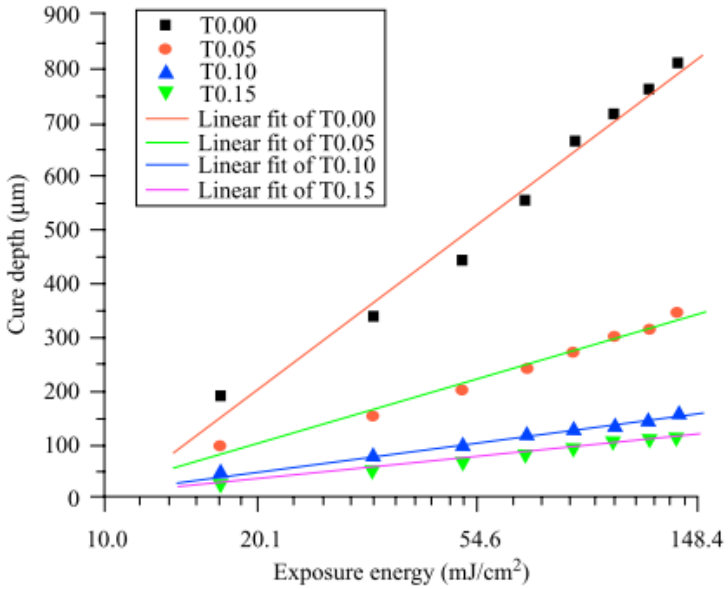

Figure 6-8: Working Curves for varying concentrations of Tinuvin 327 in the IBXA prepolymer (J.-W. Choi, R. B. Wicker, S.-H. Cho, C.-S. Ha, and S.-H. Lee, "Cure depth control for complex 3D microstructure fabrication in dynamic mask projection microstereolithography," *Rapid Prototyp. J.*, vol. 15, no. 1, pp. 59–70, 2009., Used under fair use, 2014).

Table 6-4: E_c and D_p for each Tinuvin 327 concentration (J.-W. Choi, R. B. Wicker, S.-H. Cho, C.-S. Ha, and S.-H. Lee, "Cure depth control for complex 3D microstructure fabrication in dynamic mask projection microstereolithography," *Rapid Prototyp. J.*, vol. 15, no. 1, pp. 59–70, 2009., Used under fair use, 2014).

Material sample name	Critical energy (E_c, mJ/cm^2)	Penetration depth (D_p, μm)
T0.00	10.4	308.0
T0.05	8.6	121.5
T0.10	7.9	53.6
T0.15	8.1	40.7

To demonstrate the ability of Tinuvin 327 to improve part quality and enable cure depth control for 3D microstructure fabrication, Choi et. al. used an MPμSL system to print microfan structures (Figure 6-9).

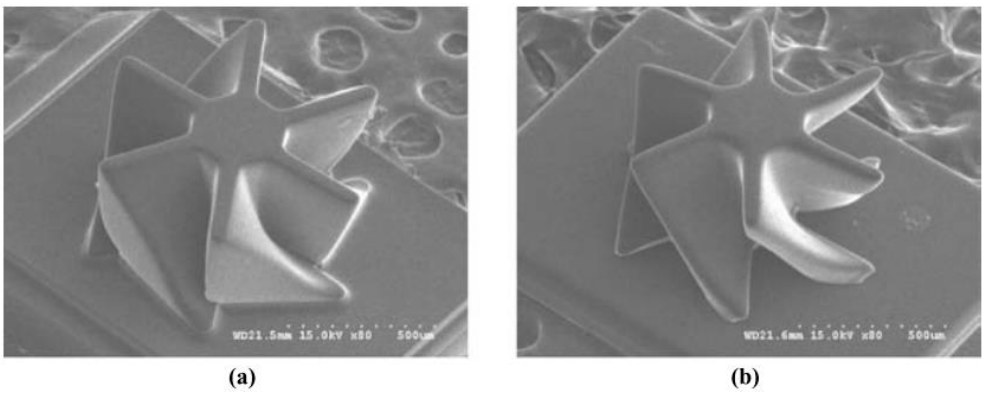

(a) (b)

Figure 6-9: Microfan structures printed with material (a) T0.00 and (b) T0.05 (J.-W. Choi, R. B. Wicker, S.-H. Cho, C.-S. Ha, and S.-H. Lee, "Cure depth control for complex 3D microstructure fabrication in dynamic mask projection microstereolithography," *Rapid Prototyp. J.*, vol. 15, no. 1, pp. 59–70, 2009., Used under fair use, 2014).

The microfan in image (a) shows significant print-through, with poorly fabricated down-facing surfaces. The microfan in image (b) demonstrates how 0.05% Tinuvin 327 can dramatically reduce the print-through error and generate dimensionally accurate features.

A second research group also conducted experiments to determine the effect Tinuvin 327 had on EnvisionTEC PIC-100 (1,1,1 Trihydroxymethylpropyl-triacrylate) photo-curing resin [56]. Zabti et. al. mixed Tinuvin 327 into the PIC-100 resin at 0.1%, 0.25% , 0.5%, and 1% (w/w) concentrations. The working curves for the PIC-100 resin mixtures is shown in Figure 6-10 and the critical exposure and penetration depth are shown in Table 6-5.

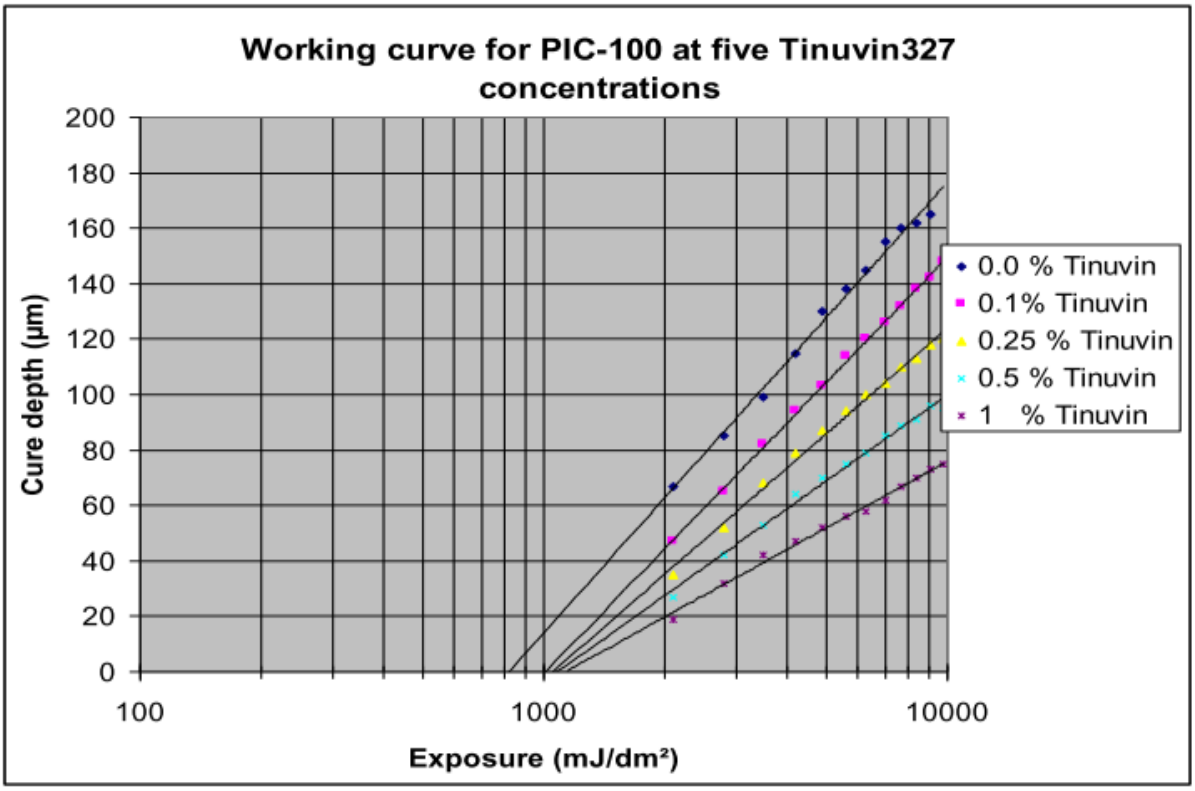

Figure 6-10: Working curves for PIC-100 at varying concentrations (w/w) of Tinuvin 327 (M. M. Zabti, "Effects of Light Absorber on Micro Stereolithography Parts," The University of Birmingham, 2012., Used under fair use, 2014).

Table 6-5: E_c and D_p of the PIC-100 at varying concentrations of Tinuvin 327 (M. M. Zabti, "Effects of Light Absorber on Micro Stereolithography Parts," The University of Birmingham, 2012., Used under fair use, 2014).

Tinuvin® Concentration %	Critical Energy (Ec, mJ/dm²)	Penetration Depth (Dp, µm)
0.0	820	70
0.1	1000	65
0.25	1052	55
0.5	1080	44
1.0	1132	34

The results of these experiments suggest that introducing an Ultraviolet Light Absorber into the PPGDA resin may decrease the penetration depth and reduce the print-through error affecting the accuracy of the Z dimension features.

6.2.2. Experimental Method

To test the impact that Ultraviolet Light Absorbers on the PPGDA resin and answer RQ2, liquid Tinuvin 400 (85% 2-hydroxyphenyl-s-triazine UVA (HTP) in 1-methoxypropan-2-ol) was acquired from BASF, chosen based on its good UV absorption [57], [58]. The prepolymer PPGDA was prepared with the standard 2 wt% DMPA as photoinitiator, and mixed with varying concentrations of the Tinuvin 400. The samples were then placed in a warm water bath (50°C) for an hour to dissolve the viscous Tinuvin 400 in the prepolymer. Four samples were prepared with the Tinuvin 400 concentrations listed in Table 6-6.

Table 6-6: Preparation of the PPGDA with varying Tinuvin 400 concentrations.

Sample Name	Tinuvin 400 Concentration (w/w %)	Prepolymer
T0.00%	0.00	Poly (Propylene Glycol)
T0.05%	0.05	Diacrylate, 2w% DMPA
T0.15%	0.15	(100 ppm MEHQ, 100
T0.25%	0.25	ppm BHT as inhibitor)

The four samples were returned to room temperature and characterized according to the polymer characterization process outlined in CQ1. Working curves for each sample were developed, and benchmark parts were fabricated with each sample to analyze the effects of Tinuvin 400 on Z-dimension accuracy. Images of the benchmark parts were taken with the DinoLight Pro Digital Microscope, and critical measurements were collected using the associated DinoCapture 2.0 software.

6.2.3. Experimental Results and Analysis

The working curves for the four materials are shown in Figure 6-11 and the critical exposure and depth of penetration for each material are presented in Table 6-7.

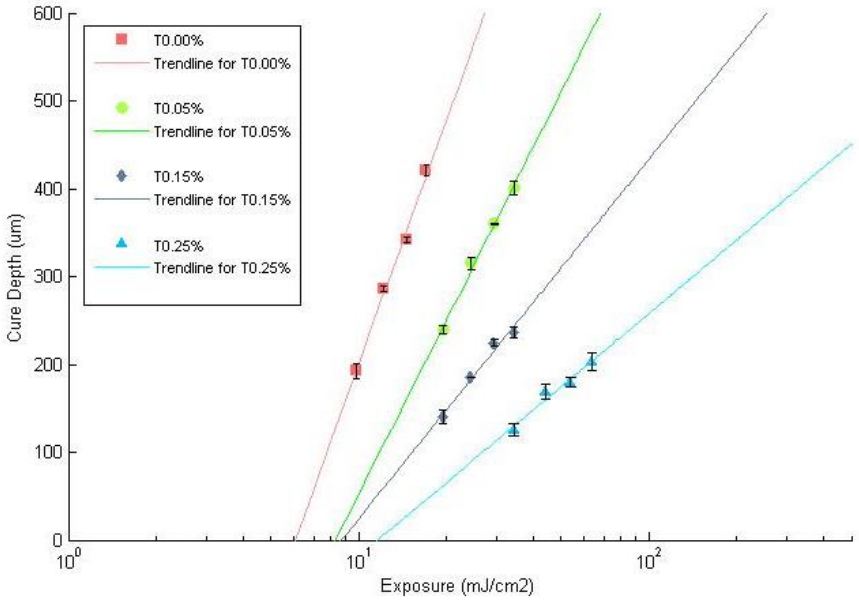

Figure 6-11: Working curve (cure depth according to exposure energy) for each material.

Table 6-7: The E_c and D_p for each material.

Sample Name	Critical Exposure E_c (mJ/cm2)	Depth of Penetration D_p (μm)
T0.00%	6.1	398.5
T0.05%	8.3	285.3
T0.15%	8.7	177.7
T0.25%	11.6	119.7

There is an observable trend in the reduction of the depth of penetration as the concentration of Tinuvin 400 increases. To understand how this affects the Z-dimension accuracy performance of the MPμSL system, benchmark parts were developed with each material, and their lateral extrusions measured. Due to material availability, one representative benchmark part was printed from each material. The results of the lateral extrusion and cross beam measurements of the benchmark part are presented in Table 6-8. The dimensions of the lateral extrusions are shown in Figure 5-10, and were designed in dimension pairs: the distance to the top of the extrusion, and the distance to the bottom of the extrusion (from the top face of the benchmark part).

Table 6-8: Percent error and standard deviation for the lateral extrusions of the benchmark part at different Tinuvin 400 concentrations.

	Lateral % Error	**Lateral Std. Dev.** (mm)
T0.00%	N/A	N/A
T0.05%	N/A	N/A
T0.15%	10%	0.104
T0.25%	6%	0.061

As the contributor to inaccuracy in the Z-dimension is a product of print-through, the source of the error in the measurements was typically the distance to the bottom of the extrusion. No data exists for the lateral features from the T0.00% and T0.05% material as the print-through

was so high that the features were indistinguishable from one another. As an alternative measurement method, the cross beam dimension was analyzed independent of the lateral feature data so that any trends, if apparent, could be identified.

Table 6-9: The average cross-beam depth of the Benchmark part and associated percent error from the design at different Tinuvin 400 concentrations.

	Avg. Beam Depth (mm)	**% Error**	**Std. Dev**
T0.00%	2.19	119%	0.267
T0.05%	1.4	40%	N/A
T0.15%	1.30	30%	0.177
T0.25%	1.09	9%	0.41

A chart is presented below demonstrating the average cross beam depth according to sample material (Figure 6-12).

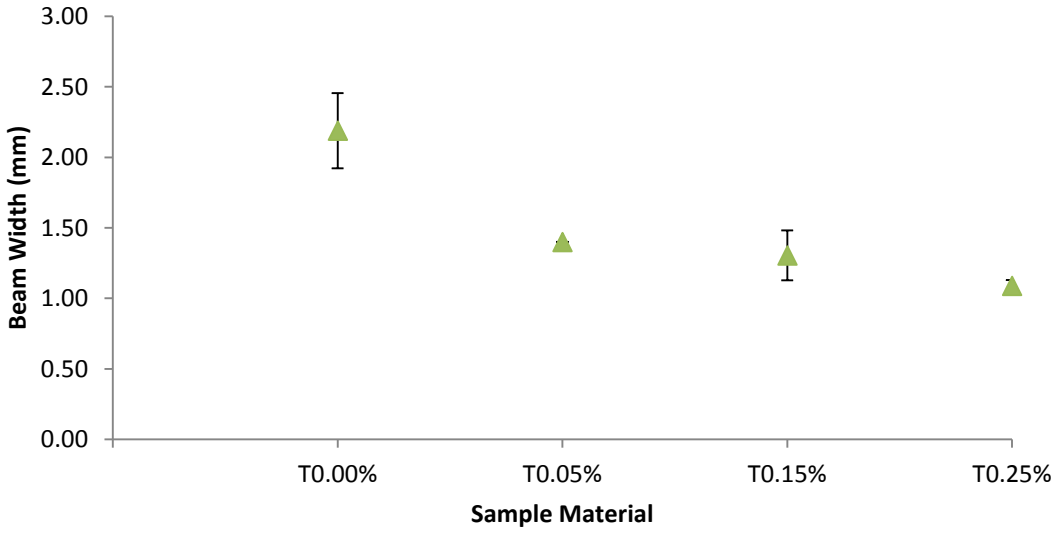

Figure 6-12: Chart presenting the relationship between cross-beam depth according to increased Tinuvin 400 concentrations.

To qualitatively show the structure/property relationship between Tinuvin concentration and Z-dimension accuracy, the figure below shows a part printed with T0.00%, T0.15% and T0.25%.

The images above distinctly show the lateral features are completely indistinguishable in the T0.00% sample part. The features begin to separate in the T0.15% sample part, and demonstrate complete separation and begin to resemble their designed shape with the T0.25% material. Furthermore, the individual 25 micrometer layers become more apparent. According to the data collected as part of this experiment, there is a clear and observable trend indicating the structure/property relationship between increased Tinuvin 400 concentrations and the associated Z-accuracy and feature size. As Tinuvin 400 increases, the percent error from the designed feature, as well as the standard deviation of the measurements, considerably reduces.

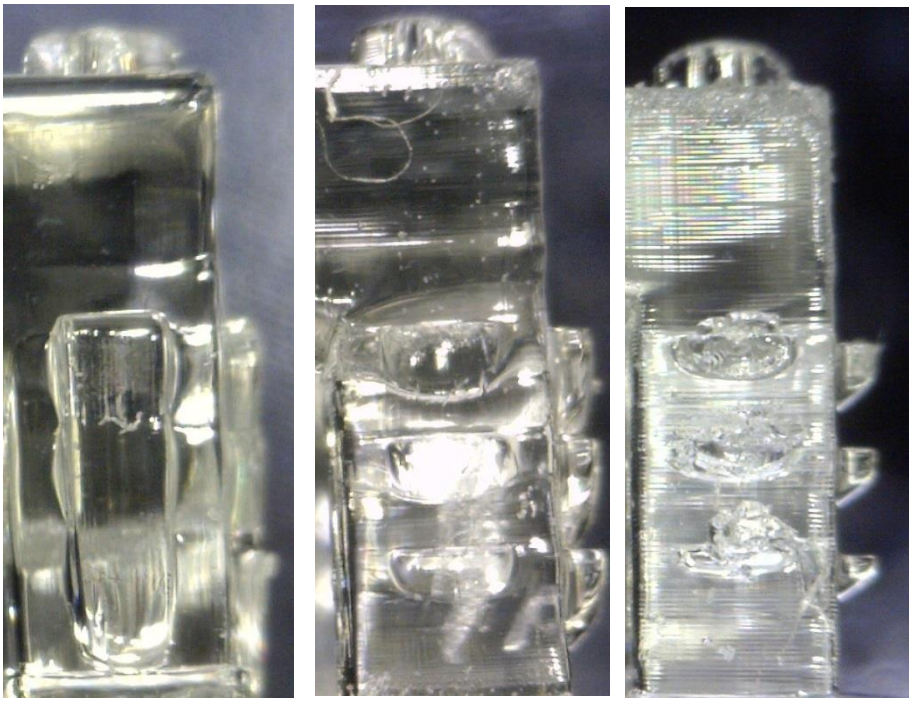

Figure 6-13: (Left) Benchmark part printed with T0.00%. (Center) Benchmark part printed with T0.15%. (Right) Benchmark part printed with T0.25%.

6.2.4. Discussion

The basic scaffold structures presented in Figure 6-14 demonstrate that the Tinuvin 400 can be used to reduce cure depths such that parts with accurate Z dimensions can be fabricated.

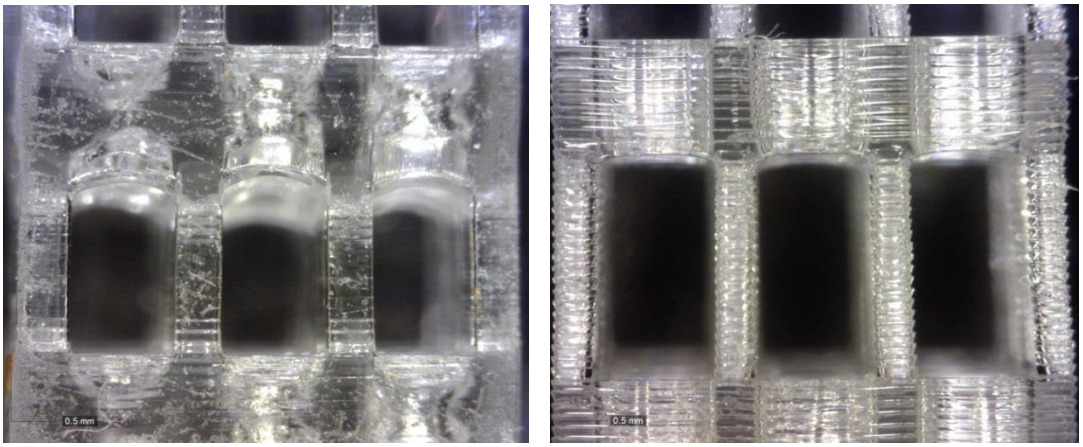

Figure 6-14: (a) Basic scaffold part printed with the T0.00% material. (b) Basic scaffold part printed with the T0.25% material.

The structures above, basic scaffold shapes printed with 100 micrometer layers, show a significant reduction in print-through from ~0.5mm down to 0.05mm. Furthermore, the arching overhangs seen in (a) are absent in image (b).

The results of the Tinuvin 400 experiment resemble those of the experiments conducted with the Tinuvin 327 as presented by Choi et. al. and Zabti in Figure 6-8 and Figure 6-10 [26], [56]. This shows promising results that Tinuvin 400 may be incorporated into future novel photo-curable resins with high depth of penetration. Used in small concentrations, Tinuvin 400 may be the solution for many photopolymers encountering poor Z-accuracy from MPμSL processing.

7. Novel Photopolymer Characterization

The MPµSL system designed in this body of research operates via custom designed software. The system operator has control over all of the print process parameters, including exposure and layer thickness. With this level of control, novel photo-curable resins can be introduced to the MPµSL machine and be used to fabricate complex 3D structures. Before 3D structures can be manufactured with these novel resins, their processability must first be determined.

Two novel photo-curable resins were introduced into the system and their performance characterized. They are Pluronic L-31 (Section 7.1) and Phosphonium Ionic Liquid (Section 7.2).

7.1.Pluronic L-31 (RQ3)

The block copolymer Pluronic L-31, as stated much earlier, is a polymer of interest due to its reported biocompatibility, which can be used to fabricate tissue engineering scaffolds. An cell viability experiment was conducted to examine the cytotoxicity of the polymer and determine if cells can survive on the surface of the films. The experiment compared films made from poly (propylene glycol) and the Pluronic L-31, both with and without fibronectin. MC3T3-E1 mouse preosteoblasts were seeded on PPGDA and Pluronic L-31 films and cultured for 7 days. Cell viability was quantified using an MTS assay. Average cell counts were conducted after 1 day, 4 days, and 7 days of incubation. The cell counts were based on three samples for each day. The results are shown in Figure 7-1.

While the Pluronic L-31 films (with and without fibronectin) do not show significant growth of cells over time, the PPG with fibronectin and the control wells show no growth either. The pure PPG films demonstrate growth from day 4 to day 7, but the error is so high that this trend is not significant. Though no growth was observed, this experiment demonstrates that the Pluronic L-31 can sustain cell life and is a viable candidate for further experimentation in the application of tissue engineering scaffolds.

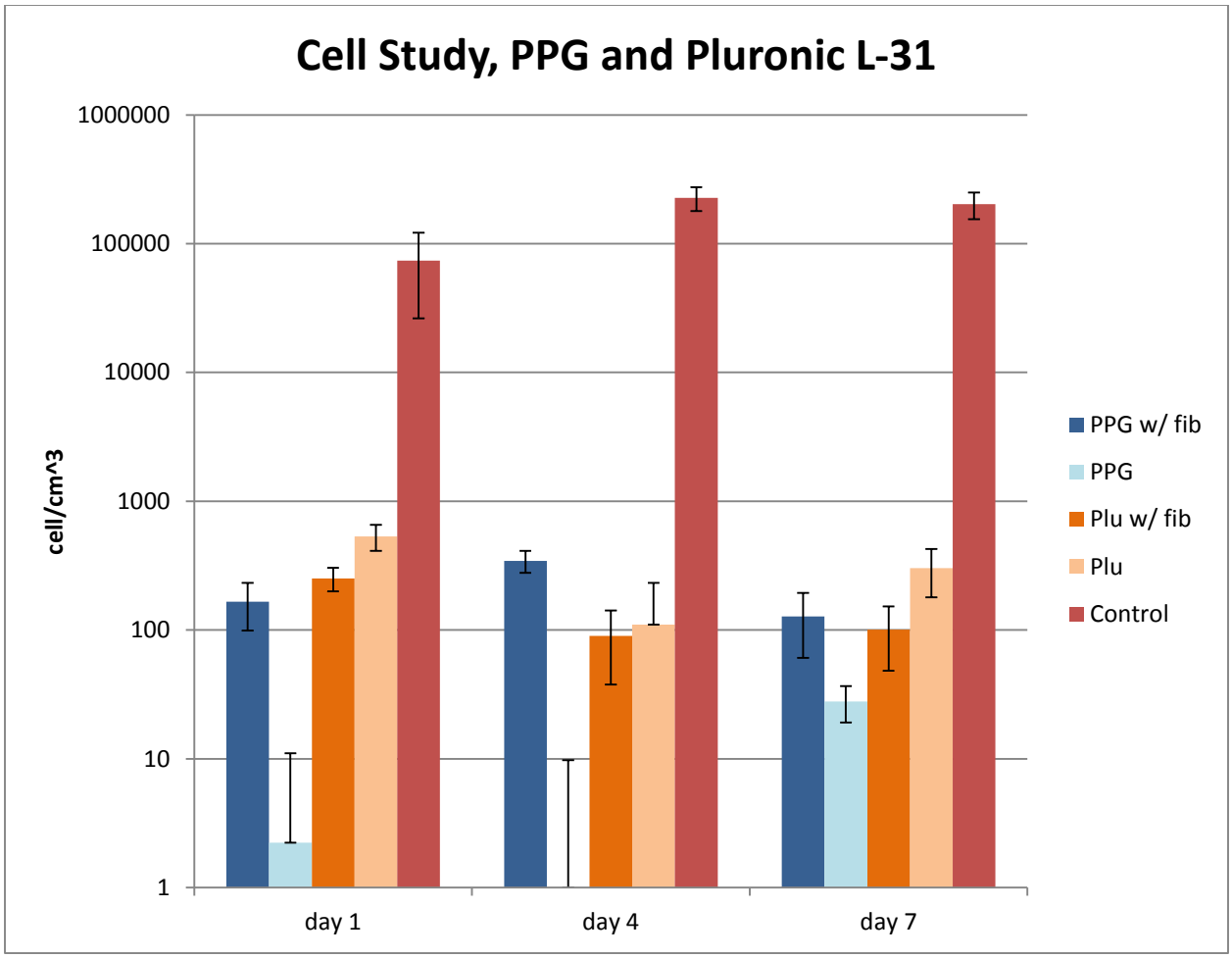

Figure 7-1: Cell study comparing cells present on the film surface after 1 day, 4 days, and 7 days of incubation (Used with permission of the Whittington Group, 2014).

With biocompatibility validated, the next step to making 3D structure with Pluronic L-31 is to understand how the Pluronic L-31 works with this MPµSL system. Research Question 3 (RQ3) was answered.

RQ3: *What are the curing characteristics of Pluronic L-31 how does it perform in the MPµSL system?*

This was accomplished by utilizing the process outlined in the answer to Characterization Question 1 in Section 4: "How can the curing characteristics of this photopolymer and its

performance with the MPμSL system be determined?" Following this process, the Pluronic L-31 resin was characterized, and its performance in the system was determined.

7.1.1. Materials and Methods

Pluronic L-31 is a co-block polymer with the chemical structure Poly(ethylene glycol)-block-poly(propylene glycol)-block-poly(ethylene glycol), shown in Figure 7-2. Some properties of the Pluronic L-31 polymer are listed in Table 7-1.

Table 7-1: Properties of Pluronic L-31.

Property	Value
Mol wt	~ 1,100 g/mol
Density	1.018 g/mL
Color	Amber
Viscosity	175 cP
Interest	Biocompatibility

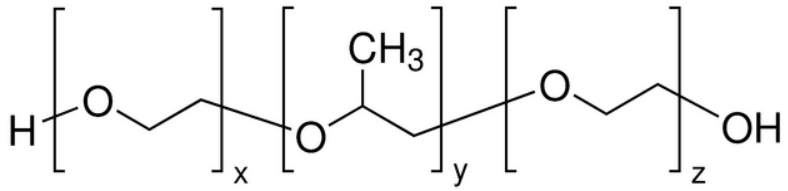

Figure 7-2: Chemical structure of the Pluronic L-31 oligomer.

The Pluronic L-31 resin was functionalized with reactive diacrylate end groups, making it compatible with the photo-crosslinking process. The functionalized oligomer is shown in Figure 7-3.

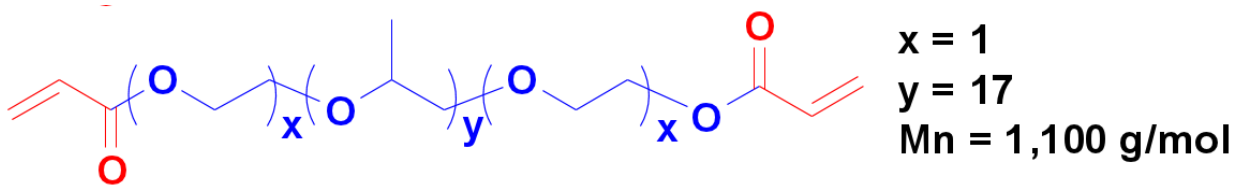

Figure 7-3: Functionalized Pluronic-L31 oligomer.

As was mentioned, the process outlined as part of CQ1 was used to characterize the functionalized Pluronic L-31 resin. 2 wt % of DMPA was dissolved in a small amount of acetone and mixed with the L-31 resin. Three cure depth samples were generated at four exposure durations with a UV intensity of 4.9 mW/cm^2 at the resin surface. The exposure time varied from 2s to 5s in intervals of 1s. The thickness of the samples were measured and plotted against exposure energy. A trend line was calculated based on the plotted data to generate the working curve for Pluronic-L31.

7.1.2. Results and Discussion

Critical exposure and depth of penetration (E_c and D_p, respectively) were determined from the slope and x-intercept of the calculated trend line in the cure depth versus exposure energy curve. Figure 7-4 shows the graph of cure depth versus exposure energy for the four exposure durations along with the calculated trend line and error bars showing the standard deviation at each exposure. Table 7-2 provides the calculated E_c and D_p for the Pluronic L-31 with 2 wt% DMPA.

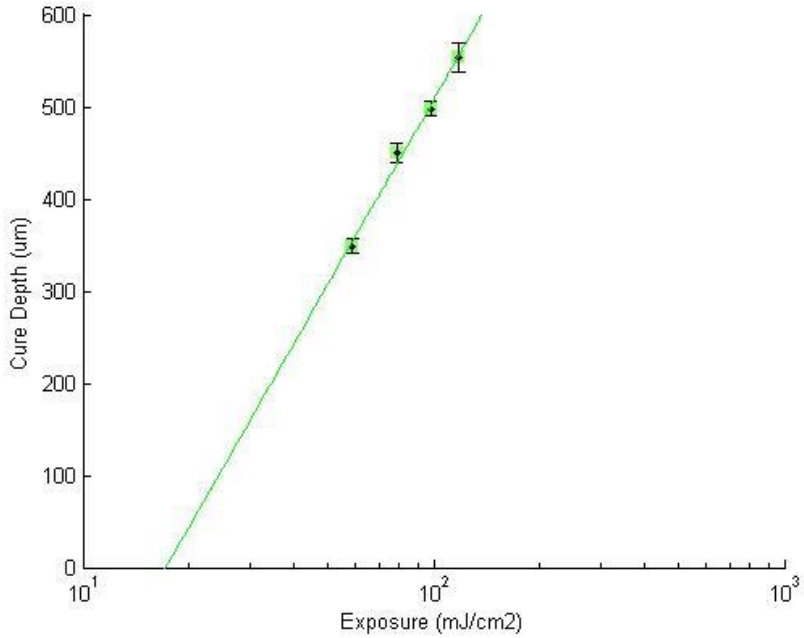

Figure 7-4: Working curve for the Pluronic L-31 with standard deviation error bars.

Table 7-2: Ec and Dp for Pluronic L-31 with 2 wt% DMPA.

	Pluronic L-31
Critical Exposure E_c (mJ/cm^2)	17.2
Depth of Penetration D_p (µm)	288.8

Figure 7-5 shows a benchmark part printed with 25 micrometer layers with the Pluronic L-31 resin. The exposure duration was 3.75 s with an intensity of 4.9 mW/cm^2 at the resin surface. Table 7-3 summarizes the characterization information gathered from the benchmark test part.

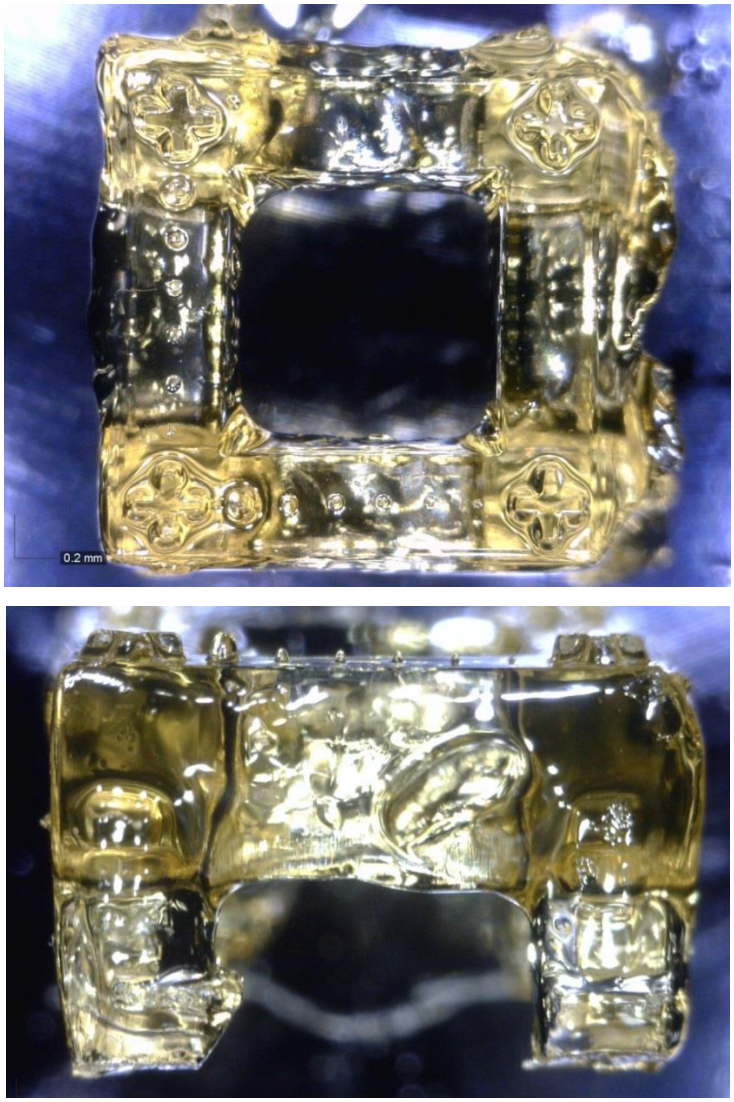

Figure 7-5: Top-down view (top) and lateral view (bottom) of the benchmark part printed with Pluronic L-31.

Table 7-3: Performance of the Pluronic L-31.

	Value	Std. Dev.	% Error
XY Min. Feature Size	57.3 µm	5.7 µm	22%
XY Accuracy	N/A	6.5 µm	6%
Z Accuracy	N/A	5.1 µm	83%

The minimum feature size in the XY plane is considerably better for the Pluronic L-31 photopolymer than the PPGDA photopolymer used to benchmark the system. However, the smallest measured features showed considerably more error than the 6% demonstrated by the PPGDA experiment. The accuracy in the XY plane is worse than the PPGDA, with twice the standard deviation (2.5% and 3.5 µm, respectively). The Z accuracy was so poor that the lateral extrusions had indistinguishable definition (Figure 7-5, bottom image), and the cross beam of the benchmark test part was the only measurable Z-dimension. However, the standard deviation of these cross-beam measurements was very low at 5.1 micrometers.

The Pluronic L-31 exhibited many of areas of curing where no light was shone, while the PPGDA did not have this issue. The unintended curing can be seen in the right side of the top image in Figure 7-5. These areas did not fall in the top XY plane or in the Z measurements for accuracy, and therefore are not reflected in these measurements and were not quantified. The areas of unintended curing, independent of the common print-through error reflected by the Z accuracy measurements, are stochastic in shape but localized to the right most side of the benchmark part when oriented according to the diagram in Figure 4-2. The localization of this print error may be the result of inaccurate DMD alignment or non-homogenous intensity distribution. Another possible reason for the poor accuracy of the Pluronic L-31 may be due to the block co-polymer architecture of the material. The interfaces between the PEG-PPG-PEG groups in the Pluronic L-31 may be effecting the penetration of the light into the resin, causing unforeseen scattering to occur. The scattering of light may the causing unintended curing and thus contribute to inaccuracy in parts.

Furthermore, Figure 7-6 qualitatively demonstrates the low Z accuracy of the Pluronic L-31 without any Tinuvin 400 stabilizer. The Pluronic L-31 shares the familiar arching overhangs and

non-distinct layers seen in the pure PPGDA (T0.00%) scaffold presented in Figure 6-14. This is likely a result of the high depth of penetration exhibited by the Pluronic L-31 (288.88 micrometers).

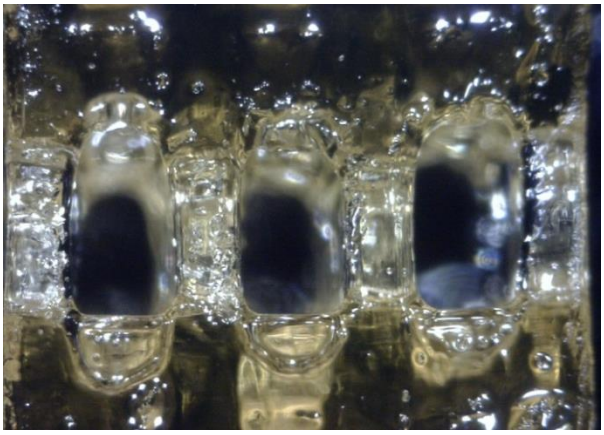

Figure 7-6: Basic scaffold part with 100 micrometer layers printed in Pluronic L-31.

In an attempt to remedy this, a small amount of Tinuvin 400 was mixed in with the Pluronic L-31 initiated with 2 wt% DMPA photo-initiator. The working curve for the Pluronic L-31 and the Pluronic L-31 with Tinuvin 400 are shown in Figure 7-7, and the critical characteristics for both samples are presented in Table 7-4.

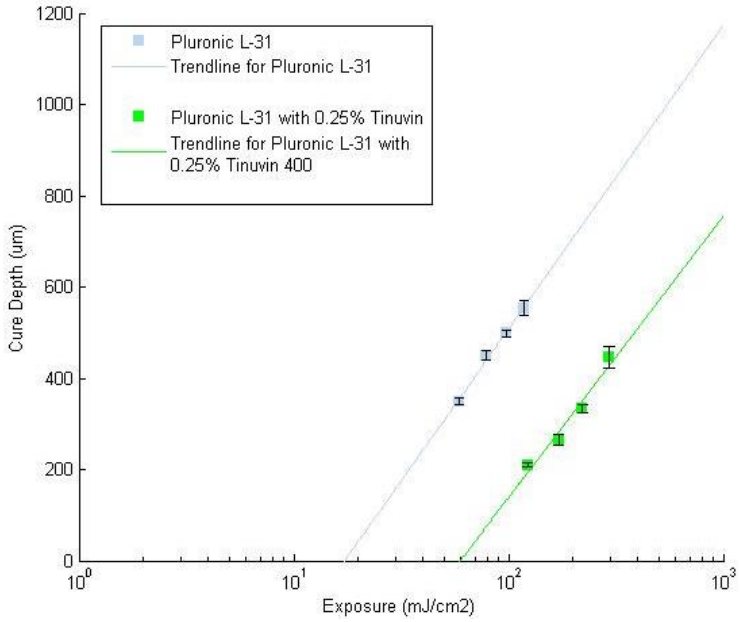

Figure 7-7: Working curve for Pluronic L-31 and Pluronic L-31 with 0.25wt% Tinuvin 400.

Table 7-4: Critical exposure (E_c) and depth of penetration (D_p) for Pluronic L-31 and Pluronic L-31 with 0.25% Tinuvin 400.

	Pluronic L-31	Pluronic L-31 with Tinuvin 400
Critical Exposure E_c (mJ/cm^2)	17.2	59.5
Depth of Penetration D_p (μm)	288.8	267.3

Unfortunately, the introduction of Tinuvin 400 into the Pluronic L-31 did not have the same effect as demonstrated in Section 6.2 with the PPGDA samples. While the depth of penetration was reduced slightly (21.5 micrometers), the critical exposure increased by approximately 248%. For reference, the PPGDA saw a depth of penetration reduction of 278 micrometers with only a 90% increase in critical exposure. Regardless, this experiment suggests that adding Tinuvin 400 at a greater concentration will further increase critical exposure with very small change in D_p, resulting in a photopolymer that will require long durations to cure a single layer. This could also lead to, as seen in the effects of extended exposure on the benchmark part from Section 6.1, a reduction in XY accuracy. Therefore, alternative means for reducing depth of penetration and improving Z accuracy should be explored.

7.2.Phosphonium Ionic Liquid (RQ4)

The phosphonium ionic liquid (PIL), a molten salt, is known to be ionically conductive. Ionic conductivity is useful in micro-actuation/sensing or microelectromechanical (MEMS) applications[28]. However, initial experimentation revealed that this ionic liquid did not cross-link alone. In order to enable photo-curing, the IL was mixed at various concentrations into PEGDMA (poly (ethylene glycol) dimethacrylate). As the property of interest for ionic liquids is their ionic conductivity, impedance analysis was conducted on thin films with 10%, 25%, and 30% ionic liquid in a PEGDMA network determine if and how the films demonstrated ionic conductivity.

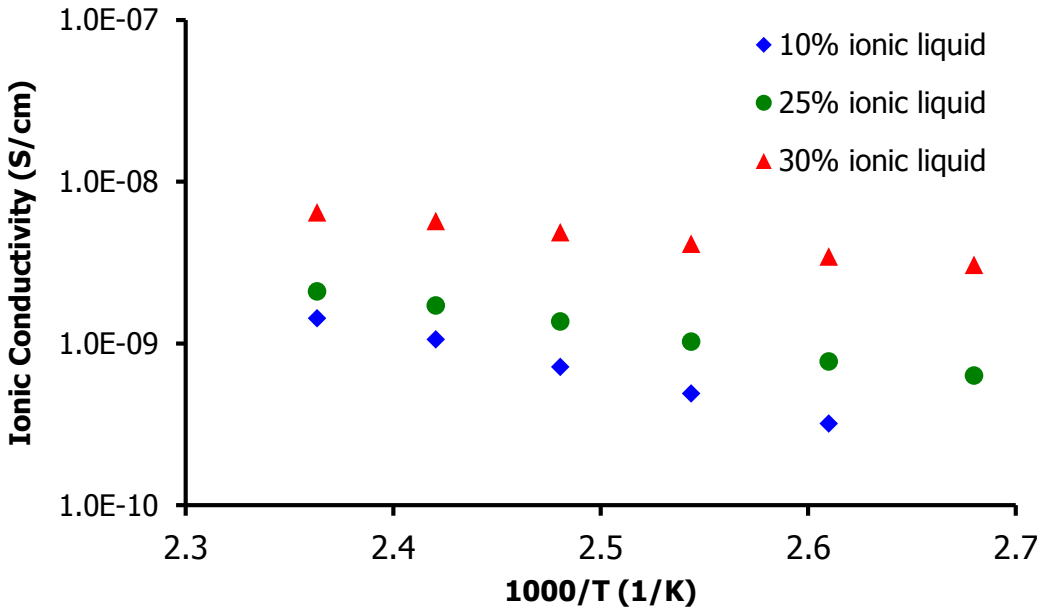

Figure 7-8: Ionic conductivity measurements of PEGDMA films containing 10%, 25%, and 30% concentrations of ionic liquid (courtesy of A Schultz of the Long Group, 2014).

The films demonstrated increasing degrees of ionic conductivity as the concentration of IL increased. With the ionic conductivity of PEGDMA/IL films validated, the curing properties of these mixtures need to be determined to understand how the ionic liquids will work with the

MPμSL system and if 3D structures can be fabricated. To accomplish this, research Question 4 (RQ4) was answered.

RQ4: *What are the curing characteristics of phosphonium ionic liquid and how does it perform in the MPμSL system?*

The characteristics of the ionic liquid were determined by again utilizing the process outlined in Chapter 4. Similar to the PPGDA and the Pluronic L-31, the phosphonium ionic liquid was characterized, and its performance in the system was determined.

7.2.1. Materials and Methods

Phosponium ionic liquid, TOPTf2N, is a molten salt at room temperature with the structure shown in Figure 7-9. Resin properties of the Phosphonium Ionic Liquid (PIL) are shown in Table 7-5.

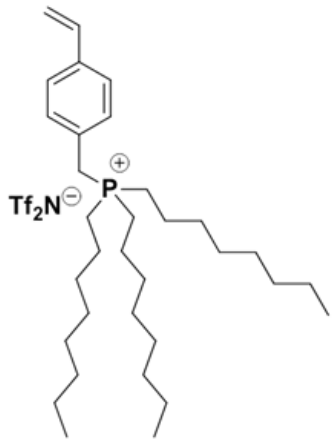

Figure 7-9: Chemical structure of the Phosphonium Ionic Liquid TOPTf2N.

Table 7-5: Properties of phosphonium ionic liquid.

Property	Value
Mol wt	~ 767.95 g/mol
Density	1.018 g/mL
Color	Light amber
Interest	Ionic conductivity

The ionic liquid alone was not reactive with the DMPA initiator, and no cross-linking was observed when pure PIL mixed with 5 wt% DMPA was exposed to UV light. To resolve this, the ionic liquid was mixed in various concentrations with BDA and PEGDMA (properties in Table 7-6 Table 7-7, chemical structure in Figure 7-10 and Figure 7-11, respectively).

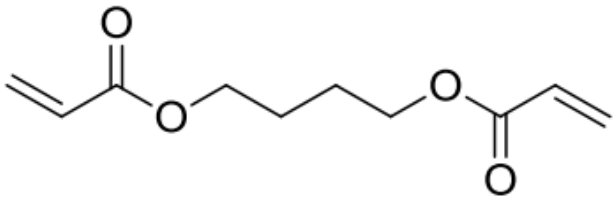

Figure 7-10: Chemical structure of BDA

Table 7-6: Properties of BDA.

Property	Value
Mol wt	~ 198.22 g/mol
Density	1.051 g/mL
Color	Colorless
Interest	Small Mn Network

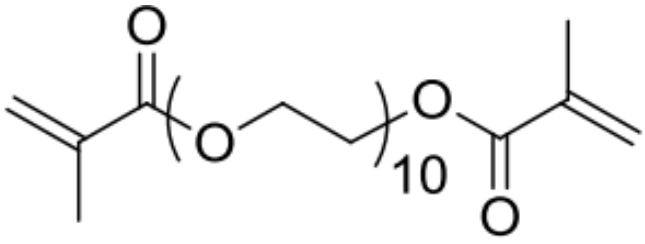

Figure 7-11: Chemical structure of PEGDMA.

Table 7-7: Properties of PEGDMA.

Property	Value
Mol wt	~ 550 g/mol
Density	1.099 g/mL
Color	Colorless
Interest	Larger Mn Network
Contains	270-330 ppm BHT 80-120 ppm MEHQ

As ionic conductivity of 3D printed parts is the characteristic of interest of the ionic liquid (IL), processability and ionic conductivity of the IL at different concentrations in PEGDMA and BDA were analyzed. The samples with varying concentrations of the IL were mixed, shown in Table 7-8 and Table 7-9.

Table 7-8: Preparation of the BDA prepolymer with varying ionic liquid concentrations.

Sample Name	Ionic Liquid Concentration (mol %)	Prepolymer
BDA (0%IL)	0	BDA, 2 wt% DMPA
B-IL10%	10	

Table 7-9: Preparation of the PEGDMA prepolymer with varying ionic liquid concentrations.

Sample Name	Ionic Liquid Concentration (mol %)	Prepolymer
PEGDMA (0%IL)	0	PEGDMA, 2 wt% DMPA
P-IL10%	10	(270-330 ppm BHT,80-
P-IL25%	25	120 MEHQ as inhibitor)

As was mentioned, the process outlined as part of CQ1 was used to characterize the ionic liquid. 2 wt % of DMPA was dissolved in a small amount of acetone and mixed with the prepared PEGDMA/PIL and BDA/PIL samples. Three cure depth specimens were generated at four exposure durations with an UV intensity of 4.9 mW/cm^2 at the resin surface for all samples. The thickness of the samples were measured and plotted against exposure energy. A trend line was calculated based on the plotted data to generate the working curve for Pluronic-L31.

7.2.2. Results and Discussion

Critical exposure and depth of penetration (E_c and D_p, respectively) were determined from the slope and x-intercept of the calculated trend line in the cure depth versus exposure energy curve. Figure 7-12 and Figure 7-13 show the graphs of cure depth versus exposure energy for

the four exposure durations for the BDA mixtures and PEGDMA mixtures, respectively. Table 7-10 provides the calculated E_c and D_p for all PIL mixtures.

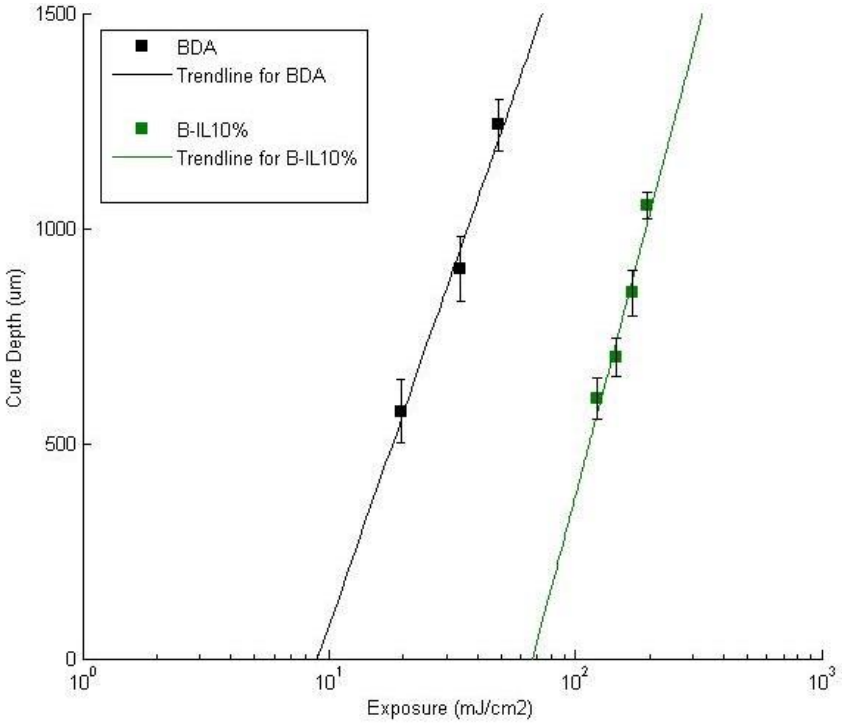

Figure 7-12: Working curve for the BDA samples with standard deviation error bars.

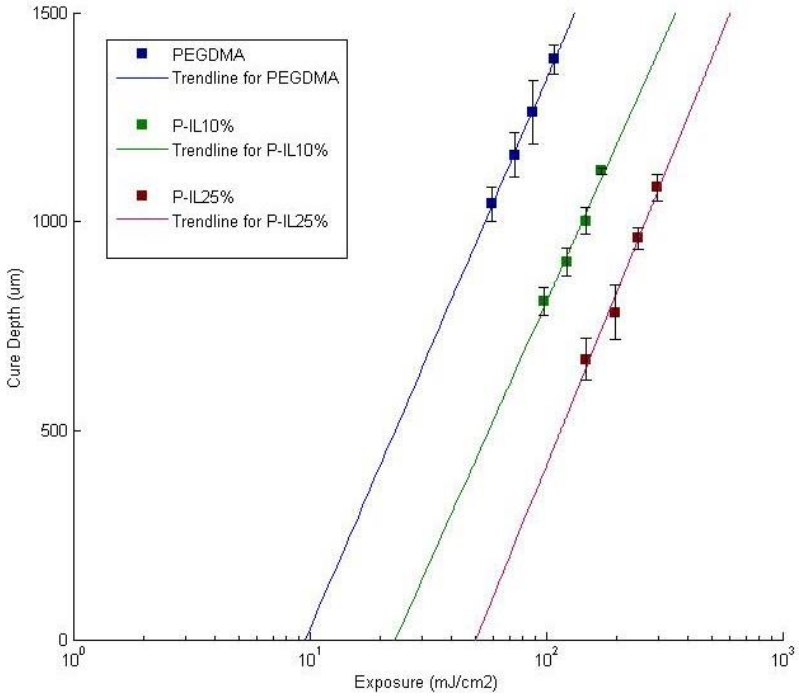

Figure 7-13: Working curve for the PEGDMA samples with standard deviation error bars.

Table 7-10: E_c and D_p for Ionic Liquid with 2 wt% DMPA.

Sample Name	Critical Exposure E_c (mJ/cm^2)	Depth of Penetration D_p (μm)
BDA (0%IL)	9.0	715
B-IL10%	67.1	944
PEGDMA (0%IL)	9.6	571
PIL10%	23.0	549
PIL25%	50.4	605

The table and figures above, regardless of base resin, reveal two significant trends.

1: Critical exposure of the resin increases with increasing concentrations of PIL.

2: There is no significant change in depth of penetration with varying concentrations of PIL.

With both the BDA and PEGDMA base resins, increasing concentrations of cause the exposure energy at which cross-linking begins to increase significantly (though much more dramatically with the BDA). However, ionic liquid seems to have little to no effect on the penetration depth of light into the resin. The depth of penetration for all mixtures is very high, which suggests that the Z axis accuracy will be very poor.

During the film fabrication process for the BDA and B-IL10% working curves, a notable phenomenon occurred. Once crosslinking of the BDA had begun (when the critical energy has been reached) the resins did not reflect the typical violet color of the LED light source, but rather emitted a magenta color. This is the first instance of this occurring in all UV curing processes during this body of research, and is likely attributed to the small molecular weight and high volatility of the BDA material.

Three benchmark parts were printed with each of the five sample IL mixtures. The benchmark parts were analyzed for XY minimum feature size, XY accuracy, and Z accuracy according to the methods demonstrated in Characterization Questions 1 and 3. A summary of the results are presented in Table 7-11.

Table 7-11: Summary of the performance of the ionic liquid samples.

	PEGDMA	P-IL10%	P-IL20%	BDA	B-PIL10%
XY Min. Feature Size	0.095mm	0.115mm	0.091mm	x	0.188mm
XY Accuracy (% error)	22%	22%	26%	5%	22%
Z Accuracy (% error)	150%	158%	176%	38%	117%

The minimum feature size of each of the resin mixtures are compared in the chart below, Figure 7-14, with standard deviation error bars.

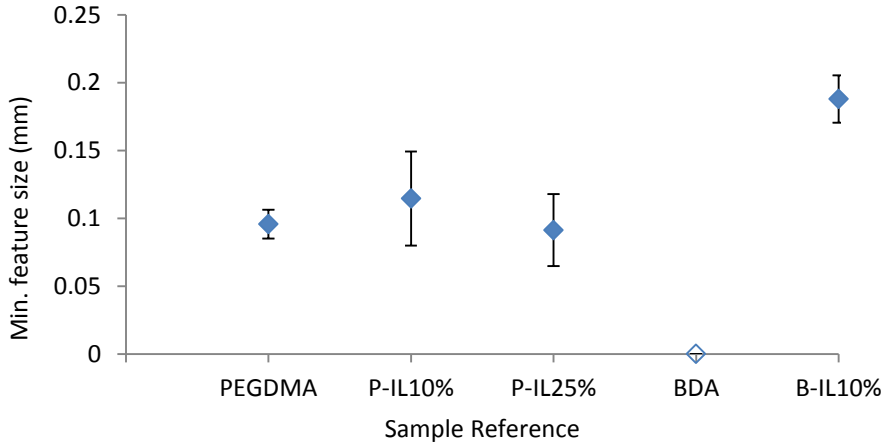

Figure 7-14: Minimum feature size of the five tested samples with standard deviation.

There are no significant differences between the achievable minimum features size in the PEGDMA based mixtures, which printed features around 95 micrometers. The BDA based resins demonstrated much lower resolution, with no feature size cylinders printed in the 100% BDA sample, and only the 200 micrometer cylinder printed.

The accuracy of the resin samples are compared in the chart presented in Figure 7-15. The blue diamonds represent the Z axis accuracy, and red squares represent the XY accuracy.

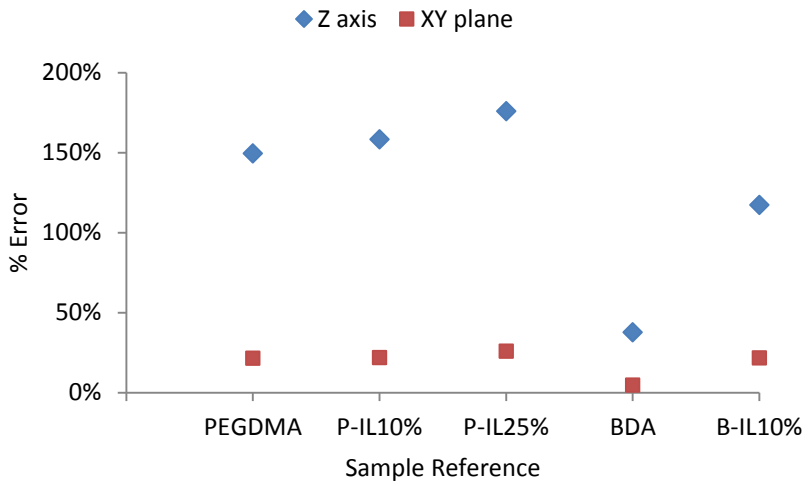

Figure 7-15: The XY plane and Z axis percent error for the five tested samples.

There appears to be a trend of increasing % error in both the XY plane and Z axis accuracy of printed parts as the concentration of ionic liquid increases in the prepolymer mixture. This trend extends to both the PEGDMA and BDA base resins, but more data points are necessary to confirm this trend.

To determine if this trend can be extended to the critical curing characteristics of photopolymers, the Z axis % error of each mixture was compared to the respective depth of penetration. This chart is presented in Figure 7-16.

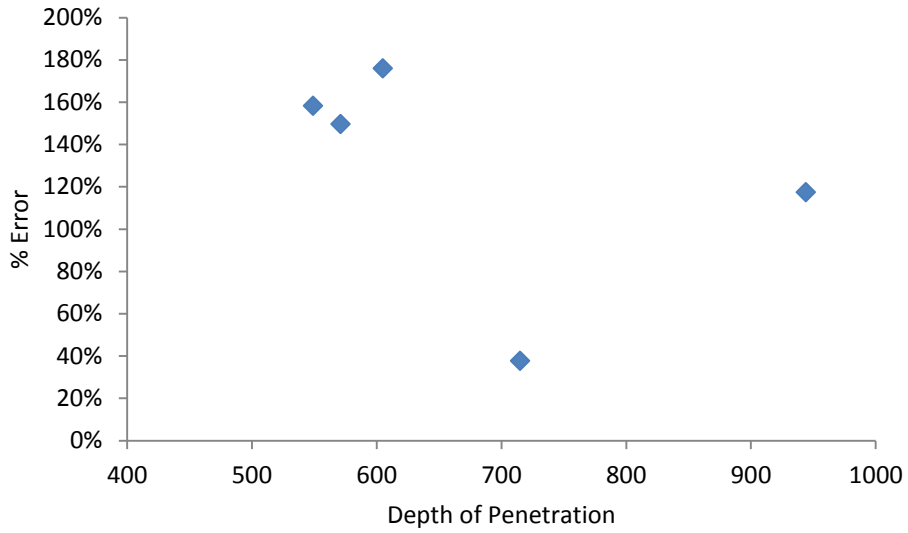

Figure 7-16: Comparison of depth of penetration to Z axis percent error.

Presumably, increasing depth of penetration would correlate with increasing Z axis accuracy in printed parts. This idea corresponds with the conclusion presented by Limaye, which suggests that the value for depth of penetration through cured layers tends to reach infinity, indicating that a cured layer is almost transparent to radiation [59]. However, according to the Figure 7-16, this may not be the case. The two highest depth of penetration values were found in the BDA samples, yet they show overall lower Z axis error than the PEGDMA samples. This suggests that depth of penetration in the cured BDA is significantly lower (demonstrating greater attenuation) than the uncured resin. This characteristic may be linked to the highly volatility of BDA, which is seen by rapid and violent degradation when exposed to high energy.

Furthermore, the Z accuracy error is significantly greater than the XY accuracy in all samples. However, it's important to note that while the 26% XY error in the P-IL25% sample seems small compared to its Z axis error of 176%, 26% error is indeed reflective of very poor XY accuracy. To demonstrate this, Figure 7-17 shows the benchmark part printed in pure BDA with an XY error of 6% next to the same part printed with the P-IL25% sample with the percent error of 26% for visual comparison. Figure 7-18 presents the same parts viewed laterally, to show the visual difference between the Z axis percent errors of pure BDA at 38% to the P-IL25% at 176%.

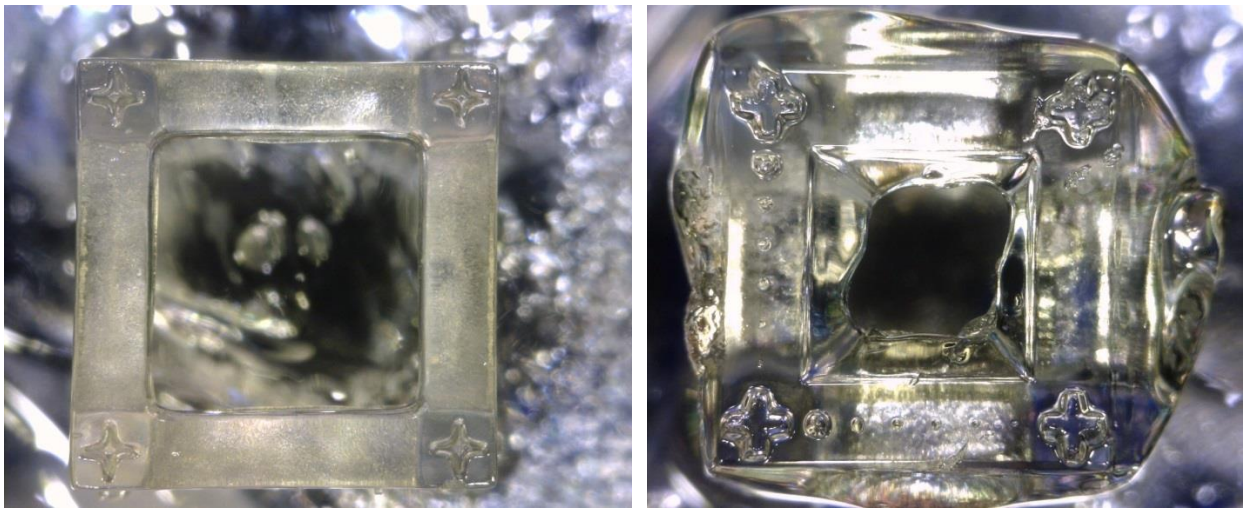

Figure 7-17: (Left) 100% BDA with a 5% XY error. (Right) P-IL25% with 26% XY error.

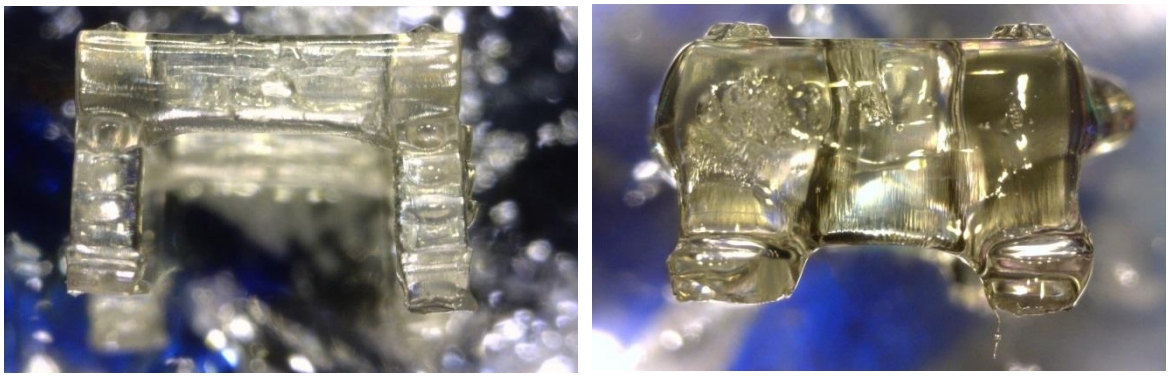

Figure 7-18: (Left) 100% BDA with 38% Z axis error. (Right) P-IL25% with 176% Z axis error.

As seen, all mixtures containing the ionic liquid had very poor accuracy in both the XY plane and Z axis. This is result, though perhaps not exclusively, of the high depth of penetration exhibited by these mixtures. Introducing Tinuvin 400 into these mixtures in small concentrations will reduce depth of penetration and presumably increase the Z accuracy. It is also hypothesized that TInuvin 400 will reduce light scattering and improve XY plane accuracy.

To demonstrate the utility of Tinuvin 400 in the IL samples, ~0.5 wt% Tinuvin 400 was mixed into the P-IL10% sample, and sample parts were fabricated. Figure 7-19 shows images of a Hokie bird model printed with P-IL10% without and with Tinuvin 400. Figure 7-20 shows a close up (left) and a macro image (right) of a hyperboloid structure printed with P-IL10% containing Tinuvin 400.

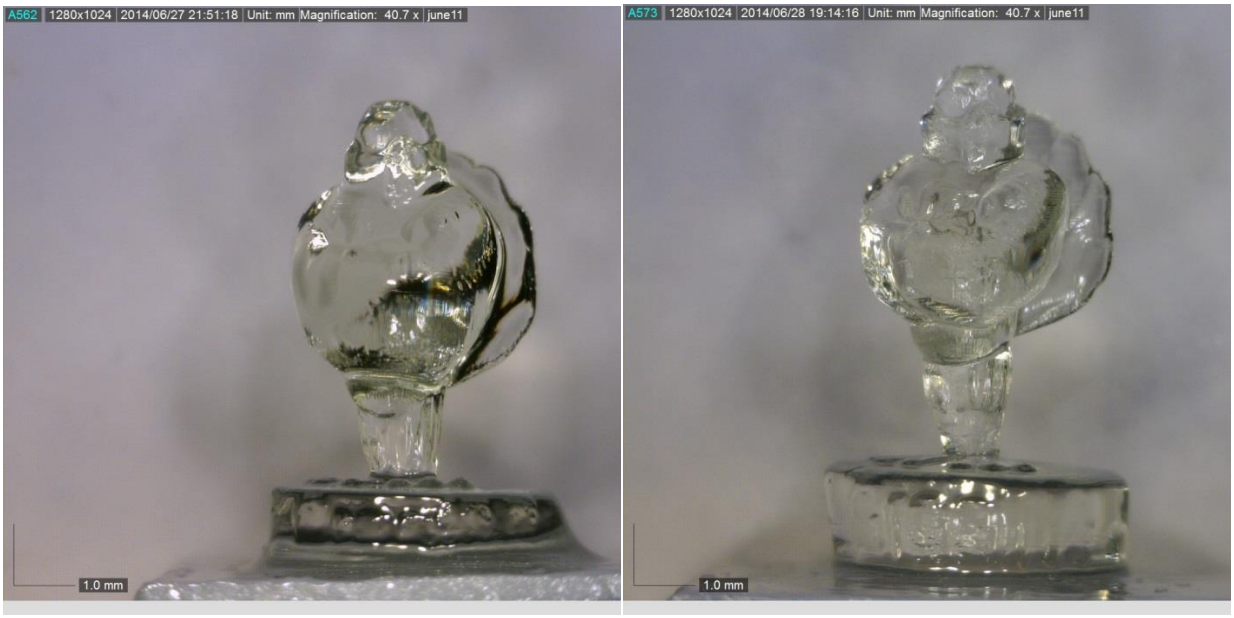

Figure 7-19: (Left) Hokie bird printed in P-IL10% with no Tinuvin 400. (Right) Hokie bird printed in P-IL10% with ~0.5wt% Tinuvin 400.

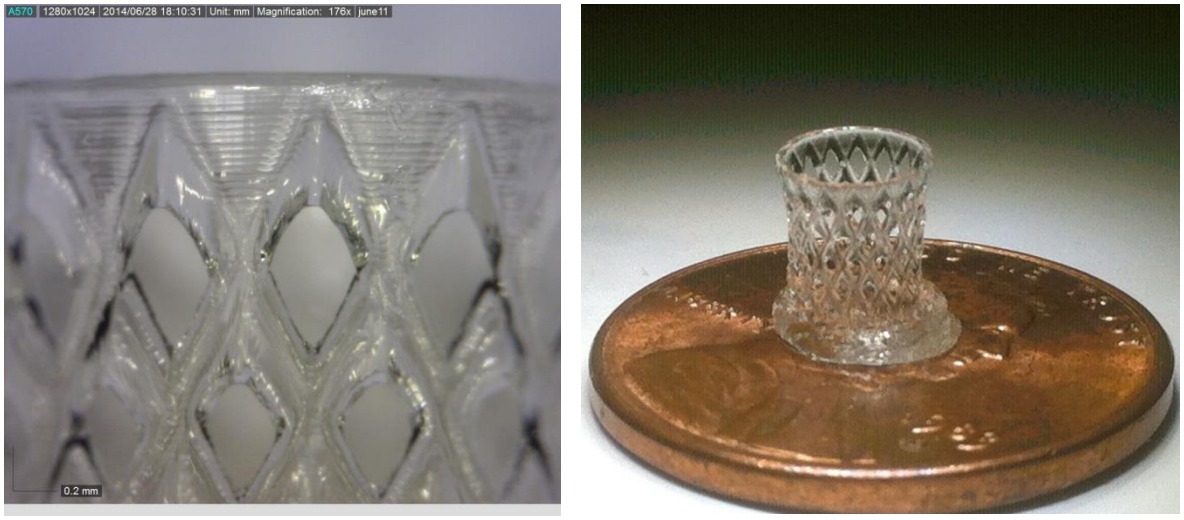

Figure 7-20: Hyperboloid shape printed in the P-IL10% with ~0.5wt% Tinuvin 400.

The Hokie bird figures in Figure 7-19 show that by introducing the Tinuvin 400, a more accurate structure can be fabricated. The image on the right displays a Hokie bird figure that has finer detail and is less affected by print-through. Accuracy improvement is further demonstrated by Figure 7-20, where complex micro-structures of the Hyperboloid were printed with very fine

detail. With demonstrated utility, samples containing Tinuvin 400 should be characterized using the methods outlined in Section 4. Impedance analysis should be repeated with the mixtures containing the Tinuvin 400 to confirm ionic conductivity is retained. Also, the mechanical properties of IL samples with and without Tinuvin should be determined to identify any changes.

8. Conclusions and Future Work

8.1. Summary of Research

The primary goal of this work was stated as follows:

"Design and build a projection microstereolithography 3D printing system to characterize, process, and quantify the performance of novel photopolymers."

This goal was met by designing and fabricating an MPμSL system (Chapter 3) that effectively demonstrated the ability to characterize and process photopolymers novel to projection stereolithography (Chapter 4). These photopolymers were then used to fabricate complex 3D structures, demonstrating their prospective utility in novel applications such as tissue engineering (Section 7.1) and MEMS fabrication (Section 7.2).

Many of the key requirements listed for the system were met. The system can manufacture 3D structures utilizing vat polymerization. The build process is relatively fast at 360 layers per hour (Table 5-6), and the build process is automated. System operation and user interface are simple, but some training is necessary to make quality parts.

With regard to customer needs, this system satisfactorily meets all target specifications with the exception of "the system should have very high resolution." The target specification of 5 micrometer features was not met; the smallest measured feature manufactured on the benchmark part was 38 micrometers (Section 5.1.3). However, both XY minimum feature size and Z accuracy are resin dependent characteristics of the system performance, and were addressed by Research Questions 1 and 2.

RQ1: *How does minimum feature size vary with exposure energy?*

The process/property relationship between exposure energy and feature size shows a trend in achievable XY minimum feature size as exposure energy increases (Section 6.1). The trend reveals that by increasing exposure energy by 420% (5.83 mJ/cm^2 to 24.5 mJ/cm^2) reduces the achievable feature size by 67% (0.212mm to 0.70mm).

RQ2: *How does Z-axis accuracy change with increasing concentrations of TInuvin 400?*

Experiments exploring the structure/property relationship of prepolymers demonstrated increasing Z-axis accuracy in printed parts with increasing concentrations of Tinuvin 400 (Section 6.2). This experiment shows that by including 0.25% Tinuvin 400 in the prepolymer, depth of penetration was reduced from 398.5 micrometers to 119.7 micrometers. This corresponds to a decrease in Z-axis error from 119% (no Tinuvin 400) to 9% Z-axis error (0.25% Tinuvin 400).

A process was developed to reliably and repeatedly determine the curing characteristics of novel photopolymer resins for processing via MPμSL (Section 4.3.1). A benchmark part was designed to characterize the performance of the polymer in the system (Section 4.3.2). The performance metrics for polymers printed with the system were identified as XY minimum feature size, XY accuracy, Z minimum feature size, and Z accuracy. Research Questions 3 and 4 addressed the performance of novel photopolymers in the designed system.

RQ3: *What are the curing characteristics of Pluronic L-31 how does it perform in the MPμSL system?*

A working curve was developed for Pluronic L-31 with 2 wt% DMPA; the critical exposure was 17.2 mJ/cm^2 and the depth of penetration was 288.8 micrometers (Section 7.1). The Pluronic L-31 achieved features as small as 57 micrometers on the benchmark part. The accuracy of the Pluronic L-31 resin was poor with 22% error in the XY plane and 83% error in the Z dimension.

RQ4: *What are the curing characteristics of phosphonium ionic liquid and how does it perform in the MPμSL system?*

Working curves were developed for 5 different prepolymer mixtures: pure PEGDMA, 10% IL in PEGDMA, 25% IL in PEGDMA, pure BDA, and 10% IL in BDA (Section 7.2). The results show increasing critical exposure with increasing concentrations of IL in both PEGDMA and BDA. There is no significant trend between increasing concentrations of IL in either PEGDMA or BDA and depth of penetration. Any trends previously identified between penetration depth and Z

accuracy do not seem to extend from one resin to another. This means that overall, among all resins, depth of penetration is not an accurate way to predict the Z axis accuracy of a part.

8.2.Research Contributions

The contributions of this work to the research community are:

- The development of a Mask Projection Microstereolithography system that verifies the utility of the morphological matrix design tool presented in “Design Considerations for Mask Projection Microstereolithography” (Section 3).
- A standardized process for characterizing and benchmarking the performance of a novel photopolymer in top-down projection based MPμSL systems (Section 4)
- The identification of the process/property relationship between exposure energy and achievable feature size (Section 6.1)
- Confirmation of the structure/property relationship between Tinuvin 400 photo-absorber and depth of penetration of photo-curable resins (Section 6.2)
- The characterization and performance of novel photo-curable block-copolymer Pluronic L-31 with 2 wt% DMPA photoinitiator in MPμSL systems (Section 7.1)
- The characterization and performance of novel photo-curable Phosponium Ionic Liquid in PEGDMA and BDA networks with 2 wt% DMPA photoinitiator in MPμSL systems (Section 7.2).
- The determination that depth of penetration may not correlate directly to Z-axis accuracy for all photopolymers (Section 7.2.2).

8.3. Future Work

The system designed as part of this work has several areas where ease of operation could be improved, as well as overall utility. Suggested improvements to the system include:

- Redesign the build platform.

The current stage and build platform are 3D printed with ABS plastic. This material is not optimal due to the ridges inherent in 3D printed parts, as well as the non-precise tolerances

contributing to a non-level build surface. The stage should be machined from aluminum, and the build platform should be replaced with a flat, inert surface.

- A mechanism or process for accurately maintaining the resin surface at the build plane.

A plague during the print process was the resin level falling below the focal point of projection plane. As mentioned earlier, any small vertical change in the resin surface caused the projected image to be out of focus, and the intensity to vary. The solution to this is to automate control over the resin surface, such as utilizing a precise micro-pump.

- A rotating stage with multiple vats, enabling the 3D manufacture of structures developed from multiple materials.

Several research groups have displayed interest in utilizing this system to construct 3D structures out of multiple types of photo-curable resin. The precedence for this exists in the research conducted by the Chen group through the introduction of multiple vats on a rotating stage [38], [60].

- A linear XY stage with one large vat, enabling the stitching of multiple exposures to manufacture larger layers.

With the current XY area of the system limited to 6mm x 8mm, the size of printed parts is severely limited in application. To manufacture larger parts and maintain XY resolution, image stitching can be utilized. By controlling the location of the build platform with an XY linear motor, multiple exposures can be used to create single layers [61].

- Projection light intensity distribution feedback.

The current system light source is an LED, which though experimentation, has shown significant light homogenization issues. The uneven intensity distribution across the projection plane may have devastating effects on part accuracy. A solution to this would be to install real-time intensity distribution monitoring via CCD camera. The data from the camera could feed back into the image manipulation software. Here, the projected image could be normalized with

intensity compensation by introducing greyscale calibration to each projected image [3], [51], [62].

8.3.1. Process Improvement

Besides system improvement, there are several other areas of future work that would benefit the scientific community. The experiments conducted in effort to improve the system performance unveiled questions that appear to unanswered in literature, and worthy of pursuing.

8.3.1.1. Exposure Energy versus Minimum Feature Size

This experiment made the assumption that oxygen inhibition is dominating the feature size threshold. To confirm this is indeed the case, the experiment should be repeated at controlled concentrations of oxygen on the resin surface. This data will aid in modeling the interaction between oxygen concentrations on minimum feature size. With this model, a more reliable process can be developed for open air projection stereolithography systems.

Conversely, alternative methods should be considered for reducing the effects of oxygen. Two options for this are (i) printing in an inert atmosphere (i.e. nitrogen), or (ii) printing with a constrained surface (resin surface flush with transparent substrate). These methods would remove the need to consider oxygen inhibition when conducting experiments.

8.3.1.2. Tinuvin 400 versus Penetration Depth

This experiment confirmed the ability of Tinuvin 400 to act as an effective photo-absorber for the PPGDA resin. However, the utility of this material needs to be extended to the resins of interest as part of this work, namely the Phosphonium ionic liquid mixtures. The determination of the structure/property relationship between Tinuvin 400 and penetration depth in the PIL resins will define the universal utility of Tinuvin 400 for increasing Z accuracy in this MPμSL system.

8.3.2. Novel Polymer Applications

While novel polymers have been characterized and processed using this MPμSL system, the next steps for both the Pluronic L-31 and Phosphonium Ionic Liquids are to demonstrate their utility in their respective fields of application.

8.3.2.1. Pluronic L-31

The Pluronic L-31 block-copolymer resin is the first of its kind to be manufactured into 3D structures via MPμSL. This polymer was chosen originally for characterization due to its biocompatibility. There are many variables introduced in the processing of this resin that may compromise the biocompatible nature of this polymer, such as the reactive photo-initiators and photo-absorbers. Cell assay tests should be conducted on thin films to determine the appropriate ratio of these chemicals to attempt to develop biocompatible 3D structures via MPμSL. Furthermore, the cross-linked Pluronic L-31 should be investigated to identify any properties, whether mechanical or otherwise, that are more advantageous in biological applications than existing photo-curable biocompatible resins. This investigation should identify how or why Pluronic L-31 should be used instead of existing biocompatible photopolymer standards such as poly (propylene fumarate) [63]–[65].

Furthermore, as the purpose of this system is to develop complex 3D structures, all thin film experiments suggested above should be repeated on 3D printed structure to insure that the desired biocompatible attributes are retained after 3D part fabrication.

Finally, with the design freedoms enabled by MPμSL, the next step is to confirm that micro and mesostructure formation can indeed be designed and optimized for cell type. One experiment that will be conducted compares the cell viability of HUVEC cells to osteoblasts on a 3D printed vein-like scaffold. The purpose behind this experiment is characterize the response of HUVECs (human umbilical vein endothelial cells) to a tubular, vein-like 3D printed scaffold, and compare it to the response of osteoblasts in the same structure. Ideally, better cell growth will be seen by the HUVECs in the vein-like scaffold due to the optimized environment.

This experiment will be conducted in partnership with the Dr. Abby Whittington Research Group from the department of Materials Science and Engineering.

8.3.2.2. Phosphonium Ionic Liquid

With multiple ratios of Ionic Liquid to PEGDMA/BDA identified that crosslinks to form a photo-curable prepolymer capable of being processed by MPμSL, examination into its utility in 3D

structures should be examined. A definitive application should be identified and proven as viable through experimentation.

Furthermore, all mixtures containing the ionic liquid had poor XY accuracy and extremely poor Z-axis accuracy. This is result of, though perhaps not exclusively, the high depth of penetration the samples demonstrate. Introducing Tinuvin 400 into these mixtures in small concentrations will reduce depth of penetration and presumably increase the Z accuracy. As mentioned earlier, Tinuvin 400 may also reduce light scattering, and improve XY accuracy as well. Impedance analysis should be repeated with the mixtures containing the Tinuvin 400 to confirm cured samples maintain ionic conductivity, and identify conductivity change (if any). Experimentation should also be conducted comparing the mechanical properties of the IL samples with and without Tinuvin 400.

This experiment will be conducted in partnership with the Dr. Tim Long Research Group from the Chemistry Department.

References

[1] A. Bertsch, S. Zissi, and J. Y. Je, “Microstereophotolithography using a liquid crystal display as dynamic mask-generator,” 1997.

[2] A. Bertsch and J. C. Andr, “Study of the spatial resolution of a new 3D microfabrication process : the microstereophotolithography using a dynamic mask-generator technique,” vol. 107, pp. 275–281, 1997.

[3] X. Zheng, J. Deotte, M. P. Alonso, G. R. Farquar, T. H. Weisgraber, S. Gemberling, H. Lee, N. Fang, and C. M. Spadaccini, “Design and optimization of a light-emitting diode projection micro-stereolithography three-dimensional manufacturing system.,” *Rev. Sci. Instrum.*, vol. 83, no. 12, p. 125001, Dec. 2012.

[4] Y. M. Ha, J. W. Choi, and S. H. Lee, “Mass production of 3-D microstructures using projection microstereolithography,” *J. Mech. Sci. Technol.*, vol. 22, no. 3, pp. 514–521, May 2008.

[5] C. Sun, N. Fang, D. M. Wu, and X. Zhang, “Projection micro-stereolithography using digital micro-mirror dynamic mask,” *Sensors Actuators A Phys.*, vol. 121, no. 1, pp. 113–120, May 2005.

[6] A. Limaye and D. D. W. Rosen, “Multi-Objective Process Planning Method For Mask Projection Stereolithography,” Georgia Institute of Technology, 2007.

[7] B. M. Comeau and D. C. L. Henderson, “Fabrication of Tissue Engineering Scaffolds Using Stereolithography,” Georgia Institute of Technology, 2007.

[8] a. Bertsch, H. Lorenz, and P. Renaud, “3D microfabrication by combining microstereolithography and thick resist UV lithography,” *Sensors Actuators A Phys.*, vol. 73, no. 1–2, pp. 14–23, Mar. 1999.

[9] L. Beluze, A. Bertsch, and P. Renaud, “Microstereolithography : a new process to build complex 3D objects Fixed light spot,” vol. 3680, no. April, pp. 808–817, 1999.

[10] M. Farsari, S. Huang, P. Birch, F. Claret-Tournier, R. Young, D. Budgett, C. Bradfield, and C. Chatwin, “Microfabrication by use of a spatial light modulator in the ultraviolet: experimental results.,” *Opt. Lett.*, vol. 24, no. 8, pp. 549–50, Apr. 1999.

[11] M. Farsari, F. Claret-Tournier, S. Huang, C. . Chatwin, D. . Budgett, P. . Birch, R. C. . Young, and J. . Richardson, “A novel high-accuracy microstereolithography method employing an adaptive electro-optic mask,” *J. Mater. Process. Technol.*, vol. 107, no. 1–3, pp. 167–172, Nov. 2000.

[12] C. R. Chatwin, M. Farsari, S. Huang, M. I. Heywood, R. C. D. Young, P. M. Birch, F. Claret-Tournier, and J. D. Richardson, “Characterisation of Epoxy Resins for Microstereolithographic Rapid Prototyping,” *Int. J. Adv. Manuf. Technol.*, vol. 15, no. 4, pp. 281–286, Apr. 1999.

[13] C. Chatwin, M. Farsari, S. Huang, M. Heywood, P. Birch, R. Young, and J. Richardson, “UV Microstereolithography System that uses Spatial Light Modulator Technology.,” *Appl. Opt.*, vol. 37, no. 32, pp. 7514–22, Nov. 1998.

[14] S. Monneret, V. Loubère, S. Corbel, D. De Chimie, and B. P. N. Cedex, “Microstereolithography using a dynamic mask generator and a non-coherent visible light source,” vol. 3680, no. April, pp. 553–561, 1999.

[15] A. Bertsch, “Microstereolithography: a Review,” in *Materials Research Society Symposium Proceedings*, 2002, vol. 758, p. 15.

[16] B. P. Chan and K. W. Leong, “Scaffolding in tissue engineering: general approaches and tissue-specific considerations.,” *Eur. Spine J.*, vol. 17 Suppl 4, pp. 467–79, Dec. 2008.

[17] F. P. W. Melchels, J. Feijen, and D. W. Grijpma, “A review on stereolithography and its applications in biomedical engineering.,” *Biomaterials*, vol. 31, no. 24, pp. 6121–30, Aug. 2010.

[18] S. Yang, K. Leong, Z. Du, and C. Chua, “The design of scaffolds for use in tissue engineering. Part I. Traditional factors,” *Tissue Eng.*, vol. 7, no. 6, pp. 679–689, 2001.

[19] S. Yang, K. Leong, Z. Du, and C. Chua, “The design of scaffolds for use in tissue engineering. Part II. Rapid prototyping techniques,” *Tissue Eng.*, vol. 8, no. 1, pp. 1–11, 2002.

[20] C. Heller, M. Schwentenwein, G. Russmueller, F. Varga, J. Stampfl, and R. Liska, “Vinyl Esters : Low Cytotoxicity Monomers for the Fabrication of Biocompatible 3D Scaffolds by Lithography Based Additive Manufacturing,” pp. 6941–6954, 2009.

[21] F. Intranuovo and R. Gristina, “Plasma Modification of PCL Porous Scaffolds Fabricated by Solvent-Casting/Particulate-Leaching for Tissue Engineering,” *Plasma Process. …*, pp. 1–4, 2014.

[22] L. D. Harris, B. S. Kim, and D. J. Mooney, “Open pore biodegradable matrices formed with gas foaming,” *J. Biomed. Mater. Res.*, vol. 42, no. 3, pp. 396–402, Dec. 1998.

[23] J. Lannutti, D. Reneker, T. Ma, D. Tomasko, and D. Farson, “Electrospinning for tissue engineering scaffolds,” *Mater. Sci. Eng. C*, vol. 27, no. 3, pp. 504–509, Apr. 2007.

[24] W. Sun, A. Darling, B. Starly, and J. Nam, “Computer-aided tissue engineering: overview, scope and challenges.,” *Biotechnol. Appl. Biochem.*, vol. 39, pp. 29–47, 2004.

[25] A. Jariwala, F. Ding, and D. W. Rosen, “Modeling effects of oxygen inhibition in mask-based stereolithography,” *Rapid Prototyp. …*, vol. 17, no. 3, pp. 168–175, 2011.

[26] J.-W. Choi, R. B. Wicker, S.-H. Cho, C.-S. Ha, and S.-H. Lee, “Cure depth control for complex 3D microstructure fabrication in dynamic mask projection microstereolithography,” *Rapid Prototyp. J.*, vol. 15, no. 1, pp. 59–70, 2009.

[27] A. S. Limaye and D. W. Rosen, “Compensation zone approach to avoid print-through errors in mask projection stereolithography builds,” *Rapid Prototyp. J.*, vol. 12, no. 5, pp. 283–291, 2006.

[28] S. Imaizumi, Y. Ohtsuki, T. Yasuda, H. Kokubo, and M. Watanabe, “Printable polymer actuators from ionic liquid, soluble polyimide, and ubiquitous carbon materials.,” *ACS Appl. Mater. Interfaces*, vol. 5, no. 13, pp. 6307–15, Jul. 2013.

[29] C. B. Williams, F. Mistree, and D. W. Rosen, “A Functional Classification Framework for the Conceptual Design of Additive Manufacturing Technologies,” *J. Mech. Des.*, vol. 133, no. 12, p. 121002, 2011.

[30] J.-W. Choi, R. Wicker, S.-H. Lee, K.-H. Choi, C.-S. Ha, and I. Chung, “Fabrication of 3D biocompatible/biodegradable micro-scaffolds using dynamic mask projection microstereolithography,” *J. Mater. Process. Technol.*, vol. 209, no. 15–16, pp. 5494–5503, Aug. 2009.

[31] A. Bertsch, P. Bernhard, C. Vogt, and P. Renaud, “Rapid prototyping of small size objects,” *Rapid Prototyp. J.*, vol. 6, no. 4, pp. 259–266, 2000.

[32] Y. Lu, G. Mapili, G. Suhali, S. Chen, and K. Roy, “A digital micro-mirror device-based system for the microfabrication of complex, spatially patterned tissue engineering scaffolds.,” *J. Biomed. Mater. Res. A*, vol. 77, no. 2, pp. 396–405, May 2006.

[33] G. W. Hadipoespito, Y. Yang, H. Choi, G. Ning, and X. Li, “Digital Micromirror Device Based on Microstereolithography for Micro Structures of Transparent Photopolymer and Nanocomposites,” University of Wisconsin-Madison, Madison, Wisconsin, 2003.

[34] L.-H. Han, G. Mapili, S. Chen, and K. Roy, “Projection Microfabrication of Three-Dimensional Scaffolds for Tissue Engineering,” *J. Manuf. Sci. Eng.*, vol. Vol. 130, p. 021005: 1–4, 2008.

[35] K. Takahashi and J. Setoyama, “A UV-exposure system using DMD,” *Electron. Commun. Japan (Part II Electron.*, vol. 83, no. 7, pp. 56–58, Jul. 2000.

[36] A. Bertsch, P. Bernhard, and P. Renaud, “Microstereolithography : Concepts and applications,” 2001.

[37] H.-W. Kang, J. H. Park, and D.-W. Cho, “A pixel based solidification model for projection based stereolithography technology,” *Sensors Actuators A Phys.*, vol. 178, pp. 223–229, May 2012.

[38] J.-W. Choi, E. MacDonald, and R. Wicker, “Multi-material microstereolithography,” *Int. J. Adv. Manuf. Technol.*, vol. 49, no. 5–8, pp. 543–551, Dec. 2009.

[39] Y. Pan, C. Zhou, and Y. Chen, “A Fast Mask Projection Stereolithography Process for Fabricating Digital Models in Minutes,” *J. Manuf. Sci. Eng.*, vol. 134, no. 5, p. 051011, 2012.

[40] T. V. Wilson, “How LCoS Works.” [Online]. Available: http://electronics.howstuffworks.com/lcos.htm.

[41] “3D Systems,” 2013. [Online]. Available: http://www.3dsystems.com/.

[42] Texas Instruments, “DLP ® 0.95 1080p 2 x LVDS Type A DMD,” no. September. p. 29, 2012.

[43] Keynote Photonics, “FlexLight ™ X1 DLP ® Development System Open Platform DLP ® Technology.” pp. 1–2, 2012.

[44] Hamamatsu, “UV-LED Spot Light Source LightningCure LC-L1V3.” Iwata City, japan, p. 4, 2012.

[45] Edmund Optics, “Beam Expanders.” [Online]. Available: http://www.edmundoptics.com/learning-and-support/technical/learning-center/application-notes/lasers/beam-expanders/. [Accessed: 17-Jan-2013].

[46] National Instruments, “Using a State Machine (Event Driven) Architecture,” 2008.

[47] P. J. Bartolo, Ed., *Stereolithography, Materials, Processes and Applications*. New York, NY: Springer, 2011.

[48] M. Talib, “Fabrication and characterisation of 3 dimensional scaffold for tissue engineering application via microstereolithography technique,” 2012.

[49] P. Jacobs, “Fundamentals of stereolithography,” *Proc. Solid Free. Fabr.,* July, 1992.

[50] R. Ibrahim, M. H. H. Ramlee, M. A. Shaik Mohamed, M. Ibrahim, and M. S. Wahab, “Evaluation on the Photoabsorber Composition Effect in Projection Microstereolithography,” *Appl. Mech. Mater.*, vol. 159, pp. 109–114, Mar. 2012.

[51] Amit S Jariwala, R. E. Schwerzel, and D. W. Rosen, “Real-time Interferometric Monitoring System for Exposure Controlled Projection Lithography,” in *Proceedings of the 22nd Solid Freeform Fabcrication Symposium*, 2011, pp. 99–110.

[52] A. Jariwala, H. Jones, A. Kwatra, and D. Rosen, “Process Planning Method for Exposure Controlled Projection Lithography,” *Proc. 24th Solid Free. Fabcrication Symp.*, pp. 95–110, 2013.

[53] Y. Pan, Y. Chen, and C. Zhou, “Fast Recoating Methods for the Projection-based Stereolithography Process in Micro- and Macro-Scales,” pp. 846–862.

[54] J. R. Zyzalo and D. J. Potgeiter, “Masked Projection Stereolithography: Improvement in the Limary Model for Curing Single Layer Medium Sized Parts,” Massey University, Albany, New Zealand, 2008.

[55] C. Zhou, Y. Chen, Z. Yang, and B. Khoshnevis, “Digital Material Fabrication Using Mask-Image-Projection- based Stereolithography,” pp. 1–16, 2011.

[56] M. M. Zabti, “Effects of Light Absorber on Micro Stereolithography Parts,” The University of Birmingham, 2012.

[57] B. S. Inc., “Coatings that stay looking good,” Ludwigshafen, Germany.

[58] B. C. Inc., “Safety Data Sheet Tinuvin 400,” Mississauga, ON, 2013.

[59] A. Limaye and D. Rosen, “Process planning to build Mask Projection Stereolithography parts with accurate vertical dimensions,” *Proc. 17th Solid Free. …*, pp. 159–173, 2007.

[60] H. Kim, J. Choi, E. Macdonald, and R. Wicker, “Slice overlap-detection algorithm for process planning in multiple-material stereolithography,” *Int. Jounrnal Adv. Manuf. Technol.*, pp. 1161–1170, 2010.

[61] A. Limaye and D. Rosen, “Process planning method for curing accurate microparts using Mask Projection Micro Stereolithography,” *… 2nd Int. Conf. …*, pp. 1–6, 2005.

[62] J. Potgieter and J. Zyzalo, “Layer Curing for Masked Projection Stereolithography: the effects of varying irradiance distributions,” *… Mach. Vis. …*, no. Dmd, pp. 604–609, 2008.

[63] P. X. Lan, J. W. Lee, Y.-J. Seol, and D.-W. Cho, “Development of 3D PPF/DEF scaffolds using micro-stereolithography and surface modification.,” *J. Mater. Sci. Mater. Med.*, vol. 20, no. 1, pp. 271–9, Jan. 2009.

[64] J. W. Lee, G. Ahn, J. Y. Kim, and D.-W. Cho, “Evaluating cell proliferation based on internal pore size and 3D scaffold architecture fabricated using solid freeform fabrication technology.,” *J. Mater. Sci. Mater. Med.*, vol. 21, no. 12, pp. 3195–205, Dec. 2010.

[65] J. W. Lee, P. X. Lan, B. Kim, G. Lim, and D.-W. Cho, “3D scaffold fabrication with PPF/DEF using micro-stereolithography,” *Microelectron. Eng.*, vol. 84, no. 5–8, pp. 1702–1705, May 2007.

Appendices

Appendix A- Engineering Drawings of DMD mount

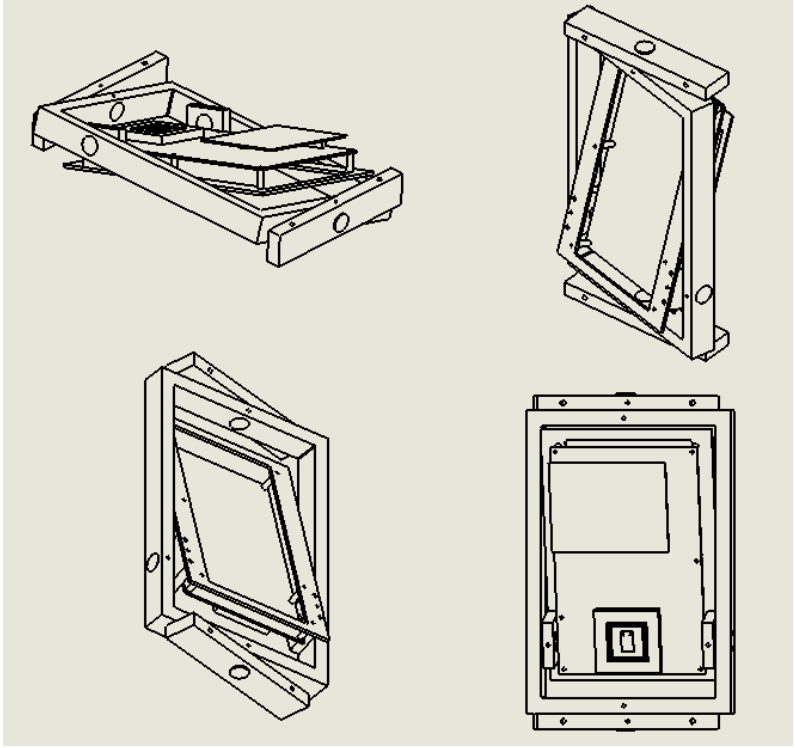

Appendix B- Bill of Materials

Vendor	Description	Part Number	#	Cost per unit
Keynote Photonics	Flexlight X1 Evaluation Kit	X1-1080P	1	$7,705.00
Hamamatsu	LightningCure LC-L1V3 Collimating Head	L11922-401	1	$1,354.00
Hamamatsu	LightningCure LC-L1V3 Driver	C11924-501	1	$967.00
ThorLabs	Performance Series I Breadboard	PBH11106	1	$923.80
ThorLabs	Breadboard Mounting Feet (Imperial)	BMF4	1	$26.00
ThorLabs	Dovetail Optical Rail	RLA1800	1	$106.00
ThorLabs	Extended Rail Carrier	RC2	1	$26.00
ThorLabs	Rail Carrier	RC1	6	$23.00
ThorLabs	Post Holder	PH2	6	$7.70
ThorLabs	Table Clamp	CL6	4	$5.60
Zaber	Linear Actuator	NA11B60	1	$472.00
AllMotion	EZ10ENSK EZ Stepper Starter Kit	EZ10ENSK	1	$175.00
Jameco	Power Supply	1952214	1	$20.49
Jameco	Power Cord	38050	1	$4.95
Edmund Optics	UV Plano-Convex Lens (50mm diam, 150 FL)	67-220	2	$249.00
Edmund Optics	UV Plano-Convex Lens (50mm diam, 75 FL)	67-218	1	$225.00
Edmund Optics	UV Plano-Concave Lens (12mm diam, -25 FL)	48-050	1	$100.00
Edmund Optics	Optical Mount (50mm)	64-568	3	$49.00
Edmund Optics	Optical Mount (12mm)	64-555	1	$38.00
Edmund Optics	Mounting Post (4" length)	59-000	9	$9.70
Edmund Optics	First Surface Mirror	43-876	1	$22.50
Edmund Optics	Mirror Mount	58-858	1	$119.00
Edmund Optics	Bandpass Filter	65-130	1	$195.00
Edmund Optics	Optic Mount (for Filter)	64-560	1	$40.00
Edmund Optics	Holographic UV Diffuser	48-513	1	$550.00
Edmund Optics	Optical Cell Assembly (Diffuser Mount)	36-465	1	$83.00
Edmund Optics	Right Angle Post Clamp	53-357	3	$16.00
Edmund Optics	Mounting Post (12" length)	59-010	1	$16.00
Edmund Optics	Mounting Post (6" length)	59-008	1	$12.00
Edmund Optics	Post Holder Assembly	59-006	2	$25.00
Carolina Fluid Components	80/20 Aluminum, Brackets, Screws	N/A	1	$129.00
McMaster	Aluminum Block	89155K78	1	$173.85
McMaster	Aluminum Sheet	89015K18	1	$28.34
McMaster	Aluminum Rod	9062K331	1	$13.85
McMaster	Nylon Spacer	93657A833	10	$1.07
McMaster	Flat Head Phillips Machine Screw	91500A197	1	$8.83
Fisher	20 mL Beaker (quantity 12)	02-539-1	1	$74.45
			Total	$13,995.13

Appendix C- Benchmarking Minimum Feature Size Test Data

		Minimum feature radius					
		1.19	cylinder	3	cylinder	5	cylinder
Sample 1	X1	0.109	1	0.051	3	0.032	4
	Y1	0.105	1	0.038	3	0.035	4
Sample 2	X2	0.103	1	0.045	3	0.038	5
	Y2	0.109	1	0.042	3	0.042	5
Sample 3	X3	0.102	1	0.047	3	0.033	4
	Y3	0.108	1	0.08	2	0.031	4
Avg. radius		0.106		0.0505		0.0352	
Avg. diameter		0.212		0.101		0.0703	
Std. dev. (radius)		0.0028		0.0138		0.0038	
Std. dev. (diameter)		0.0057		0.0276		0.0076	

		200 micron cylinder radius					
		1190	cylinder	3000	cylinder	5000	cylinder
Sample 1	X	0.109	1	0.142	1	0.13	1
	Y	0.105	1	0.127	1	0.132	1
Sample 2	X	0.103	1	0.158	1	0.139	1
	Y	0.109	1	0.128	1	0.162	1
Sample 3	X	0.102	1	0.166	1	0.158	1
	Y	0.108	1	0.137	1	0.14	1
Avg. radius		0.106		0.143		0.1435	
Std. dev.		0.003		0.015		0.012	

Appendix D- XY Accuracy Test Data

PPGDA XY Accuracy

	Design	*Sample 1*	*% error*	*Sample 2*	*% error*	*Sample 3*	*% error*	*avg*	*dev from design*	*std dev of data*
X1	0.400	0.386	0.035	0.420	0.050	0.403	0.008	0.403	0.003	0.024
X2	0.600	0.655	0.092	0.677	0.128	0.621	0.035	0.651	0.051	0.016
X3	4.130	4.064	0.016	4.132	0.000	4.075	0.013	4.090	0.040	0.048
X4	4.400	4.333	0.015	4.423	0.005	4.305	0.022	4.354	0.046	0.064
X5	4.600	4.602	0.000	4.699	0.022	4.591	0.002	4.631	0.031	0.069
X6	4.880	4.809	0.015	4.910	0.006	4.798	0.017	4.839	0.041	0.071
X7	5.000	4.966	0.007	5.005	0.001	4.971	0.006	4.981	0.019	0.028
X8	3.000	2.861	0.046	2.894	0.035	2.889	0.037	2.881	0.119	0.023
Y1	0.400	0.403	0.008	0.409	0.022	0.414	0.035	0.409	0.009	0.004
Y2	0.600	0.705	0.175	0.666	0.110	0.644	0.073	0.672	0.072	0.028
Y3	4.130	4.131	0.000	4.143	0.003	4.092	0.009	4.122	0.008	0.008
Y4	4.400	4.355	0.010	4.417	0.004	4.372	0.006	4.381	0.019	0.044
Y5	4.600	4.630	0.007	4.702	0.022	4.635	0.008	4.656	0.056	0.051
Y6	4.880	4.876	0.001	4.915	0.007	4.870	0.002	4.887	0.007	0.028
Y7	5.000	5.027	0.005	5.039	0.008	4.999	0.000	5.022	0.022	0.008
Y8	3.000	2.911	0.030	2.967	0.011	2.917	0.028	2.932	0.068	0.040
		Average % Error	3%		3%		2%		Average Std Dev	0.035

Pluronic L-31 XY Accuracy

	Design	*Sample 1*	*% error*	*Sample 2*	*% error*	*Sample 3*	*% error*	*avg*	*% error*	*dev from design*	*std dev of data*
X1	0.4	0.408	0.02	0.502	0.2550	0.49	0.2250	0.467	17%	0.067	0.066
X2	0.6	0.75	0.2500	0.75	0.2500	0.739	0.2317	0.746	24%	0.146	0.000
X3	4.13	3.947	0.0443	4.196	0.0160	4.071	0.0143	4.071	1%	0.059	0.176
X4	4.4	4.423	0.0052	4.467	0.0152	4.332	0.0155	4.407	0%	0.007	0.031
X5	4.6	4.55	0.0109	4.645	0.0098	4.55	0.0109	4.582	0%	0.018	0.067
X6	4.88	4.822	0.0119	4.887	0.0014	4.775	0.0215	4.828	1%	0.052	0.046
X7	5	4.988	0.0024	5.047	0.0094	4.887	0.0226	4.974	1%	0.026	0.042
X8	3	2.772	0.0760	2.89	0.0367	2.831	0.0563	2.831	6%	0.169	0.083
Y1	0.4	0.366	0.0850	0.165	0.5875	0.42	0.0500	0.317	21%	0.083	0.142
Y2	0.6	0.668	0.1133	0.573	0.0450	0.597	0.0050	0.613	2%	0.013	0.067
Y3	4.13	3.947	0.0443	4.024	0.0257	3.924	0.0499	3.965	4%	0.165	0.054
Y4	4.4	4.196	0.0464	4.385	0.0034	4.285	0.0261	4.289	3%	0.111	0.134
Y5	4.6	4.55	0.0109	4.633	0.0072	4.492	0.0235	4.558	1%	0.042	0.059
Y6	4.88	4.822	0.0119	4.857	0.0047	4.692	0.0385	4.790	2%	0.090	0.025
Y7	5	4.928	0.0144	4.946	0.0108	4.84	0.0320	4.905	2%	0.095	0.013
Y8	3	2.807	0.0643	2.86	0.0467	2.86	0.0467	2.842	5%	0.158	0.037
			5%		8%		5%			Average Std Dev	0.065

Appendix E- Z Accuracy Test Data

PPGDA Z Accuracy (Cross beams only)

	Design	Sample 1	Sample 2	Sample 3	avg	% error	stddev
X side	1	2.71	2.578	1.979	2.422	142%	0.390
Y side	1	2.07	1.793	2.003	1.955	96%	0.145
					2.189	119%	0.267

Pluronic L-31 Z Accuracy (Cross beams only)

	Design	Sample 1	Sample 2	Sample 3	avg	% error	stddev
X side	1	1.868	1.877	1.877	1.874	87%	0.005
Y side	1	1.81	1.877	1.686	1.791	79%	0.097
					1.8325	83%	0.051

PPGDA Z accuracy (Lateral Extrusions) with Tinuvin 400

	XT0.15%	YT0.15%	Design	% error	stddev	XT0.25%	YT0.25%	Design	% error	stddev
1	1.148	1.14	1.25	8%	0.061		1.123	1.25	10%	0.090
2	1.573	1.628	1.45	10%	0.091		1.461	1.45	1%	0.008
3	1.616	1.628	1.75	7%	0.074		1.624	1.75	7%	0.089
4	2.053	2.1	1.9	9%	0.105		1.894	1.9	0%	0.004
5	2.104	2.1	2.25	7%	0.085		2.091	2.25	7%	0.112
6	2.541	2.576	2.35	9%	0.122		2.344	2.35	0%	0.004
7	1.119	1.616	1.25	9%	0.258	1.14	1.11	1.25	10%	0.074
8	1.483	1.504	1.33	12%	0.095	1.35	1.333	1.33	1%	0.011
9	1.624	1.603	1.75	8%	0.080	1.568	1.581	1.75	10%	0.102
10	1.899	1.95	1.8	7%	0.076	1.791	1.714	1.8	3%	0.047
11	2.079	2.07	2.25	8%	0.101	2.087	2.078	2.25	7%	0.097
12	2.318	2.344	2.38	2%	0.031	2.245	2.198	2.38	7%	0.094
13	1.328	1.281	1	30%	0.177	1.119	1.058	1	9%	0.060
			Average	10%	0.104			Average	6%	0.061

Appendix F- XY Accuracy Data for IL experiment samples

Ionic Liquid Accuracy

		BDA					*PEGDMA*					*10% IL in BDA*					*25%IL in PEGDMA*					*10%IL in PEGDMA*				
	Design	*Sample 1*	*Sample 2*	*Sample 3*	*std dev*	*% error*	*Sample 1*	*Sample 2*	*Sample 3*	*std dev*	*% error*	*Sample 1*	*Sample 2*	*Sample 3*	*std dev*	*% error*	*Sample 1*	*Sample 2*	*Sample 3*	std dev	*% error*	*Sample 1*	*Sample 2*	*Sample 3*	*std dev*	*% error*
X1	0.400	0.349	0.409	0.397	0.032	0.038	0.569	0.777	0.688	0.104	0.695	0.603	0.670	0.771	0.085	0.703	0.678	0.605	0.575	0.053	0.548	0.624	0.787	0.605	0.100	0.680
X2	0.600	0.514	0.563	0.534	0.025	0.105	0.843	0.984	0.996	0.085	0.568	0.843	0.866	0.967	0.066	0.487	1.021	0.765	0.824	0.134	0.450	1.042	0.999	0.884	0.082	0.625
X3	4.130	4.303	4.264	4.460	0.104	0.051	4.536	4.133	4.193	0.217	0.038	4.509	4.460	4.555	0.048	0.092	4.562	4.116	4.122	0.256	0.033	4.577	4.230	4.175	0.218	0.048
X4	4.400	4.543	4.525	4.626	0.054	0.037	4.865	4.484	4.430	0.237	0.044	4.749	4.703	4.721	0.023	0.074	4.858	4.359	4.394	0.279	0.031	4.845	4.453	4.264	0.296	0.027
X5	4.600	4.701	4.733	4.810	0.056	0.032	5.050	4.709	4.650	0.216	0.044	5.057	4.899	4.934	0.083	0.079	5.231	4.537	4.578	0.389	0.040	5.215	4.700	4.513	0.364	0.046
X6	4.880	4.955	4.964	5.005	0.027	0.019	5.414	4.905	4.911	0.292	0.040	5.276	5.165	5.519	0.181	0.090	5.512	4.821	4.869	0.386	0.038	5.482	4.958	4.792	0.360	0.040
X7	5.000	5.057	5.078	5.148	0.048	0.019	5.701	5.385	5.658	0.171	0.116	5.578	5.589	5.658	0.043	0.122	5.962	5.349	5.776	0.314	0.139	5.681	5.276	5.148	0.278	0.074
X8	3.000	3.173	3.131	3.214	0.042	0.058	3.091	1.548	1.287	0.975	0.342	2.912	2.212	2.414	0.360	0.162	2.275	1.668	1.61	0.368	0.383	2.172	2.034	1.732	0.225	0.340
Y1	0.400	0.384	0.344	0.409	0.033	0.053	0.404	0.812	0.765	0.223	0.651	0.630	0.664	0.640	0.017	0.612	0.850	0.884	0.7	0.098	1.028	0.768	0.458	0.623	0.155	0.541
Y2	0.600	0.500	0.576	0.587	0.047	0.076	0.699	1.032	0.937	0.172	0.482	0.884	0.896	0.795	0.055	0.431	1.158	1.038	0.884	0.137	0.711	1.110	0.670	0.890	0.220	0.483
Y3	4.130	4.338	4.324	4.335	0.007	0.049	4.392	4.389	4.246	0.083	0.051	4.591	4.578	4.507	0.045	0.104	4.804	4.430	4.187	0.311	0.083	4.776	3.948	4.140	0.433	0.038
Y4	4.400	4.598	4.614	4.596	0.010	0.046	4.680	4.638	4.555	0.064	0.051	4.879	4.881	4.723	0.091	0.097	5.188	4.644	4.4	0.403	0.078	5.098	4.206	4.460	0.460	0.043
Y5	4.600	4.749	4.792	4.756	0.023	0.036	5.002	4.863	4.768	0.118	0.060	5.153	5.011	4.904	0.125	0.092	5.482	4.827	4.756	0.400	0.092	5.413	4.418	4.750	0.507	0.057
Y6	4.880	4.954	5.047	5.035	0.051	0.027	5.304	5.122	5.070	0.123	0.058	5.421	5.261	5.242	0.098	0.088	5.749	5.088	4.958	0.424	0.079	5.660	4.688	5.041	0.492	0.051
Y7	5.000	4.961	5.137	5.136	0.101	0.016	5.461	5.261	5.243	0.121	0.064	5.633	5.527	5.510	0.067	0.111	6.064	5.397	5.272	0.426	0.116	5.935	5.346	5.355	0.337	0.109
Y8	3.000	3.317	3.149	3.428	0.140	0.099	3.097	2.283	2.182	0.502	0.160	2.892	2.449	2.503	0.242	0.128	2.323	2.150	1.716	0.313	0.312	2.296	2.147	1.821	0.243	0.304
	average				0.050	5%				0.231	22%				0.102	22%				0.293	26%				0.298	22%
				X avg	0.048	4%			X avg	0.287	24%			X avg	0.111	23%			X avg	0.272	21%			X avg	0.240	24%
				Y avg	0.052	5%			Y avg	0.176	20%			Y avg	0.093	21%			Y avg	0.314	31%			Y avg	0.356	20%

Appendix G- Z Accuracy Data for IL experiment samples

		BDA					*PEGDMA*					*10% IL in BDA*					*25%IL in PEGDMA*					*10%IL in PEGDMA*				
	Design	*Sample 1*	*Sample 2*	*Sample 3*	std dev	*% error*	*Sample 1*	*Sample 2*	*Sample 3*	std dev	*% error*	*Sample 1*	*Sample 2*	*Sample 3*	std dev	*% error*	*Sample 1*	*Sample 2*	*Sample 3*	std dev	*% error*	*Sample 1*	*Sample 2*	*Sample 3*	std dev	*% error*
ZX	1.000	1.221	1.257	1.398	0.094	29%	2.33	3.043	2.409	0.391	159%	2.09	2.197	2.163	0.055	1.15	2.946	2.749	2.714	0.125	180%	2.729	2.503	2.573	0.116	160%
ZY	1.000	1.371	1.375	1.645	0.157	46%	2.213	2.491	2.497	0.162	140%	2.037	2.174	2.385	0.175	1.19867	2.851	2.491	2.809	0.197	172%	2.784	2.467	2.444	0.190	157%
					0.125	38%				0.277	150%				0.115	117%				0.161	176%				0.153	158%

Appendix H- Raw Data for Working Curves

Raw data for the working curves of all photopolymer samples.
UV Intensity for all experiments: 4.9 mW/cm^2
All samples have 2 wt% DMPA photo-initiator

T0.00 (100% PPGDA)

```
exposuretime = [2 2.5 3 3.5] %seconds
sample2 = [185 284 345 425]; %micron
sample3 = [196 286 338 427]; %micron
sample4 = [203 284 340 413]; %micron
sample5 = [185 290 345 421]; %micron
```

T0.05%

```
exposuretime = [4 5 6 7]; %seconds
sample2 = [237 320 361 410]; %micron
sample3 = [246 320 359 397]; %micron
sample4 = [235 315 359 403]; %micron
sample5 = [240 305 361 392]; %micron
```

T0.15%

```
exposuretime = [4 5 6 7]; %seconds
sample2 = [151 185 220 241]; %micron
sample3 = [138 185 229 228]; %micron
sample4 = [142 185 223 241]; %micron
sample5 = [132 185 225 237]; %micron
```

T0.25%

```
exposuretime = [7 9 11 13]; %seconds
sample2 = [125 176 176 206]; %micron
sample3 = [135 162 182 199]; %micron
sample4 = [123 160 186 192]; %micron
sample5 = [118 177 174 215]; %micron
```

Pluronic L-31

```
exposuretime = [12 16 20 24]; %seconds
sample2 = [356 455 504 552]; %micron
sample3 = [342 457 501 574]; %micron
sample4 = [355 435 500 535]; %micron
sample5 = [343 452 487 552]; %micron
```

Pluronic L-31 with 0.25wt% Tinuvin

```
exposuretime = [25 35 45 60]; %seconds
sample2 = [203 275 342 423]; %micron
sample3 = [212 261 324 472]; %micron
sample4 = [210 251 338 457]; %micron
sample5 = [212 277 328 429]; %micron
```

BDA (0% IL)

```
exposuretime = [4 7 10]; %seconds
sample2 = [433 700 975]; %micron
sample3 = [475 607 918]; %micron
sample4 = [490 637 851]; %micron
sample5 = [326 776 977]; %micron
```

B-IL10% (10% IL in BDA)

```
exposuretime = [25 30 35 40]; %seconds
sample2 = [651 738 805 1072]; %micron
sample3 = [608 742 906 1010]; %micron
sample4 = [536 657 884 1079]; %micron
sample5 = [620 667 803 1057]; %micron
```

PEGDMA (0% IL)

```
exposuretime = [12 15 18 22]; %seconds
sample2 = [1012 1224 1343 1339]; %micron
sample3 = [1044 1092 1173 1389]; %micron
sample4 = [1097 1158 1304 1408]; %micron
sample5 = [1013 1164 1231 1417]; %micron
```

P-IL10% (10% IL in PEGDMA)

```
exposuretime = [20 25 30 35]; %seconds
sample2 = [807 924 984 1112]; %micron
sample3 = [769 931 993 1125]; %micron
sample4 = [810 859 1050 1128]; %micron
sample5 = [851 900 980 1118]; %micron
```

P-IL25% (25% IL in PEGDMA)

```
exposuretime = [30 40 50 60]; %seconds
sample2 = [692 758 932 1049]; %micron
sample3 = [676 833 993 1115]; %micron
sample4 = [715 839 951 1059]; %micron
sample5 = [598 701 966 1102]; %micron
```